

THESIS FOR THE DEGREE OF DOCTOR OF PHILOSOPHY IN SOLID AND
STRUCTURAL MECHANICS

Numerical simulation of thermomechanically coupled transient
rolling contact — An arbitrary Lagrangian–Eulerian approach

ANDREAS DRAGANIS

Department of Applied Mechanics
CHALMERS UNIVERSITY OF TECHNOLOGY

Göteborg, Sweden 2014

Numerical simulation of thermomechanically coupled transient rolling contact — An arbitrary Lagrangian–Eulerian approach
ANDREAS DRAGANIS
ISBN 978-91-7597-053-0

© ANDREAS DRAGANIS, 2014

Doktorsavhandlingar vid Chalmers tekniska högskola
Ny serie nr. 3734
ISSN 0346-718X
Department of Applied Mechanics
Chalmers University of Technology
SE-412 96 Göteborg
Sweden
Telephone: +46 (0)31-772 1000

Chalmers Reproservice
Göteborg, Sweden 2014

Numerical simulation of thermomechanically coupled transient rolling contact — An arbitrary Lagrangian–Eulerian approach

Thesis for the degree of Doctor of Philosophy in Solid and Structural Mechanics

ANDREAS DRAGANIS

Department of Applied Mechanics

Chalmers University of Technology

ABSTRACT

Numerical simulation of rolling contact serves as an important complement to laboratory and full-scale testing in the endeavour to further the understanding of related physical mechanisms, e.g. the influence of friction on the rolling motion, the thermomechanical interaction, damage phenomena and related modes of failure. In the development of computational methods for the analysis of rolling contact, a major challenge is to enhance predictive capabilities while keeping computational efforts reasonable.

The work presented in this thesis aims to provide a general and versatile theoretical and computational framework for efficient, high-resolution analysis of fully transient, thermomechanically coupled, frictional rolling contact between two deformable bodies. To this end, the pertinent thermomechanically coupled boundary value problem is stated in terms of an Arbitrary Lagrangian–Eulerian (ALE) kinematical description, whereupon a computational framework is developed in the context of the Finite Element (FE) method. Here, the Streamline-Upwind Petrov–Galerkin (SUPG) method is implemented and a quasi Residual-Free Bubble (RFB) method developed in order to address numerical instability issues related to the convective ALE description of the energy balance equation. Other components of the computational model include a support for non-reflecting boundary conditions, irregular surface profiles, and a computationally efficient methodology for mixed control between rolling velocities and corresponding driving forces.

In contrast to traditional and still predominant approaches to rolling contact, including semi-analytical methods based on Hertz and Carter theory, the described computational model provides a high geometrical versatility, and accommodates a thermomechanically coupled, fully transient analysis, including inertial effects. The ALE description is noted to allow for, among other things, a highly localized mesh refinement, linearization of the thermomechanical response, a compact computational domain and velocity-independent contact interface modelling.

Numerical simulations are presented, covering a range of transient, thermomechanical rolling contact phenomena. These show the model to be able to capture e.g. fully transient stick/slip behaviour, negotiation of strongly non-smooth surface profiles, and a range of thermomechanical phenomena, including frictional heat generation and the effect of convective cooling of the rolling body due to the contact with the foundation. Numerical results are as far as possible validated toward analytical solutions.

Keywords: arbitrary Lagrangian–Eulerian, rolling contact, thermomechanical coupling, transient analysis, frictional contact, finite element method

PREFACE

The work presented in this thesis was carried out at the division of Material and Computational Mechanics at Chalmers University of Technology during 2009–2014. It was carried out as part of the activities within the National Centre of Excellence in Railway Mechanics (CHARMEC), under the project name *MU25: Thermodynamically coupled contact between wheel and rail*. The financial support provided by the Swedish Research Council (Vetenskapsrådet) under the contract 2008-3860 is gratefully acknowledged.

I would like to thank my excellent supervisors: professors Anders Ekberg and Fredrik Larsson, for their friendship as well as their invaluable counselling during the course of my PhD project. Anders is a railway mechanics guru with an admirable engineering intuition, on top of being impossibly well-read in the engineering literature. As for Fredrik – and everyone who has ever worked with him will agree – it seems like the only limitation on the rate at which he is able to produce his mathematical wizardry is the speed of his writing hand.

The division of Material and Computational Mechanics and its neighbour Dynamics are connected through a long corridor. It is therefore natural for people from both divisions to meet regularly in the shared break room for lunches and coffee breaks. The result is an extraordinarily pleasant social environment. A thank you goes out to all of my colleagues in both divisions for coming in to work every day and contributing to it.

I would like to thank my friends and family, for their unfailing love and support throughout all these years (although one sibling in particular will take advantage of this opportunity to laugh at me for this uncharacteristic outpouring of clichéd sentimentality).

I finally thank my girlfriend Bella. I don't now if I would have been able to get to this point without her, and her constant supply of love, patience, encouragement, and carrots.

THESIS

This thesis consists of an extended summary and the following appended papers:

- Paper A** A. Draganis, F. Larsson, and A. Ekberg. Numerical evaluation of the transient response due to non-smooth rolling contact using an arbitrary Lagrangian–Eulerian formulation. *Proceedings of the Institution of Mechanical Engineers, Part J: Journal of Engineering Tribology* **226.1** (2012), 36–45. DOI: 10.1177/1350650111422015
- Paper B** A. Draganis, F. Larsson, and A. Ekberg. Finite element analysis of transient thermomechanical rolling contact using an efficient arbitrary Lagrangian–Eulerian description. *Computational Mechanics* **54.2** (2014), 389–405. ISSN: 0178-7675. DOI: 10.1007/s00466-014-0992-6
- Paper C** A. Draganis, F. Larsson, and A. Ekberg. Finite element modelling of frictional thermomechanical rolling/sliding contact using an arbitrary Lagrangian–Eulerian formulation. *Proceedings of the Institution of Mechanical Engineers, Part J: Journal of Engineering Tribology (in review)* (2014)
- Paper D** A. Draganis. “Finite element modelling of transient thermomechanical rolling contact featuring mixed control of the rigid body motion”. To be submitted for international publication

Papers A–C were prepared in collaboration with the co-authors. The author of this thesis is responsible for the majority of the work performed, including planning and writing the papers, developing the theory and the numerical implementation, and designing and carrying out the numerical simulations.

CONTENTS

Abstract	i
Preface	iii
Thesis	v
Contents	vii
I Extended Summary	1
1 Introduction	1
1.1 Motivation	1
1.2 Aim, approach and scope	3
2 Rolling contact mechanics	4
2.1 The analytical theory	4
2.2 Semi-analytical approaches	6
2.3 BE approaches	6
2.4 FE approaches	7
2.4.1 Overview	7
2.4.2 ALE approaches	8
3 Continuum thermomechanics	9
3.1 Governing equations	9
3.2 Thermomechanical coupling	11
4 The ALE kinematical description	12
4.1 Brief history	12
4.2 Overview	12
4.3 One-dimensional example	14
4.4 Application to rolling contact	16
5 Numerical stabilization of convection–diffusion problems	18
5.1 Introduction	18
5.2 Numerical stabilization methods	19
5.2.1 The SUPG method	19
5.2.2 Bubble function approaches	20
5.3 One-dimensional example	21
6 Summary of appended papers	22
7 Conclusions and outlook	23
7.1 Contributions of the thesis	23

7.2 Suggestions for future work 25

References **25**

II Appended Papers A–D **35**

Part I

Extended Summary

1 Introduction

1.1 Motivation

Numerical simulation of rolling contact serves as an important complement to laboratory and full-scale testing in the endeavour to further the understanding of related physical mechanisms, e.g. the influence of friction on the rolling motion, the thermomechanical interaction, damage phenomena and related modes of failure. In the development of computational methods for the analysis of rolling contact, a major challenge is to enhance predictive capabilities while keeping computational efforts reasonable.

Computational approaches to the analysis of rolling contact predominantly employ semi-analytical contact models based on Hertz/Carter theory [5, 6, 7]. These approaches have the advantage of being computationally efficient and simple to implement. An alternative to these models is provided by Kalker's and Vollebregt's CONTACT code [8, 9], which is a sophisticated framework for the analysis of rolling contact based on a boundary element (BE) formulation. However, although there are ongoing efforts to develop these approaches and extend them to new areas of applicability, they are ultimately limited by the fundamental assumptions upon which they are based. These include the half-space assumption (which requires the contact region to be small relative to the radii of curvature of the contacting bodies), assumptions of nominally flat contact surfaces, quasistatic dynamics, a purely mechanical analysis, and typically elastic materials. In contrast, a computational rolling contact model of the type considered in this thesis, i.e. one based on the Finite Element (FE) method and an Arbitrary Lagrangian–Eulerian (ALE) kinematical description [10], has the advantage of inheriting the great versatility of the former, and is thus not restricted by any of the aforementioned limitations.

A significant motivation for the work presented in this thesis, and one of its main long-term goals, is to further the understanding and facilitate the identification of detrimental operational conditions and modes of failure in railway mechanics applications [11, 12]. Of particular interest are damage phenomena for which traditional rolling contact models have proven insufficient. As a particular example, consider the damage shown in Figure 1.1. The pattern with inclined cracks to the right (toward the field side of the wheel) is due to frictional contact on the low rail during curving. Note the very sharp border to the nearby damage band with more radially oriented cracks, mainly owing to braking on (more or less) tangent track. This would correspond to a rather sharp transition in contact characteristics (in the presented case believed to be related to the profile of the inner rail in curves). In order to numerically simulate the conditions generating this damage pattern, it is necessary to account for dynamic wheel–rail forces during curving, braking forces, and the sharp transition in contact geometries. This requires a numerical model detailed enough to capture non-Hertzian contact conditions. Ideally, the model should



Figure 1.1: *Surface initiated rolling contact fatigue cracks on a loco wheel tread.*

also be able to incorporate elastic-plastic material characteristics.

The need for detailed and general modelling of contact geometries becomes even more important in the presence of contact geometry discontinuities, e.g. insulated joints, crossings, indentations, or wheel flats. Under such conditions, half-space based approaches are generally not applicable.

In addition to the mechanical loading, thermal loads may have a significant influence on the material response. Consider Figure 1.2, where the wheel tread has been subjected to a high thermal load in addition to the rolling contact loading. The result is discoloured spots containing (thermal) cracks. The discolouration is likely to have been caused by material phase transitions resulting from high temperatures. The cracking is mainly owing to the thermal loading, although the influence of the mechanical loading may be significant [13]. To capture these damage phenomena in numerical simulations, there is a need for evaluation of the wheel-rail contact stress field under dynamic loading. In addition, the thermal interaction between the wheel and the rail (and possibly between wheel and brake blocks) must be included. An important objective in this context is to capture the effect of rail chill [14], whereby the comparatively cold rail exerts a cooling influence on the wheel.

In the numerical analysis of rolling contact phenomena, it is often sufficient to focus on one separate part of the problem at a time. For example, in an analysis where only the impact load of wheel flats is of interest, a simplified model that focuses solely on the related dynamics can be adopted [15, 16]. Similarly, when wheel fractures due to overheating are studied, a commonly employed simplification is to ignore any effects of the superposed rolling contact loading [14]. However, due to ever-increasing performance demands on wheels and rails, the number of cases where such simplifications are unviable is increasing. This is especially clear in cases where there is an obvious interaction between thermal and mechanical loads, e.g. in the damage pattern in Figure 1.2.

A common simplification in traditional computational approaches to rolling contact is to limit the analysis to a quasistatic description (and therefore neglect inertial effects).



Figure 1.2: *Wagon wheel tread subjected to thermal and rolling contact loading, resulting in clustered thermomechanical damage.*

An example of an area where this is not acceptable is the study of rail corrugation [17, 18]. The mechanisms behind the onset of corrugation are still largely unknown, and reliable predictive models are elusive. What is known, however, is that it is essential to the success of such a model to incorporate the dynamical interaction between wheel and rail, in connection with a detailed analysis of material damage mechanisms.

The above discussion points toward an emergent need, in the analysis of rolling contact phenomena in railway mechanics, to go beyond the limitations of traditional approaches. In particular, this might mean taking dynamic/inertial effects and thermomechanical coupling phenomena into account, and/or accommodating non-smooth geometries.

1.2 Aim, approach and scope

The work presented in this thesis aims to provide a general and versatile methodology for efficient, high-resolution analysis of fully transient, thermomechanically coupled, frictional rolling contact between two deformable bodies. To this end, an analytical model is developed on the basis of an ALE description [10], which leads to a convective formulation of the governing thermomechanical boundary value problem. On this basis, a computational framework based on the FE method is constructed, where numerical instability issues related to the discretized energy balance equation are addressed using the Streamline-Upwind Petrov–Galerkin (SUPG) method [19, 20], and a variation of a particular quasi Residual-Free Bubble (RFB) method [21].

The numerical implementation was written from scratch in MATLAB, with an aim toward a modular and extensible computational framework. All code was written by the author, with the exception of a general-purpose meshing library written by Fredrik Larsson.

Throughout the work presented in this thesis, the analysis has been limited to two-dimensional geometries, isotropic, linear thermoelasticity, and relatively rudimentary

mechanical and thermal constitutive contact interface models. Since the long-term goal of the work is toward railway mechanics applications, material modelling considerations are focused toward metallic (rather than e.g. polymeric) materials. Furthermore, optimization of computational efficiency and robustness has not been held as the highest priority. While numerical results have in some cases been qualitatively compared against data from operational conditions, quantitative experimental verification has not been performed. These limitations in scope have been for the benefit of a focus toward – equally – developing the theoretical foundations of the ALE approach to rolling contact, and tackling fundamental computational issues that arise as it is extended to e.g. fully transient, thermomechanically coupled applications.

2 Rolling contact mechanics

2.1 The analytical theory

The continuum theory of contact mechanics was developed by Heinrich Hertz at age 23 during his 1880 Christmas vacation [22], and first published in his historic paper from 1882 [5]. Appreciated both for its mathematical elegance and its practical applicability, the theory attracted considerable attention from the scientific community. In the field of mechanical engineering, it found early application in railway mechanics, as well as in the modelling of rolling bearings and gears. Hertzian contact theory is computationally efficient and – due to subsequent extensions by other researchers over the years – currently applicable to a broad range of engineering contact problems. It is therefore ubiquitous in the field of contact mechanics to this day.

Hertzian contact theory considers purely mechanical, frictionless, non-adhesive contact between two linear elastic bodies [7, 23, 5]. It further assumes that the contacting bodies are smooth and non-conforming, so that the size of the contact patch may be considered small in relation to representative dimensions of the bodies (e.g. radii of curvature). The contact stresses can then be considered to be much larger than those appearing elsewhere in the system, and highly concentrated to the contact region. For this reason, they may be seen as dependent only on conditions local to the contact region. Another fundamental assumption of Hertz theory is the half-space assumption: For the purpose of establishing relationships between contact pressures and internal stresses and displacements, each contacting body is approximated as an elastic half-space. This assumption is valid whenever the contact surface may be considered small in relation to radii of curvature of the (undeformed) contacting bodies. Furthermore, it makes available the great wealth of analytical methods developed for the elastic half-space, for the evaluation of stress and deformation fields in the interiors of the contacting bodies. Two important works contemporary to Hertz: Cerruti [24] and Boussinesq [25], as well as the famous treatises on elasticity theory: Love [26] and Timoshenko and Goodier [23], are notable in this context.

Hertz showed – using analogies between elasticity and electrostatic potential theory – that the contact pressure distribution acting between two three-dimensional bodies, whose surfaces are locally approximable by quadratic functions, takes the form of a semi-ellipsoid

acting on an elliptic contact region. It should here be noted that the Hertzian contact pressure distribution is obtained using a geometric non-penetration boundary condition that considers the undeformed shape of the contacting bodies. However, this is the only way in which the shapes of the contacting bodies are taken into account: throughout the rest of Hertzian contact theory, they are approximated as elastic half-spaces.

Once the contact pressure distribution is known, analytical theories for the elastic half-space may be used in order to obtain e.g. distributions of stresses and displacements in the interiors of the contacting bodies [7, 27, 28].

Since its conception, Hertz theory has been extended outside of the confinements of its original assumptions of smooth, non-conforming, frictionless, linear elastic contact situations. The reader is referred to Johnson [7] or Johnson [22] for an extensive discussion of the development of Hertzian contact theory in the one hundred years following its conception. To name a few select examples, Steuermann [29], Goodman and Keer [30] and Paul and Hashemi [31] present analytical theories of elastic, conformal contact, Johnson, Kendall, and Roberts [32] presents a surface-energy based formulation of adhesive contact between elastic solids, Johnson [33] studies the situation of a rigid indenter being pressed down upon an elastic-plastic half-space and Greenwood and Tripp [34] models the case of an elastic sphere in contact with a rough, elastic plane.

The extension of the continuum contact theory to rolling/sliding contact applications is of obvious engineering interest. Early work in this area includes Cattaneo [35], where the static situation of two spheres pressed together and shifted in the tangential direction is considered, and the resulting tangential contact traction distribution is derived (see also Mindlin [36]). In this case, the contact region is divided into a central stick zone and two neighbouring slip zones (see Figure 2.1a).

The analytical continuum theory of tractive rolling contact goes back to the 1920s, and the mutually independent work of Carter [6] and Fromm [37]. Carter considered the two-dimensional case of an elastic cylinder in a state of tractive rolling on an elastic half-space, while Fromm considered the case of two elastic cylinders in rolling contact. Using the half-space assumption and the elastic theory of Love [26], Carter derived analytical expressions for the tangential contact traction distribution in terms of the rolling creepage¹. Here, the contact region is divided into two zones: the stick zone, adjacent to the leading edge of the contact region, and the slip zone, adjacent to the trailing edge [9, 7] (see Figure 2.1b).

The tangential contact traction distributions shown in Figure 2.1 are based on a consideration of the following conditions, which are fundamental properties of frictional contact, valid for every point on the contact surface: i) In the case of slip, the tangential traction reaches its limiting value: the product of the coefficient of friction and the normal pressure at the same point (da Vinci, Amontons, Coulomb), ii) in the case of stick, the slip (or the slip velocity) is zero and iii) the direction of the tangential contact traction always opposes the direction of the slip (or the slip velocity). In particular, in the case of tractive rolling contact, it may be shown that the occurrence of a region of slip adjacent to the leading edge would be inconsistent with condition iii, i.e. the tangential contact traction and the slip velocity would here be equidirectional [7].

¹The rolling creepage is a normalized measure of the nominal slip velocity in the contact region, see e.g. Johnson [7] or Paper D.

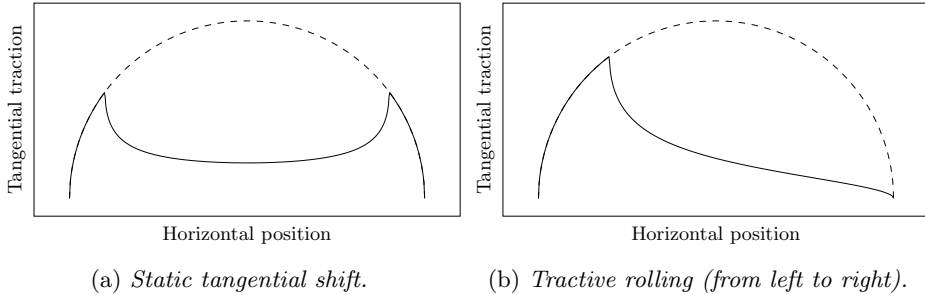


Figure 2.1: *Examples of tangential contact traction distributions across the contact region for two modes of tangential contact. Solid lines: partial slip. Dashed lines: full slip.*

The earliest models of three-dimensional, tractive rolling contact were presented in Johnson [38] and Vermeulen and Johnson [39]. Here, the stick region is assumed to be an elliptical region located adjacent to the leading edge. Other early approaches [40, 41] divide the contact surface into a set of thin, longitudinally aligned strips, each of which is subject to a treatment using a two-dimensional theory for tractive rolling.

2.2 Semi-analytical approaches

Semi-analytical contact models are characterized by the use of some version of Hertz theory in conjunction with a numerical methodology (e.g. fatigue/wear models, inelastic material models and/or the FE method). These methods are comparatively simple to implement and typically computationally efficient. However, despite efforts to expand the range of applicability of Hertz based approaches (see Section 2.1), they are inevitably constrained by their foundational assumptions, such as that of half-space geometries and typically quasistatic dynamics, a purely mechanical response, and elastic materials.

Semi-analytical approaches to the analysis of rolling contact are characterized by a reliance on analytical expressions for normal and tangential contact traction distributions obtained from Hertz and – in the case of tractive rolling – Carter theory. In one class of approaches, the analytical contact traction distributions (and possibly also internal strain and stress fields) are employed for the computation of e.g. inelastic responses [42, 43, 44] and/or evaluation of various damage criteria [45]. Another class of approaches instead employ the FE method to analyze the response to the analytically determined rolling contact loading. Examples include the analysis of elastic-plastic responses [46, 47] and thermomechanical phenomena [48, 49, 50].

2.3 BE approaches

The Boundary Element (BE) method [51] is a computational technique for the numerical solution of continuum mechanics problems. In this approach, the governing differential equations of the physical system under study are first reformulated into a system of

integral equations, whereupon the divergence theorem is used in order to rephrase all constituent volume integrals into boundary integrals. The discretization of the resulting system therefore requires a computational mesh to be constructed only on the boundary of the studied continuum.

The most prominent example of the use of the BE method for the analysis of frictional contact problems is the computational code CONTACT [8], which was developed and released by Kalker in 1982. This code is based on a boundary element formulation (or, as Kalker calls it, a *surface mechanics* formulation) of an extended version of the theory of Duvaut and Lions. The original theory [52] concerns a formulation of static frictional contact in terms of a variational complementary virtual work principle. Kalker extended this theory to the case of rolling contact [53], and developed the computational code DUVOROL, later superseded by CONTACT, on this basis. A comprehensive description of Kalker's theory, including extensions subsequent to 1982 [54, 55], is given in Kalker [9].

CONTACT is a sophisticated and robust framework for the analysis of three-dimensional frictional (static and rolling) contact problems. However, it is limited by a number of fundamental assumptions, including the half-space assumption, homogeneous and linear elastic or viscoelastic materials, and the absence of inertial effects in the dynamic response. The half-space assumption requires the contacting surfaces to be nominally flat and small with respect to characteristic dimensions of the contacting bodies. However, some classes of non-Hertzian contact surfaces, including rough and conforming surfaces, are supported.

CONTACT is still under continual development. For instance, recent efforts by Vollebregt and co-workers have resulted in an increase in the robustness, accuracy and computational efficiency of the program [56, 57]. Furthermore, the program has been expanded to new areas of applicability, such as the modelling of surface roughness, interfacial contaminants [57], and conformal contact [58].

2.4 FE approaches

2.4.1 Overview

After the emergence and popularization of the Finite Element (FE) method in the 1960s [59], the development of contact algorithms in the FE context soon followed. Early papers on the subject include Chan and Tuba [60] and Wilson and Parsons [61]. Instead of relying on idealized analytical expressions based on very specific geometrical and constitutive assumptions (as in Hertz theory), FE based approaches to computational contact mechanics take advantage of the discretized geometry of both of the contact surfaces, as well as that of the interiors of the contacting bodies, thus inheriting the versatility of the FE method. For instance, through a consideration of the kinematical interaction between the discretized surfaces, contact constraints may be evaluated in order to determine nodal contact forces. These may be included in the discrete FE equation system, which may then be solved in order to evaluate e.g. internal stress and strain fields. Apart from a geometrical versatility, the FE method offers substantial freedom in constitutive modelling, and readily allows for the modelling of other physical phenomena than the purely mechanical response, e.g. thermomechanical effects.

Today, the field of FE based computational contact mechanics has reached a high level of sophistication, and provides a wealth of options for contact algorithms and interface laws. The reader is referred to the famous book by Wriggers [62] for a comprehensive and well-referenced treatise on the subject.

2.4.2 ALE approaches

The application of the FE method to rolling contact problems goes back to the 1980s [63, 64, 65]. In particular, Oden and Lin [65] presents a relative kinematics framework for rolling contact in which an intermediate configuration, corresponding to the undeformed rolling body, is employed as a reference. The relationship between the relative kinematics approach of Oden and Lin and the ALE methods that saw regular use in fluid mechanics and fluid–structure interaction problems at the time (see Chapter 4) was first observed in Nackenhorst [66]. A subsequent paper by the same author [10] presents a complete mathematical formulation of mechanical rolling contact (including detailed statements of balance laws, weak forms and contact kinematics) in the context of an ALE kinematical description. The paper also emphasizes two significant complications associated with the ALE formulation of rolling contact. Specifically, these are related to the convective nature of the ALE description, and the related difficulty of tracking material points in the circumferential direction in the domain of the rolling body (see Section 4). This leads to complications both in the treatment of inelastic material response and in keeping track of relative slip distances. Both of these issues are addressed in Ziefle and Nackenhorst [67], in the context of stationary (steady-state), rolling contact on a rigid, plane surface.

In the aforementioned paper, relative slip distances are introduced as additional unknowns, and expressed as integrals of slip velocities that are restated in a convective form. Using these expressions, standard frictional contact laws may subsequently be employed.

Early approaches to the treatment of inelastic material behaviour in a convective kinematical framework typically followed one of two approaches: They either relied upon integration of material data around concentric rings in the undeformed domain [65, 68], thus imposing the requirement of a structured computational mesh, or they employed upwind-schemes in order to integrate the advection equation governing the transport of inelastic history parameters [69]. In Ziefle and Nackenhorst [67], a numerical scheme for the treatment of inelastic material response based on a *fractional step* method [70] is constructed. In this approach, the evolution equation for the inelastic history parameters is restated into a convective ALE form. Its solution is then divided into a series of steps: First, the evolution equation is solved while neglecting convective terms. After an intermediate smoothing step, in which the inelastic parameters are given a continuous representation in the arbitrarily structured mesh, the convective part of the evolution equation is finally used to transport the material history data through the computational domain in the direction of the convective flow. In this last step, a Time-Discontinuous Galerkin (TDG) approach is used to address numerical instability issues related to the convective form of the evolution equation.

In Suwannachit and Nackenhorst [71], a computational model for the analysis of rolling contact between a rubber tire and a rigid surface, based on an ALE kinematical description,

is presented. A sophisticated thermoviscoelastic constitutive model is employed, including rate-dependent response, large deformations, and strongly thermomechanical effects such as dissipative heating and temperature-dependent constitutive parameters (see also Nackenhorst, Ziefle, and Suwannachit [72] and Suwannachit [73]). Furthermore, the approach presented in Ziefle and Nackenhorst [67] for the treatment of inelastic material response is expanded to the thermomechanically coupled case. Here, a staggered approach is employed, wherein the equations governing the mechanical response, the thermal response, and the evolution of the inelastic history parameters are sequentially solved in each iteration.

3 Continuum thermomechanics

3.1 Governing equations

Continuum mechanics [74, 75, 76] is a branch of mechanics based on the assumption that physical bodies may be modelled as continuous media (or *continua*), i.e. they continuously fill the geometrical region in which they are contained. Of course, this model stands in stark contrast to the known nature of matter as a composition of atoms, which in turn mostly consist of empty space. Even at intermediate scales, many materials exhibit strong heterogeneities. For instance, polycrystalline metals are made up of an assemblage of often randomly oriented crystallites, or grains (with typical dimensions of the order of micrometers). The continuum assumption is nevertheless a useful and accurate description at *macroscopic* scales, i.e. larger scales at which subscale entities such as metallic grains are numerous enough so that their collective behaviour tend toward a mean constitutive response.

The physical state of a continuum is usually described using scalar or tensorial field quantities, defined for every point in the geometrical region occupied by the continuum, and also potentially time-dependent. These quantities may be kinematical (e.g. displacements and velocities), measures of strain or stress, or other macroscopic state variables such as temperature or density.

The continuum mechanics framework is amenable to a mathematical treatment using integral and differential calculus. With the help of these tools, fundamental physical laws may be stated in local forms, i.e. as partial differential equations valid for every point in the continuum. Together with constitutive relations (which describe material properties) and suitable initial and boundary conditions, these result in boundary value problems which may be solvable by analytical or numerical methods.

In *continuum thermomechanics* [74, 77, 78, 79], both mechanical and thermodynamic balance laws (potentially including thermomechanical coupling phenomena) are considered. In particular, this approach considers the law of *momentum balance* and the law of *conservation of energy* (or *energy balance*), which are local forms of Newton's second law and the first law of thermodynamics, respectively. The former is expressed in the Lagrangian (material) description as

$$\rho \mathbf{a} - \mathbf{P} \cdot \nabla - \mathbf{B} = 0, \quad (3.1)$$

where ρ is the density in the material domain, \mathbf{a} is the material acceleration, \mathbf{P} is the first Piola–Kirchhoff stress tensor, ∇ is the vector differential operator with respect to the material domain, and \mathbf{B} is the external body force per unit volume in the material domain. The energy balance equation is stated in terms of the Lagrangian description as

$$\rho\dot{u} = \dot{\mathbf{F}} : \mathbf{P} - \mathbf{q} \cdot \nabla + R, \quad (3.2)$$

where u is the mass-specific internal energy, \mathbf{F} is the deformation gradient, \mathbf{q} is the heat flux in the material domain and R is the external heat source per unit time and unit volume in the material domain. The dot notation (e.g. \dot{u}) denotes a material time derivative and $:$ is the tensorial double contraction operator: For two second order tensors \mathbf{A} and \mathbf{B} , $\mathbf{A} : \mathbf{B} = A_{ij}B_{ij}$.

It is noted that eq. (3.2) is expressed in terms of the thermodynamic state variables u and \mathbf{F} . This is just one of several possible options. By introducing the (mass-specific) Helmholtz free energy

$$\psi = u - s\theta, \quad (3.3)$$

(where s is the mass-specific entropy) it is possible to reformulate the equation so that it is instead stated in terms of \mathbf{F} and the absolute temperature θ . These state variables are experimentally observable and controllable (as opposed to e.g. u and s), and are thus a common choice of unknowns in which to express the energy balance equation.

For a thermoelastic material (which is characterized by the absence of dissipative stresses and internal, history-dependent parameters), the Helmholtz free energy may be regarded as a function of θ and \mathbf{F} with the properties

$$\begin{aligned} s &= -\frac{\partial\psi}{\partial\theta}, \\ \mathbf{P} &= \rho\frac{\partial\psi}{\partial\mathbf{F}}. \end{aligned} \quad (3.4)$$

Hence, \dot{u} may be expressed as

$$\begin{aligned} \dot{u} &= \frac{\partial\psi}{\partial\theta}\dot{\theta} + \frac{\partial\psi}{\partial\mathbf{F}} : \dot{\mathbf{F}} + \dot{s}\theta + s\dot{\theta} = \frac{1}{\rho}\mathbf{P} : \dot{\mathbf{F}} + \dot{s}\theta \\ &= \frac{1}{\rho}\mathbf{P} : \dot{\mathbf{F}} - \theta\frac{\partial^2\psi}{\partial\theta^2}\dot{\theta} - \theta\frac{\partial^2\psi}{\partial\theta\partial\mathbf{F}} : \dot{\mathbf{F}} = \frac{1}{\rho}\mathbf{P} : \dot{\mathbf{F}} + c_\epsilon\dot{\theta} + \frac{1}{\rho}\theta\boldsymbol{\beta} : \dot{\mathbf{F}}, \end{aligned} \quad (3.5)$$

where the mass-specific heat capacity at constant strain,

$$c_\epsilon := -\theta\frac{\partial^2\psi}{\partial\theta^2},$$

and the tensor

$$\boldsymbol{\beta} := -\rho\frac{\partial^2\psi}{\partial\theta\partial\mathbf{F}}$$

were defined. Hence, eq. (3.2) may be rewritten in terms of \mathbf{F} and θ as

$$\theta\boldsymbol{\beta} : \dot{\mathbf{F}} + \rho c_\epsilon\dot{\theta} + \mathbf{q} \cdot \nabla - R = 0. \quad (3.6)$$

This equation is commonly referred to as the *heat equation*.

Eqs. (3.1) and (3.6), again noted to be expressed in terms of a Lagrangian kinematical description, form the basis for the derivation of the ALE-formulation of the thermomechanically coupled equation system, given in Paper B.

3.2 Thermomechanical coupling

The local balance equations (3.1) and (3.6) are in general mutually coupled. For instance, the stress \mathbf{P} will in general depend on the temperature field θ . Consider for instance the case of a linear thermoelastic, isotropic material, assuming small temperature fluctuations. In this case, the constitutive relation may be stated as

$$\mathbf{P} = \mathbf{E} : [\mathbf{H} - \mathbf{H}^0] = \mathbf{E} : \mathbf{H} - 3K\alpha\theta\mathbf{I}, \quad (3.7)$$

where \mathbf{E} is the elasticity tensor, $\mathbf{H} = \mathbf{F} - \mathbf{I}$ is the displacement gradient, K is the bulk modulus, α is the thermal expansion coefficient and $\mathbf{H}^0 = \alpha\theta\mathbf{I}$ represents thermal strains, i.e. strains caused by *thermal expansion* of the material. In particular, for an unconstrained specimen,

$$\mathbf{P} = \mathbf{0} \Rightarrow \mathbf{H} = \mathbf{H}^0,$$

so that the temperature driven deformation is $\mathbf{F} = (1 + \alpha\theta)\mathbf{I}$.

The opposite thermomechanical coupling effect, which is represented by the term $\theta\boldsymbol{\beta}:\dot{\mathbf{F}}$ in eq. (3.6), represents the Gough–Joule effect [80, 81]: reversible heating/cooling of the material resulting from a nonzero strain rate. This effect is present both in polymeric and metallic materials (incidentally, it is negligible for thermoelastic materials [77]), but has very different causes and characteristics in each case. An atomistic explanation for the Gough–Joule effect in metals is given in Schweizer and Wauer [82].

There are several other forms of thermomechanical coupling phenomena than those appearing in the continuum thermomechanical field equations. As an example, inelastic deformation is an irreversible and hence dissipative process, which therefore generates an amount of heat that in some applications may not be negligible. Moreover, material phase transitions, being dependent on both temperature loads and pressures, are also thermomechanical in nature. Other examples of thermomechanical coupling phenomena include temperature-dependent constitutive parameters and – in contact mechanics applications – pressure-dependent thermal constitutive interface laws (see eg. Schrefler and Zavarise [83]).

In the frictional rolling contact implementation considered in Paper C and Paper D in this thesis, the dominating modes of thermomechanical coupling are those of frictional heat generation and interfacial heat transfer. The frictional heat generation is dependent on local sliding velocities, which are in turn determined by the material velocity field, accounting for the thermomechanical nature of this phenomenon. The interfacial heat transfer is in rolling contact situations dependent both on constitutive contact laws and on the rolling velocity. For instance, in railway mechanics applications, this is termed the *rail chill* effect: The higher the speed of the wheel over the rail, the larger the longitudinal distance across the rail over which heat is transferred during a given unit of time. This

leads to colder temperatures in the rail and thus a higher heat flux across the contact interface.

4 The ALE kinematical description

4.1 Brief history

The *Arbitrary Lagrangian–Eulerian* (ALE) kinematical description is a generalization of the classical Lagrangian and Eulerian descriptions, which may ideally be used to combine the advantages and avoid the weaknesses usually associated with the latter two descriptions. The first implementations of the ALE methodology go back to the early 1960s and 1970s, where it found use in a number of finite difference codes [84, 85, 86]. Early papers on the theory of ALE methods include Hirt, Amsden, and Cook [87] and Chan [88], which also discuss stabilization methods to mitigate numerical instability issues related to the convective ALE formulation of flow problems. The use of ALE methods in the context of FE applications soon followed [89, 90, 91], with the application to fluid–structure interaction problems as an early motivator.

4.2 Overview

In order to establish a *kinematical description* of a continuum [75, 74, 20], i.e. to describe its configuration and its motion in Euclidean space, two geometrical domains are commonly employed: the *undeformed, initial or material* configuration Ω_X and the *deformed, current or spatial* configuration Ω_x (see Figure 4.1). Ω_X represents the undeformed configuration of the continuum. It is usually associated with the fixed time $t = 0$, but does not thereby necessarily represent the actual configuration of the continuum at this or any other time. Ω_x represents the deformed configuration of the continuum at the current time t , and thus represents its actual arrangement in physical space. Both Ω_X and Ω_x are associated with coordinate systems that may either coincide or be chosen independently.

Due to the association of the undeformed configuration Ω_X with a fixed time, this configuration has the property that each coordinate $\mathbf{X} \in \Omega_X$ always corresponds to the same material point. Hence, parameterization of a given field quantity ψ as $\psi = \psi_X(\mathbf{X}, t)$ relates ψ to a particular material point \mathbf{X} , without any explicit reference to the position of this material point at the current time t . This approach of using the undeformed configuration Ω_X as the *reference configuration* characterizes the *Lagrangian* kinematical description. In contrast, each coordinate $\mathbf{x} \in \Omega_x$ corresponds to a fixed position in physical space (due to the association of Ω_x with the current time). Hence, parameterization of a field quantity ψ as $\psi = \psi_x(\mathbf{x}, t)$ relates ψ to a particular spatial point \mathbf{x} , without any explicit reference to the identity of the material point that happens to occupy the position \mathbf{x} at the current time t . This approach of using the deformed configuration Ω_x as the reference configuration characterizes the *Eulerian* kinematical description.

In order to enable a numerical treatment of the governing equations (for instance using the FE method), the continuum is discretized by introducing a computational mesh

in the chosen reference configuration. In the Lagrangian description, the computational mesh will move and deform with the continuum: its nodes will be attached to material points and its elements will represent the same material regions throughout the whole motion. This property makes the Lagrangian description very useful for keeping track of the evolution of history-dependent material parameters, and the motion of material boundaries. On the other hand, cases involving large deformations might result in a heavily distorted computational mesh. For this reason, the Lagrangian description is a common choice in solid mechanics applications, but is seldom used in fluid mechanics. In the Eulerian description, the computational mesh remains fixed in space, so that any motion of the continuum will result in convection of material points relative to the mesh. As a result, the Eulerian description is a suitable choice in cases involving large and/or complex and convoluted deformations (which are common in fluid mechanics applications), but ill-equipped to handle the tracking of history-dependent material data and material interfaces and boundaries. It is further noted that the inherently convective Eulerian description gives rise to nonsymmetric terms in the governing equations, which may lead to numerical instability issues (see Section 5).

The ALE kinematical description [20, 92] is a generalization of the Lagrangian and Eulerian descriptions in which the reference configuration (henceforth denoted by Ω_χ ; see Figure 4.1) may be chosen arbitrarily. Hence, this description provides complete freedom in the choice of the motion of the reference configuration relative to the continuum, and relative to physical space. In particular, the Lagrangian and Eulerian descriptions are obtained as special (extreme) cases when the ALE reference configuration Ω_χ is chosen as Ω_X (material-fixed) and Ω_x (space-fixed), respectively. It should here be noted that the Lagrangian description is the only one that is completely devoid of any relative motion (convection) between material points and coordinates in the reference domain. In particular, the expression for the material time derivative of a continuum field quantity is – in both the ALE and Eulerian descriptions – split into a convective term and a referential time derivative. For more information, see Donéa and Huerta [20], Donéa et al. [92], Nackenhorst [10] or Paper D.

Figure 4.1 shows a schematic illustration of the configuration of a continuum in the material domain (Ω_X), the spatial domain (Ω_x), and a particular choice of ALE domain (Ω_χ). The highlighted internal lines in the continuum (as well as its boundary) are material-fixed. Again, note that the coordinate system (shown in the bottom left in each of the three figures) may be chosen independently in each domain.

As mentioned previously, the ALE description can be used to combine the advantages of the Lagrangian and Eulerian descriptions, and in many cases circumvent their weaknesses. It can also be useful in cases where the motion is naturally divisible into separate kinematical components, one of which is known a priori (see e.g. Section 4.4). In any application of the ALE description, its success depends on the appropriate construction of the reference configuration (including its motion) for the particular problem at hand. Whenever possible, the motion of the reference configuration (and thus that of the computational mesh) is completely prescribed a priori. In other cases, the computational mesh is determined during the simulation based on some automatic remeshing algorithm. The latter might involve mesh regularization (smoothing) or adaptive mesh refinement [92].

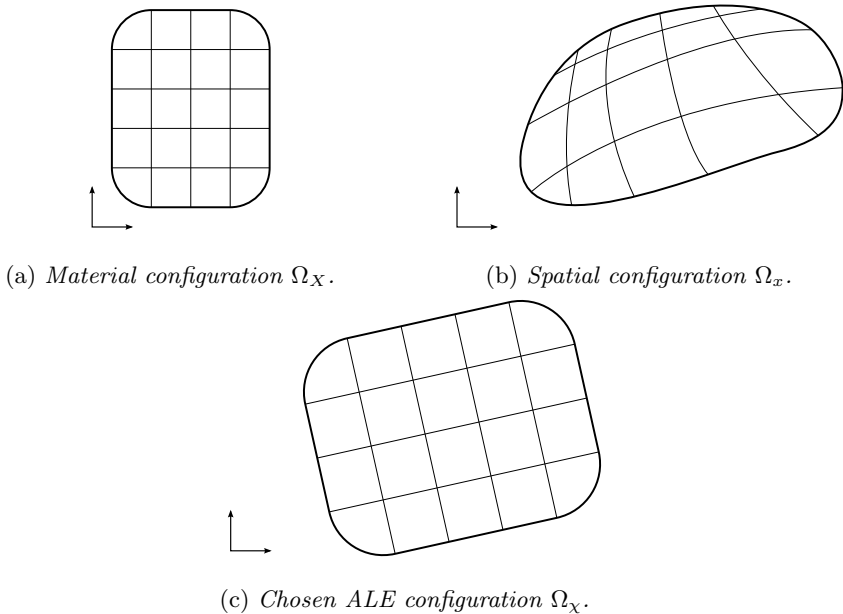


Figure 4.1: *The configuration of a continuum in each of the three domains Ω_X , Ω_x and Ω_χ .*

Examples of applications in which ALE methods are often more suitable than Lagrangian or Eulerian approaches include problems involving fluid–structure interaction [90, 93, 94], free surface flow [95, 96], metal forming [97] and cutting [98, 99] processes, and rolling contact (see Section 4.4).

4.3 One-dimensional example

Consider a one-dimensional, uncoupled version of the heat equation previously stated in eq. (3.6):

$$\rho c_\epsilon \dot{\theta} + \nabla q - R = 0. \quad (4.1)$$

Here, the dot notation (e.g. $\dot{\theta}$) again denotes a material time derivative and ∇ is the one-dimensional version of the material vector differential operator ∇ (see Section 3.1). The heat flux q is modelled using Fourier’s law:

$$q = -k \nabla \theta$$

and the external heat source R and the thermal conductivity k are taken as homogeneous.

The material configuration $\Omega_X \ni X$, as well as an artificial configuration $\hat{\Omega} \ni \hat{X}$ are now introduced. $\hat{\Omega}$ is identical to Ω_X , except that the former features a coordinate system

that translates with a constant velocity \bar{V} , so that

$$\hat{X} = \hat{\phi}(X, t) = X - \bar{V}t. \quad (4.2)$$

This relation shows that material points $X \in \Omega_X$ travel to the left as observed from the translating reference frame of $\hat{\Omega}$. The configuration $\hat{\Omega}$ is here considered to have no relation to the current configuration of the one-dimensional continuum. Therefore, this configuration may be interpreted as an artificial ALE domain. The kinematical description employed in this example is noted to be equivalent to the part of the kinematical description implemented in the appended papers that corresponds to the plate domain (see e.g. Paper D).

The material time derivative (see Section 2.1 in Paper D) of the temperature θ may now be expressed as follows in terms of the convected domain:

$$\dot{\theta} = \hat{\nabla}\theta(-\bar{V}) + d_t\theta, \quad (4.3)$$

where $\hat{\nabla}$ is the differential operator in $\hat{\Omega}$ and $d_t(\cdot) := \partial(\cdot)/\partial t|_{\hat{X}}$ denotes the time derivative in $\hat{\Omega}$. The ALE formulation of (4.1) may then be expressed as

$$\hat{\rho}c_\epsilon(-\bar{V}\hat{\nabla}\theta + d_t\theta) + \hat{\nabla}\hat{q} - \hat{R} = 0, \quad (4.4)$$

where

$$\hat{q} = -k\hat{\nabla}\theta$$

and $(\hat{\cdot})$ denotes quantities related to $\hat{\Omega}$. Since there is no deformation between the two domains Ω_X and $\hat{\Omega}$ (i.e. the deformation gradient $\partial\hat{\phi}(\hat{X}, t)/\partial X = 1$), it follows that $\hat{q} = q$, $\hat{\rho} = \rho$ and $\hat{R} = R$. Assuming a stationary response ($d_t\theta = 0$), the above equation may be rephrased as

$$\frac{\partial^2\theta}{\partial\hat{X}^2} + \frac{\hat{a}}{k}\frac{\partial\theta}{\partial\hat{X}} + \frac{\hat{R}}{k} = 0, \quad (4.5)$$

where $\hat{a} := \hat{\rho}c_\epsilon\bar{V}$. The solution to eq. (4.5) is

$$\theta(\hat{X}, t) = -\frac{\hat{R}}{\hat{a}}\hat{X} - C_1e^{-\hat{a}\hat{X}/k} + C_2, \quad (4.6)$$

where the constants C_1 and C_2 may be determined from the boundary conditions of the problem. The interval of interest in the following is $-L < \hat{X} < L$. Furthermore, homogeneous Dirichlet boundary conditions are imposed at $\hat{X} = \pm L$.

For illustration purposes, a non-dimensional counterpart of the problem and its solution is now considered, where the dimensionless parameters $L = \hat{\rho} = c_\epsilon = k = 1$ and $\hat{R} = 1000$ are employed. The temperature distribution is shown in Figure 4.2 for three distinct values of \bar{V} . The solution is noted to be characterized by an increased dissipation and a more substantial skewing in the direction of the convective flow, with increasing values of \bar{V} .

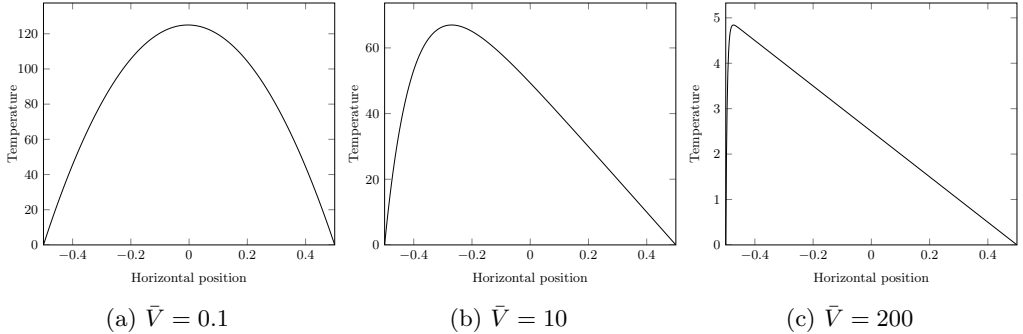


Figure 4.2: Analytical solution of the one-dimensional convected heat equation for three different values of the convective velocity \bar{V} .

4.4 Application to rolling contact

In the context of rolling contact mechanics, a Lagrangian kinematical description may be applicable in cases where rolling distances are short and velocities are low (or when the rolling motion can be considered to be quasistatic), so that the conditions in the contact region change little between consecutive time steps of the simulation. See for instance Galantucci and Tricarico [100], where a Lagrangian FE model is employed to model a hot rolling process. When rolling distances are large and velocities are high, however, a Lagrangian description (in which the computational mesh follows the motion of the continuum) leads to significant difficulties in describing the surface interaction during the rolling motion. For this reason, FE-based rolling contact models usually either adopt a contact-fixed (i.e. translating) frame of reference, or a relative-kinematics description of the rolling motion. In both cases, material points are considered to flow through the contact region via convection, although in different ways. As mentioned in Section 2.4.2, this formulation was given a more mathematically stringent treatment in Nackenhorst [10], in terms of an ALE description.

The ALE description employed in Nackenhorst [10] introduces an intermediate ALE reference domain that represents the undeformed configuration after a rigid body transformation. This transformation represents the nominal rigid body motion (translation and rotation) of the rolling body across the rolling surface. This way, the ALE kinematical description effectively decomposes the rolling motion into one nominal rigid body component (which may be determined a priori), and one corresponding to the actual deformation. It should here be noted that the kinematical description employed in the appended papers of this thesis is identical to the one presented in Nackenhorst [10], except for the fact that it involves a translating coordinate system that follows the rolling body in its motion (see e.g. Figure 1 in Paper D).

In the ALE description of rolling contact just described, the contact region in the reference domain (on both sides of the contact interface) is largely stationary throughout the rolling motion. This means that the same region in the computational mesh will always correspond to the region in contact, which allows for highly localized mesh refinement

(see e.g. Figure 4 in Paper D). As shown in Paper B, the ALE description also allows for linearization of the thermomechanical response. In the same paper, it is shown that for an isotropic, thermomechanical system, stationary (steady-state) rolling contact takes the form of a time-independent problem in the ALE context (a point which is also made in Nackenhorst [10]). Furthermore, it is noted that the ALE formulation allows for the compact modelling of the domain corresponding to the foundation¹ over which rolling takes place, regardless of the actual distance traversed during a simulation. The reason is that by the convective nature of the ALE description, the foundational domain is subject to continual in- and outflow of material across its artificial bounding edges. Thus, at any given time, the considered foundational domain corresponds to a section of the full material domain, that is located in the vicinity of the contact region. Finally, it is noted that in the case of thermomechanical contact, the velocity-dependence of the effect of convective cooling of the rolling domain (see Section 3.2), and related heat-partitioning behaviour, is inherent to the employed ALE description. This allows for velocity-independent contact interface modelling.

It is emphasized that the use of an ALE description for a thermomechanical system in rolling contact results in a significantly more complicated boundary value problem as compared to that of a Lagrangian formulation. To see this, compare the Lagrangian formulation of this problem (eqs. (4), (5), (13) and (15) in Paper B) with the ALE formulation of the same problem (eqs. (6), (12), (23) and (21) in Paper B). Accounting for transient rolling contact further complicates the picture, especially when control of driving forces is to be accommodated (see Paper D).

Being convective in nature, the ALE description is associated with potential difficulties regarding the tracking of history-dependent material parameters and material boundaries. In the case studied in the appended papers, all boundaries that are not in- or outflow boundaries follow the streamlines of the convective velocity field, hence avoiding the latter complications. Had this not been the case, any boundary irregularity would be transported in the direction of the convective flow as time progresses. This would necessitate special measures, such as frequent re-meshing to keep the mesh consistent with the geometry, likely outweighing any benefit gained from using the ALE description in the first place. Finally, computational issues such as numerical instabilities (see Paper B), and complications regarding the treatment of variable rolling velocities, as well as mixed control between these velocities and external driving forces (see Paper D), require special consideration.

¹In the two-dimensional simulations considered in the appended papers, the foundational domain is referred to as the "plate" domain

5 Numerical stabilization of convection–diffusion problems

5.1 Introduction

The most common weighted residual method used in FE formulations is the Galerkin¹ method, in which the weight functions of the weak (variational) formulation of the governing equations are the same as the approximation (trial) functions [101, 102]. For the common class of self-adjoint boundary value problems, this leads to a symmetric weak form, and hence to symmetric coefficient matrices in the FE formulation. In this case, it can be shown that the discrete solution to the Galerkin FE problem is optimal in the energy norm [103, 20]. This is known as the *Galerkin best approximation* property. In problems involving convection, the presence of the nonsymmetric convective operator means that the Galerkin best approximation guarantee is lost. In problems where convective effects dominate, very severe numerical inaccuracies may in fact arise.

Of particular interest in this thesis is the *diffusion–convection* problem², which is associated with the local equation

$$\mathbf{a} \cdot \nabla \theta - \nabla \cdot (k \nabla \theta) = R. \quad (5.1)$$

Here, \mathbf{a} (not to be confused with the acceleration in Section 3) is a first order tensor which is proportional to the convective velocity, θ is the unknown scalar field, k is a diffusion coefficient, and R is an external source term. The first and second terms above are identified as the convective and diffusive terms, respectively. When convective effects dominate over diffusive effects, the solution tends to feature thin boundary layers containing sharp gradients, in the vicinity of outflow boundaries for the convective flow. In these regions, the Galerkin shape functions are ill-suited to represent the shape of the solution. This leads to stability problems in the form of spurious node-to-node oscillations [20], where the solution and its derivative vary strongly in space. In contrast, in domains where the convective streamlines are closed, the solution to the convection–diffusion problem is not characterized by boundary layers. Instead, the dominating symptom of the failure of the Galerkin shape functions to capture the shape of the solution is erroneous numerical dissipation (see Paper B).

The only way to mitigate the aforementioned numerical instability problems in the standard Galerkin framework is by refinement of the mesh until the shape of the solution is adequately resolved. However, the degree of mesh refinement required increases rapidly with the Peclet number³ of the flow, rendering this approach untenable in most applications.

¹The surname, Russian in origin, is more accurately romanized as *Galyorkin*.

²Note from e.g. Paper B or Section 4.3 that the stationary, uncoupled version of the energy balance equation as expressed in the ALE context has the same form as eq. (5.1).

³The Peclet number is a dimensionless quantity that may be interpreted as a quantification of the degree to which convection dominates over diffusion for a given discretization.

5.2 Numerical stabilization methods

In order to address the numerical instability issues arising in convection-dominated flow problems in the context of a Galerkin FE formulation, a number of numerical stabilization methods have been developed. For an extensive summary, see Donéa and Huerta [20] or Codina [104].

In the appended papers B–D in this thesis, a thermomechanically coupled rolling contact problem expressed in terms of a convective ALE description is considered. It has been found that while the discretized momentum balance equation is not affected by numerical instability issues for the range of convective velocities of interest, the discretized energy balance equation is strongly affected. To address these problems, the SUPG method and a quasi RFB method are employed. These are described in further detail below.

5.2.1 The SUPG method

In order to understand the mechanisms behind numerical stabilization methods for convection–diffusion problems, it is instructive to begin by considering the one-dimensional version of the governing equation. In this case, it can be shown that the Galerkin FE formulation may be modified to obtain a nodally exact solution [20]. This modified scheme may equivalently be interpreted as stemming from the introduction of artificial diffusion in the strong form of the problem, or from the application of a modified test function – corresponding to a stronger weighting in the upstream direction – to the convective term in the weak form. The latter interpretation has inspired the concept of *upwind* schemes [105, 106].

In the generalization of the upwind scheme to the multi-dimensional case, it has been found to be important to apply numerical stabilization measures only along the streamlines of the convective flow. Otherwise, excessive numerical diffusion may be introduced. This has led to the concept of *streamline upwind* schemes. It is noted that these schemes are not variationally consistent: the correction to the test function is applied only to the convective term in the weak form. This shortcoming of the streamline upwind method motivated the development of the *Streamline-Upwind Petrov–Galerkin* (SUPG) method, which was introduced in Brooks and Hughes [19]. In the SUPG method, the test function

$$w^{\text{SUPG}} = w^{\text{G}} + \tau \mathbf{a} \cdot \nabla w^{\text{G}} \quad (5.2)$$

is used for all terms in the residual equation (note that the second term represents a directional derivative along a streamline of the convective flow). Here, w^{G} is the standard Galerkin test function and τ is the stabilization parameter (or the *intrinsic time scale*). τ depends both on the magnitude of the convective velocity and on a characteristic element size (see Donéa and Huerta [20] and Paper D). The choice of the latter is a non-trivial modelling consideration which may have a large influence on the performance of the SUPG method.

5.2.2 Bubble function approaches

In the context of the FE method, bubble function methods seek to enrich the functional space from which test and shape functions are chosen, by the introduction in each element of a function that vanishes on the element boundaries: a *bubble*. The shape of a given bubble function is parameterized via one or more degrees of freedom. Since the bubble vanishes on the boundaries of the element with which it is associated, these additional degrees of freedom may be reduced via the process of static condensation, so that they do not appear in the global equation system. It is emphasized, however, that the process of static condensation does not change the solution of the problem.

A Galerkin FE approach in which bubble functions have been introduced and their associated degrees of freedom then condensed may in its totality be interpreted as a numerical scheme in its own right. It should here be noted that in the special case where the bubble functions have the same functional shape as the FE test and shape functions (they may for instance be polynomials of the same order), this scheme is simply equivalent to a standard Galerkin method on an ("intelligently") enriched mesh [107].

As previously mentioned, numerical instability issues related to a Galerkin FE formulation of a convection-dominated flow problem arise as a result of the inability of the Galerkin scheme to resolve the shape of the solution, which involves thin boundary layers containing sharp gradients. By their nature as a subscale enrichment methodology, bubble function methods may – with a suitable choice of the enriched FE space – be employed to address such problems. It has in fact been found that bubble function approaches to numerical stabilization of convection–diffusion problems are closely related to streamline-upwind methods such as the SUPG method [108, 109, 110].

The Residual-Free Bubble (RFB) method [111, 112] is a special type of bubble function method in which the exact solution to the governing boundary value problem in each element (with homogeneous Dirichlet boundary conditions) is required. Static condensation is then employed, resulting in a numerical scheme that communicates the fine-scale behaviour to the coarse-scale problem. Incidentally, RFB methods have been shown to be a special case of the variational multiscale method [113]. This method, introduced in Hughes [114] and further developed in Hughes et al. [115] and Hughes and Sangalli [116], is a powerful computational methodology for the representation of multiscale phenomena, for which numerical stabilization of convection-dominated flows is but one possible application [20].

A problem associated with the RFB method is the difficulty associated with solving the subscale problem. An analytical solution is often not available, necessitating approximate schemes, which may be called *quasi residual-free bubble* methods. An example of such a scheme is given in Brezzi, Marini, and Russo [21]. Here, each triangular element in the considered two-dimensional domain is subdivided into three elements by the introduction of an extra node. Linear shape functions are used, thus resulting in a pyramid-shaped bubble function. The position of the extra node is chosen from a consideration of the direction and magnitude of the convective velocity field. The stabilization procedure discussed in Paper B is based on a similar methodology.

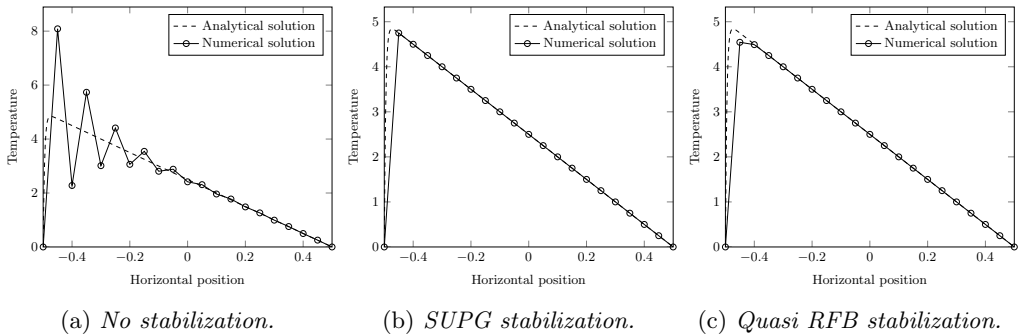


Figure 5.1: *FE solutions to the one-dimensional convected heat equation with and without numerical stabilization. The analytical solution is also included in each case. $\bar{V} = 200$*

5.3 One-dimensional example

In Section 4.3, the one-dimensional heat equation was restated in terms of a convective description. The analytical solution was plotted, and shown to be skewed in the direction of the convective flow. A Galerkin FE formulation of the problem, using piecewise linear shape functions, is now implemented in order to illustrate the previously discussed numerical instability issues associated with such an approach. The same parameters as in Section 4.3 are used, with $\bar{V} = 200$, and the one-dimensional domain is discretized using 20 equal-sized elements. The solution, shown in Figure 5.1a, clearly exhibits strongly oscillatory behaviour, culminating near the outflow boundary of the convective flow, where the exact solution exhibits sharp gradients.

Figure 5.1b shows the SUPG-stabilized solution. It is seen that this solution is completely devoid of numerically erroneous oscillatory behaviour. In fact, the SUPG method provides a nodally exact solution in the one-dimensional case.

In a final example, a quasi RFB method is implemented to stabilize the solution. In particular, each one-dimensional element is here subdivided into two elements by the introduction of an additional node. The position of this node is chosen to coincide with the stationary point of the exact solution of the heat equation, as considered on the element in question with homogeneous Dirichlet boundary conditions. The shape function associated with this node (i.e. the introduced bubble function) is chosen as a piecewise linear function (note that using the shape of the exact local solution for the bubble function would result in a pure RFB method). The extra degree of freedom in each element is eliminated via static condensation, so that a discrete system of the same size as in the previous two examples is obtained. Note that the fact that the employed bubble functions are of the same polynomial order as the Galerkin shape functions (together with the fact that static condensation does not influence the solution) means that the implemented quasi RFB method is exactly equivalent to a pure mesh refinement scheme, where the additional nodes coincide with the analytically computed positions. Figure 5.1c shows the solution to the quasi RFB-stabilized discrete problem. The spurious numerical oscillations are clearly eliminated, although a nodally exact response is not obtained.

6 Summary of appended papers

This section contains summaries of the contents of the appended papers. These summaries are followed by a table (Table 6.1) containing an overview of the set of features of the computational framework that was used for each appended paper.

Note that all appended papers have in common that they concern a theoretical and computational framework for rolling contact based on the FE method, an ALE kinematical description of the type presented in Nackenhorst [10], and a computational contact formulation based on methodologies described in Wriggers [62]. Further, they all consider a two-dimensional (plane strain) geometry corresponding to cylinder–plate rolling contact, and isotropic, homogeneous and linear (thermo-)elastic materials.

- **Paper A: Numerical evaluation of the transient response due to non-smooth rolling contact using an arbitrary Lagrangian–Eulerian formulation.**

In the first paper of this thesis, a purely mechanical version of the ALE-based computational framework is employed in a study of transient, frictionless rolling contact, featuring non-smooth surface profiles. The paper further implements non-reflecting boundary conditions at the in- and outflow boundaries of the considered plate domain. These are shown to be successful in preventing reflection of mechanical waves against the artificial boundaries of the plate. However, since these waves are found to have a limited influence on the overall stress distribution, these boundary conditions were not employed in later papers. The non-smooth surface profiles are modelled via modification of the gap functions of the contact formulation. The two surface profile shapes used in the numerical simulations are a sharp hole in the plate and a corrugation pattern based on actual field measurements. Numerical results are presented, and found to be in qualitative agreement with results in the literature.

- **Paper B: Finite element analysis of transient thermomechanical rolling contact using an efficient arbitrary Lagrangian–Eulerian description.**

This paper contains a comprehensive derivation of the ALE formulation of the fully transient, thermomechanically coupled boundary value problem, as well as its weak and FE forms. Relevant tensorial quantities (i.a. the first Piola-Kirchhoff stress tensor) are expressed in the ALE domain and shown to be free of explicit time-dependences in the isotropic case. Furthermore, mechanical and thermal boundary conditions are expressed in the ALE context and discussed in detail. The paper also contains an investigation of numerical instability issues related to the discretized energy balance equation. Specific numerical stabilization measures are proposed, and their performance is assessed. Numerical examples featuring transient, thermomechanical, frictionless rolling contact are presented, highlighting the influence of variations in thermal contact conductivity, rolling speed and external mechanical load on the contact interface heat flux.

- **Paper C: Finite element modelling of frictional thermomechanical rolling/sliding contact using an arbitrary Lagrangian–Eulerian formula-**

tion.

This paper extends the computational model to support frictional (tractive) rolling contact, although only allowing for control of the rolling velocities, and limited to a stationary (steady-state) analysis. The paper discusses particular characteristics of the frictional contact formulation as expressed in the ALE context, such as the fact that the velocity-dependence of interfacial heat transfer phenomena is captured inherently. Numerical examples show the model to be able to capture e.g. stick/slip behaviour, as well as a range of thermal phenomena, including the effect of convective cooling of the cylinder due to the contact with the plate.

- **Paper D: Finite element modelling of transient thermomechanical rolling contact featuring mixed control of the rigid body motion.**

In the final paper of this thesis, the ALE-based computational framework is finally extended to fully transient, thermomechanically coupled, frictional rolling contact. A computationally efficient methodology for mixed control between the ALE referential velocities (i.e. the rolling velocities) and their corresponding driving forces is developed and discussed in depth. Furthermore, complications related to the implementation of time-dependent convective velocities in the ALE framework are addressed. Numerical examples are presented where particular points of emphasis include dynamical effects in the vicinity of the contact region, and the time scales on which mechanical and thermal mechanisms operate.

Table 6.1: Overview of the set of features of the computational framework that was used for each appended paper. Here, a check mark indicates that a given feature is used, and a horizontal dash that the feature is not applicable, or required, for the considered situation.

	Paper A	Paper B	Paper C	Paper D
Thermomechanical coupling		✓	✓	✓
Friction			✓	✓
Transient dynamics	✓	✓		✓
Non-smooth surfaces	✓	✓		✓
Non-refl. boundary conditions	✓			
Numerical stabilization	—	✓	✓	✓
Variable rolling velocities				✓
Control of driving forces				✓

7 Conclusions and outlook

7.1 Contributions of the thesis

A theoretical and computational framework, based on an ALE kinematical description and aimed toward analysis of fully transient, thermomechanically coupled, frictional rolling contact between two deformable bodies, has been developed. Implemented features

include support for non-reflecting boundary conditions, irregular surface profiles, and mixed control between rolling velocities and corresponding driving forces. Numerical instability issues related to the convective ALE description of the energy balance equation are addressed using the Streamline-Upwind Petrov–Galerkin (SUPG) method and a variation of a known quasi Residual-Free Bubble (RFB) method.

The ALE-formulation of the thermomechanically coupled boundary value problem is derived and discussed in detail in Paper B. In particular, it is shown that for isotropic, homogeneous and thermoelastic materials, the push-forwards of relevant tensorial quantities (e.g. the Piola–Kirchhoff stress tensor and the heat flux tensor) to the ALE domain are independent of intrinsically time-dependent rigid body rotation tensors. This is noted to be a necessary condition for the time-independent nature of the ALE-formulation in the particular case of stationary rolling contact (for the given material properties).

The ALE description is noted to allow for velocity-independent modelling of the contact interface. In particular, the velocity-dependent effect of convective cooling of the rolling body, and subsequent heat partitioning between the rolling body and the foundation, is inherently captured by the convective kinematical description (see Paper C).

The modelling of the foundational body as deformable leads in the ALE context to a domain bounded on both sides by a pair of artificial boundaries, across which a continual convective material flow takes place. The convected mechanical and thermal boundary conditions that arise at these boundaries in the ALE formulation when prescribing natural tractions and fluxes, are shown in Paper B to be of the Robin type. Furthermore, mechanically non-reflecting boundary conditions were implemented at these boundaries (see Paper A). These were shown to be effective in eliminating spurious reflection of mechanical waves. However, the influence of these mechanical waves on the solution was noted to be more or less negligible, especially with regard to resultant contact forces.

The use of the ALE description is noted to result in an FE formulation wherein the constituent matrices and vectors depend on a set of convective velocity parameters. In transient simulations where these parameters vary in time, there consequently arises an apparent need to reassemble in each time step the system matrices and vectors that depend on these parameters. In Paper D, a methodology is developed for the computation of the FE system matrices as linear combinations of precomputed matrices, thus removing the need for their recomputation in each time step. The computation times for transient analyses are thus in general substantially decreased. In the same paper, a methodology for mixed control between rolling velocities and their corresponding driving forces is developed and discussed in detail.

Numerical simulations presented in the appended papers show the model to be able to capture e.g. fully transient stick/slip behaviour and negotiation of strongly non-smooth and even discontinuous surface profiles. Furthermore, a range of thermomechanical phenomena, including frictional heat generation and the effect of convective cooling of the cylinder due to the contact with the plate¹ can also be simulated by the developed model.

One of the main motivations for the development of the computational model has been for it to reach a state where it can be coupled to a multi-body vehicle dynamical framework – interfacing with the cylinder–plate model via the nominal rolling velocities,

¹It is noted that the numerical simulations in the appended papers consider the two-dimensional situation of cylinder–plate rolling contact.

or their corresponding driving forces. Although many applications would additionally require a generalization to three-dimensional geometries for an accurate representation of pertinent physical phenomena, this point can now be considered to have been reached. The construction of such a coupled model would result in a framework for vehicle dynamics analysis equipped with a versatile and sophisticated model for the contact interface. This would potentially enable high-resolution analysis of e.g. thermomechanical rolling contact fatigue, thermal damage phenomena, rolling noise generation, corrugation formation and stick/slip behaviour in the context of rolling–sliding contact interaction. The last application may for instance take advantage of the implemented methodology for mixed control between rolling velocities and driving forces. The dynamic stick/slip behaviour of the rolling system may in this way be evaluated in order to assess the proximity to sliding. Such analyses may for instance be used as a basis for assessing, in turn, the performance of automatic slip prevention systems.

7.2 Suggestions for future work

In the further development of the ALE-based computational model presented in this thesis, measures to increase its robustness and computational efficiency should take priority. In particular, the treatment of tangential contact is currently modelled using a regularized friction law (see Paper C), which is conducive to convergence problems and furthermore dependent on a velocity-dependent regularization parameter that is often very difficult to choose. An approach independent of numerical modelling parameters, e.g. a Lagrange multiplier method [62], would here be preferable. Another promising alternative – as yet only implemented for stationary rolling contact – is presented in Ziefle and Nackenhorst [67]. Here, relative slip distances are introduced as additional unknowns, and expressed as integrals of slip velocities that are restated in a convective form.

As discussed in Paper B, it has been found to be necessary to implement quadratic shape functions (in conjunction with a numerical stabilization scheme) in the domain of the rolling body in order to obtain a numerically accurate thermal response. Due to the employed monolithic solution scheme, this has the side-effect of requiring the use of quadratic shape functions also for the mechanical problem in this domain. The fact that the domain corresponding to the rolling surface implements linear shape functions thus results in a discrepancy, which complicates the contact formulation (see e.g. Paper B). On this basis, it is considered plausible that a staggered solution scheme, which allows for a separate spatial (and temporal) discretization between the mechanical and thermal problems, will prove advantageous.

In order to expand the range of practical applicability of the computational framework, e.g. toward modelling of realistic wheel–rail rolling contact situations, it will be necessary to implement support for three-dimensional geometries and inelastic material response. In this endeavour, some of the main challenges are believed to be the appropriate generalizations of the quasi RFB numerical stabilization scheme and the methodology for mixed control between rolling velocities and driving forces.

References

- [1] A. Draganis, F. Larsson, and A. Ekberg. Numerical evaluation of the transient response due to non-smooth rolling contact using an arbitrary Lagrangian–Eulerian formulation. *Proceedings of the Institution of Mechanical Engineers, Part J: Journal of Engineering Tribology* **226.1** (2012), 36–45. DOI: 10.1177/1350650111422015.
- [2] A. Draganis, F. Larsson, and A. Ekberg. Finite element analysis of transient thermomechanical rolling contact using an efficient arbitrary Lagrangian–Eulerian description. *Computational Mechanics* **54.2** (2014), 389–405. ISSN: 0178-7675. DOI: 10.1007/s00466-014-0992-6.
- [3] A. Draganis, F. Larsson, and A. Ekberg. Finite element modelling of frictional thermomechanical rolling/sliding contact using an arbitrary Lagrangian–Eulerian formulation. *Proceedings of the Institution of Mechanical Engineers, Part J: Journal of Engineering Tribology (in review)* (2014).
- [4] A. Draganis. “Finite element modelling of transient thermomechanical rolling contact featuring mixed control of the rigid body motion”. To be submitted for international publication.
- [5] H. Hertz. Über die berührung fester elastischer körper (On the contact of elastic solids). *J. reine und angewandte Mathematik* **92** (1882), 156–171.
- [6] F. W. Carter. On the action of a locomotive driving wheel. *Proceedings of the Royal Society of London. Series A* **112.760** (1926), 151–157. DOI: 10.1098/rspa.1926.0100.
- [7] K. L. Johnson. *Contact mechanics*. Cambridge University Press, 1987. ISBN: 9780521347969.
- [8] E. A. H. Vollebregt. *User guide for CONTACT, Vollebregt & Kalker’s rolling and sliding contact model*. Tech. rep. TR09-03, version 13.1. VORTech, Sept. 2012.
- [9] J. J. Kalker. *Three-dimensional elastic bodies in rolling contact*. Solid mechanics and its applications. Kluwer Academic Publishers, 1990. ISBN: 9780792307129.
- [10] U. Nackenhorst. The ALE-formulation of bodies in rolling contact: Theoretical foundations and finite element approach. *Computer Methods in Applied Mechanics and Engineering* **193** (2004), 4299–4322. DOI: 10.1016/j.cma.2004.01.033.
- [11] K. L. Johnson. The strength of surfaces in rolling contact. *Proceedings of the Institution of Mechanical Engineers, Part C: Journal of Mechanical Engineering Science* **203.3** (1989), 151–163. DOI: 10.1243/PIME_PROC_1989_203_100_02.
- [12] A. Ekberg and E. Kabo. Fatigue of railway wheels and rails under rolling contact and thermal loading—an overview. *Wear* **258.7–8** (2005), 1288–1300. ISSN: 0043-1648. DOI: 10.1016/j.wear.2004.03.039.
- [13] T. Vernersson et al. Wheel tread damage: A numerical study of railway wheel tread plasticity under thermomechanical loading. *Proceedings of the Institution of Mechanical Engineers, Part F: Journal of Rail and Rapid Transit* **224.5** (2010), 435–443. DOI: 10.1243/09544097JRR358.
- [14] T. Vernersson and R. Lundén. Temperatures at railway tread braking. Part 3: wheel and block temperatures and the influence of rail chill. *Proceedings of the*

- Institution of Mechanical Engineers, Part F: Journal of Rail and Rapid Transit* **221.4** (Jan. 2007), 443–454. ISSN: 0954-4097. DOI: 10.1243/09544097JRRT91.
- [15] E. Kabo, J. C. O. Nielsen, and A. Ekberg. Prediction of dynamic train–track interaction and subsequent material deterioration in the presence of insulated rail joints. *Vehicle System Dynamics* **44** (2006), 718–729. DOI: 10.1080/00423110600885715.
- [16] J. Sandström and A. Ekberg. Predicting crack growth and risks of rail breaks due to wheel flat impacts in heavy haul operations. *Proceedings of the Institution of Mechanical Engineers, Part F: Journal of Rail and Rapid Transit* **223.2** (Mar. 2009), 153–161. ISSN: 0954-4097. DOI: 10.1243/09544097JRRT224.
- [17] S. L. Grassie. Rail corrugation: Characteristics, causes, and treatments. *Proceedings of the Institution of Mechanical Engineers, Part F: Journal of Rail and Rapid Transit* **223.6** (2009), 581–596. DOI: 10.1243/09544097JRRT264.
- [18] J. C. O. Nielsen et al. Train-track interaction and mechanisms of irregular wear on wheel and rail surfaces. *Vehicle System Dynamics* **40.1-3** (2003), 3–54. DOI: 10.1076/vesd.40.1.3.15874.
- [19] A. N. Brooks and T. J. R. Hughes. Streamline upwind/Petrov-Galerkin formulations for convection dominated flows with particular emphasis on the incompressible Navier-Stokes equations. *Computer Methods in Applied Mechanics and Engineering* **32.1-3** (1982), 199–259. ISSN: 0045-7825. DOI: 10.1016/0045-7825(82)90071-8.
- [20] J. Donéa and A. Huerta. *Finite element methods for flow problems*. Wiley, 2003. ISBN: 9780471496663.
- [21] F. Brezzi, D. Marini, and A. Russo. Applications of the pseudo residual-free bubbles to the stabilization of convection-diffusion problems. *Computer Methods in Applied Mechanics and Engineering* **166.1-2** (1998). Advances in Stabilized Methods in Computational Mechanics, 51–63. ISSN: 0045-7825. DOI: [http://dx.doi.org/10.1016/S0045-7825\(98\)00082-6](http://dx.doi.org/10.1016/S0045-7825(98)00082-6).
- [22] K. L. Johnson. One hundred years of Hertz contact. *Proceedings of the Institution of Mechanical Engineers* **196.1** (1982), 363–378. DOI: 10.1243/PIME_PROC_1982_196_039_02.
- [23] S. P. Timoshenko and J. N. Goodier. *Theory of elasticity*. Engineering societies monographs. McGraw-Hill, 1951.
- [24] V. Cerruti. Ricerche intorno all’equilibrio de’corpi elastici isotropi. *Atti della R. Accademia dei Lincei. Memorie della Classe di scienze fisiche, matematiche e naturali* **13.3** (1882), 81–122.
- [25] J. Boussinesq. *Application des potentiels à l’étude de l’équilibre et du mouvement des solides élastiques*. Paris: Gauthier-Villars, 1885. ISBN: 9782853670715.
- [26] A. E. H. Love. *A treatise on the mathematical theory of elasticity*. New York: Dover Publications, 1944. ISBN: 0486601749.
- [27] G. M. L. Gladwell. *Contact problems in the classical theory of elasticity*. Mechanics of elastic and viscoelastic solids. Springer, 1980. ISBN: 9789028607606.
- [28] G. Lundberg and H. Sjövall. *Stress and deformation in elastic contacts*. Publication (Chalmers Tekniska Högskola). The Institution of Theory of Elasticity and Strength of Materials, Chalmers University of Technology, 1958.

- [29] E. Steuermann. On Hertz theory of local deformation of compressed bodies. *Comptes Rendus (Doklady) de l'Académie des Sciences de l'URSS* **80** (1939), 359–.
- [30] L. E. Goodman and L. M. Keer. The contact stress problem for an elastic sphere indenting an elastic cavity. *International Journal of Solids and Structures* **1.4** (1965), 407–415. ISSN: 0020-7683. DOI: [http://dx.doi.org/10.1016/0020-7683\(65\)90005-3](http://dx.doi.org/10.1016/0020-7683(65)90005-3).
- [31] B. Paul and J. Hashemi. Contact pressures on closely conforming elastic bodies. *Journal of Applied Mechanics* **48.3** (1981), 543–548. DOI: 10.1115/1.3157671.
- [32] K. L. Johnson, K. Kendall, and A. D. Roberts. Surface energy and the contact of elastic solids. *Proceedings of the Royal Society of London. A. Mathematical and Physical Sciences* **324.1558** (1971), 301–313. DOI: 10.1098/rspa.1971.0141.
- [33] K. L. Johnson. The correlation of indentation experiments. *Journal of the Mechanics and Physics of Solids* **18.2** (1970), 115–126. ISSN: 0022-5096. DOI: [http://dx.doi.org/10.1016/0022-5096\(70\)90029-3](http://dx.doi.org/10.1016/0022-5096(70)90029-3).
- [34] J. A. Greenwood and J. H. Tripp. The elastic contact of rough spheres. *Journal of Applied Mechanics* **34.1** (1967), 153–159. DOI: 10.1115/1.3157671.
- [35] C. Cattaneo. Sul contatto di due corpi elastici: distribuzione locale degli sforzi. *Rendiconti dell'Accademia nazionale dei Lincei* **27** (1938), 342–348, 434–436, 474–478.
- [36] R. D. Mindlin. Compliance of elastic bodies in contact. *Journal of Applied Mechanics* **16** (1949), 259–268.
- [37] H. Fromm. *Berechnung des schlupfes beim rollen deformierbarer scheiben*. Technische Hochschule zu Berlin, 1927.
- [38] K. L. Johnson. The effect of a tangential contact force upon the rolling motion of an elastic sphere on a plane. *Journal of Applied Mechanics* **25** (1958), 339–346.
- [39] P. J. Vermeulen and K. L. Johnson. Contact of nonspherical elastic bodies transmitting tangential forces. *Journal of Applied Mechanics* **31.2** (1964), 338–340. DOI: 10.1115/1.3629610.
- [40] D. J. Haines and E. Ollerton. Contact stress distributions on elliptical contact surfaces subjected to radial and tangential forces. *Proceedings of the Institution of Mechanical Engineers* **177.1** (1963), 95–114. DOI: 10.1243/PIME_PROC_1963_177_014_02.
- [41] J. J. Kalker. “On the rolling contact of two elastic bodies in the presence of dry friction”. PhD thesis. Delft University of Technology, 1967.
- [42] J. E. Merwin and K. L. Johnson. An analysis of plastic deformation in rolling contact. *Proceedings of the Institution of Mechanical Engineers* **177.1** (1963), 676–690. DOI: 10.1243/PIME_PROC_1963_177_052_02.
- [43] A. F. Bower and K. L. Johnson. Plastic flow and shakedown of the rail surface in repeated wheel-rail contact. *Wear* **144.1–2** (1991), 1–18. ISSN: 0043-1648. DOI: [http://dx.doi.org/10.1016/0043-1648\(91\)90003-D](http://dx.doi.org/10.1016/0043-1648(91)90003-D).
- [44] Y. Jiang and H. Sehitoglu. Rolling contact stress analysis with the application of a new plasticity model. *Wear* **191.1–2** (1996). 4th International Conference on Contact Mechanics and Wear of Rail-Wheel Systems, 35–44. ISSN: 0043-1648. DOI: [http://dx.doi.org/10.1016/0043-1648\(95\)06663-2](http://dx.doi.org/10.1016/0043-1648(95)06663-2).

- [45] Y. Jiang and H. Sehitoglu. A model for rolling contact failure. *Wear* **224.1** (1999), 38–49. ISSN: 0043-1648. DOI: 10.1016/S0043-1648(98)00311-1.
- [46] V. Bhargava, G. T. Hahn, and C. A. Rubin. An elastic-plastic finite element model of rolling contact, part 1: Analysis of single contacts. *Journal of Applied Mechanics* **52.1** (1985), 67–74. DOI: 10.1115/1.3169028.
- [47] B. Xu and Y. Jiang. Elastic-plastic finite element analysis of partial slip rolling contact. *Journal of Tribology* **124.1** (Mar. 2001), 20–26. DOI: 10.1115/1.1395630.
- [48] S. M. Kulkarni, C. A. Rubin, and G. T. Hahn. Elasto-plastic coupled temperature-displacement finite element analysis of two-dimensional rolling-sliding contact with a translating heat source. *Journal of Tribology* **113.1** (Jan. 1991), 93–101.
- [49] K. Dang Van, M. H. Maitournam, and B. Prasil. Elastoplastic analysis of repeated moving contact – application to railways damage phenomena. *Wear* **196.1–2** (1996), 77–81. ISSN: 0043-1648. DOI: 10.1016/0043-1648(95)06864-3.
- [50] C. H. Gao et al. Stress analysis of thermal fatigue fracture of brake disks based on thermomechanical coupling. *Journal of Tribology* **129.3** (Dec. 2006), 536–543. DOI: 10.1115/1.2736437.
- [51] J. H. Kane. *Boundary element analysis in engineering continuum mechanics*. Prentice Hall, 1994. ISBN: 9780130869272.
- [52] G. Duvaut and J. L. Lions. *Inequalities in mechanics and physics*. Grundlehren der mathematischen Wissenschaften. Springer-Verlag, 1976. ISBN: 9783540073277.
- [53] J. J. Kalker. The computation of three-dimensional rolling contact with dry friction. *International Journal for Numerical Methods in Engineering* **14.9** (1979), 1293–1307. ISSN: 1097-0207. DOI: 10.1002/nme.1620140904.
- [54] J. J. Kalker. Two algorithms for the contact problem in elastostatics. *Proceedings International Symposium on Contact Mechanics and Wear of Rail-Wheel systems* (), 101–120.
- [55] J. J. Kalker. Contact mechanical algorithms. *Communications in Applied Numerical Methods* **4.1** (1988), 25–32. ISSN: 1555-2047. DOI: 10.1002/cnm.1630040105.
- [56] E. A. H. Vollebregt. Refinement of Kalker’s rolling contact model. *Proceedings of the 8th International Conference on Contact Mechanics and Wear in Rail/Wheel Systems* (2009), 149–156.
- [57] E. A. H. Vollebregt and H. M. Schuttelaars. Quasi-static analysis of two-dimensional rolling contact with slip-velocity dependent friction. *Journal of Sound and Vibration* **331.9** (2012), 2141–2155. ISSN: 0022-460X. DOI: <http://dx.doi.org/10.1016/j.jsv.2012.01.011>.
- [58] E. A. H. Vollebregt and G. Segal. Solving conformal wheel-rail rolling contact problems. *Vehicle System Dynamics* **52**.sup1 (2014), 455–468. DOI: 10.1080/00423114.2014.906634.
- [59] O. C. Zienkiewicz, R. L. Taylor, and J. Z. Zhu. *The finite element method: Its basis and fundamentals*. Amsterdam Boston: Butterworth-Heinemann, 2013. ISBN: 1856176339.
- [60] S. K. Chan and I. S. Tuba. A finite element method for contact problems of solid bodies — Part I. Theory and validation. *International Journal of Mechanical Sciences* **13.7** (1971), 615–625. ISSN: 0020-7403. DOI: [http://dx.doi.org/10.1016/0020-7403\(71\)90032-4](http://dx.doi.org/10.1016/0020-7403(71)90032-4).

- [61] E. A. Wilson and B. Parsons. Finite element analysis of elastic contact problems using differential displacements. *International Journal for Numerical Methods in Engineering* **2.3** (1970), 387–395. ISSN: 1097-0207. DOI: [10.1002/nme.1620020307](https://doi.org/10.1002/nme.1620020307).
- [62] P. Wriggers. *Computational contact mechanics*. Springer, 2006. ISBN: 9783540326083.
- [63] I. Zeid and J. Padovan. Finite element modeling of rolling contact. *Computers & Structures* **14.1–2** (1981), 163–170. ISSN: 0045-7949. DOI: [http://dx.doi.org/10.1016/0045-7949\(81\)90098-5](http://dx.doi.org/10.1016/0045-7949(81)90098-5).
- [64] J. Padovan. Finite element analysis of steady and transiently moving/rolling nonlinear viscoelastic structure—I. Theory. *Computers & Structures* **27.2** (1987), 249–257. ISSN: 0045-7949. DOI: [http://dx.doi.org/10.1016/0045-7949\(87\)90093-9](http://dx.doi.org/10.1016/0045-7949(87)90093-9).
- [65] J. T. Oden and T. L. Lin. On the general rolling contact problem for finite deformations of a viscoelastic cylinder. *Computer Methods in Applied Mechanics and Engineering* **57.3** (1986), 297–367. ISSN: 0045-7825. DOI: [http://dx.doi.org/10.1016/0045-7825\(86\)90143-X](http://dx.doi.org/10.1016/0045-7825(86)90143-X).
- [66] U. Nackenhorst. On the finite element analysis of steady state rolling contact. *Contact Mechanics — Computational Techniques* (1993), 53–60. DOI: [10.2495/CON930071](https://doi.org/10.2495/CON930071).
- [67] M. Ziefle and U. Nackenhorst. Numerical techniques for rolling rubber wheels: treatment of inelastic material properties and frictional contact. *Computational Mechanics* **42.3** (2008), 337–356. ISSN: 0178-7675. DOI: [10.1007/s00466-008-0243-9](https://doi.org/10.1007/s00466-008-0243-9).
- [68] L. Nasdala et al. An efficient viscoelastic formulation for steady-state rolling structures. *Computational Mechanics* **22.5** (1998), 395–403. ISSN: 0178-7675. DOI: [10.1007/s004660050371](https://doi.org/10.1007/s004660050371).
- [69] P. Le Tallec and C. Rahier. Numerical models of steady rolling for non-linear viscoelastic structures in finite deformations. *International Journal for Numerical Methods in Engineering* **37.7** (1994), 1159–1186. ISSN: 1097-0207. DOI: [10.1002/nme.1620370705](https://doi.org/10.1002/nme.1620370705).
- [70] D. J. Benson. An efficient, accurate, simple ale method for nonlinear finite element programs. *Computer Methods in Applied Mechanics and Engineering* **72.3** (1989), 305–350. ISSN: 0045-7825. DOI: [http://dx.doi.org/10.1016/0045-7825\(89\)90003-0](http://dx.doi.org/10.1016/0045-7825(89)90003-0).
- [71] A. Suwannachit and U. Nackenhorst. A novel approach for thermomechanical analysis of stationary rolling tires within an ALE-kinematic framework. *Tire Science and Technology* **41.3** (2013), 174–195.
- [72] U. Nackenhorst, M. Ziefle, and A. Suwannachit. “Finite element techniques for rolling rubber wheels”. *Elastomere Friction*. Ed. by D. Besdo et al. Vol. 51. Lecture Notes in Applied and Computational Mechanics. Springer Berlin Heidelberg, 2010, pp. 123–163. ISBN: 978-3-642-10656-9. DOI: [10.1007/978-3-642-10657-6_5](https://doi.org/10.1007/978-3-642-10657-6_5).
- [73] A. Suwannachit. “Thermomechanical analysis of tire rubber compounds in rolling contact”. PhD thesis. Hannover, 2013. ISBN: 978-3-935732-34-5.
- [74] G. A. Holzapfel. *Nonlinear solid mechanics: a continuum approach for engineering*. Wiley, 2000. ISBN: 9780471823193.

- [75] J. Bonet and R. D. Wood. *Nonlinear continuum mechanics for finite element analysis*. Cambridge University Press, 2008. ISBN: 9781139467544.
- [76] J. E. Marsden and T. J. R. Hughes. *Mathematical foundations of elasticity*. Dover Civil and Mechanical Engineering Series. Dover, 1994. ISBN: 9780486678658.
- [77] N. S. Ottosen and M. Ristinmaa. *The mechanics of constitutive modeling*. Elsevier, 2005. ISBN: 9780080446066.
- [78] H. Ziegler. *An introduction to thermomechanics*. North-Holland series in applied mathematics and mechanics. North-Holland Pub. Co., 1983. ISBN: 9780444865038.
- [79] R. B. Hetnarski and R. Eslami. *Thermal stresses – Advanced theory and applications*. Solid Mechanics and Its Applications. Springer, 2008. ISBN: 9781402092466.
- [80] J. Gough. A description of a property of caoutchouc, or Indian rubber; with some reflections on the cause of the elasticity of this substance. *Memoirs of the Literary and Philosophical Society of Manchester* **1** (1805), 288–295.
- [81] J. P. Joule. On some thermo-dynamic properties of solids. *Philosophical Transactions of the Royal Society of London* **149** (1859), 91–131. DOI: 10.1098/rstl.1859.0005.
- [82] B. Schweizer and J. Wauer. Atomistic explanation of the Gough-Joule-effect. *The European Physical Journal B - Condensed Matter and Complex Systems* **23.3** (2001), 383–390. ISSN: 1434-6028. DOI: 10.1007/s100510170058.
- [83] B. A. Schrefler and G. Zavarise. Constitutive laws for normal stiffness and thermal resistance of a contact element. *Computer-Aided Civil and Infrastructure Engineering* **8.4** (1993), 299–308. ISSN: 1467-8667. DOI: 10.1111/j.1467-8667.1993.tb00215.x.
- [84] W. F. Noh. *CEL: A time dependent, two space dimensional, coupled Eulerian-Lagrange code*. Aug. 1963. DOI: 10.2172/4621975.
- [85] J. G. Trulio. *Theory and structure of the AFTON codes*. Defense Technical Information Center, 1966.
- [86] A. A. Amsden and C. W. Hirt. *YAQUI, an Arbitrary Lagrangian-Eulerian computer program for fluid flow at all speeds*. LA-5100. United States. Defense Nuclear Agency and U.S. Atomic Energy Commission: Los Alamos Scientific Laboratory of the University of California, 1973.
- [87] C. W. Hirt, A. A. Amsden, and J. L. Cook. An arbitrary Lagrangian-Eulerian computing method for all flow speeds. *Journal of Computational Physics* **14.3** (1974), 227–253. ISSN: 0021-9991. DOI: 10.1016/0021-9991(74)90051-5.
- [88] R. K. C. Chan. A generalized arbitrary Lagrangian–Eulerian method for incompressible flows with sharp interfaces. *Journal of Computational Physics* **17.3** (1975), 311–331. ISSN: 0021-9991. DOI: [http://dx.doi.org/10.1016/0021-9991\(75\)90055-8](http://dx.doi.org/10.1016/0021-9991(75)90055-8).
- [89] J. Donea, P. Fasoli-Stella, and S. Giuliani. Lagrangian and Eulerian finite element techniques for transient fluid–structure interaction problems. *Proceedings of 4th International conference on structural mechanics in reactor technology* (1977).
- [90] T. Belytschko, J. M. Kennedy, and D. F. Schoeberle. Quasi-Eulerian finite element formulation for fluid-structure interaction. *Journal of Pressure Vessel Technology-transactions of The Asme* **102** (1 1980), 62–69. DOI: 10.1115/1.3263303.

- [91] T. J. Hughes, W. K. Liu, and T. K. Zimmermann. Lagrangian-Eulerian finite element formulation for incompressible viscous flows. *Computer Methods in Applied Mechanics and Engineering* **29.3** (1981), 329–349. ISSN: 0045-7825. DOI: [10.1016/0045-7825\(81\)90049-9](https://doi.org/10.1016/0045-7825(81)90049-9).
- [92] J. Donéa et al. “Arbitrary Lagrangian–Eulerian Methods”. *Encyclopedia of Computational Mechanics*. John Wiley & Sons, Ltd, 2004. ISBN: 9780470091357. DOI: [10.1002/0470091355.ecm009](https://doi.org/10.1002/0470091355.ecm009).
- [93] M. Souli, A. Ouahsine, and L. Lewin. ALE formulation for fluid–structure interaction problems. *Computer Methods in Applied Mechanics and Engineering* **190.5–7** (2000), 659–675. ISSN: 0045-7825. DOI: [http://dx.doi.org/10.1016/S0045-7825\(99\)00432-6](http://dx.doi.org/10.1016/S0045-7825(99)00432-6).
- [94] Q. Zhang and T. Hisada. Analysis of fluid–structure interaction problems with structural buckling and large domain changes by ALE finite element method. *Computer Methods in Applied Mechanics and Engineering* **190.48** (2001), 6341–6357. ISSN: 0045-7825. DOI: [http://dx.doi.org/10.1016/S0045-7825\(01\)00231-6](http://dx.doi.org/10.1016/S0045-7825(01)00231-6).
- [95] A. Huerta and W. K. Liu. Viscous flow with large free surface motion. *Computer Methods in Applied Mechanics and Engineering* **69.3** (1988), 277–324. ISSN: 0045-7825. DOI: [10.1016/0045-7825\(88\)90044-8](https://doi.org/10.1016/0045-7825(88)90044-8).
- [96] H. Braess and P. Wriggers. Arbitrary Lagrangian Eulerian finite element analysis of free surface flow. *Computer Methods in Applied Mechanics and Engineering* **190.1-2** (2000), 95–109. ISSN: 0045-7825. DOI: [10.1016/S0045-7825\(99\)00416-8](https://doi.org/10.1016/S0045-7825(99)00416-8).
- [97] R. Boman and J.-P. Ponthot. Finite element simulation of lubricated contact in rolling using the arbitrary Lagrangian–Eulerian formulation. *Computer Methods in Applied Mechanics and Engineering* **193.39–41** (2004). `jcetitlej`The Arbitrary Lagrangian-Eulerian Formulation;`ce:titlej`, 4323–4353. ISSN: 0045-7825. DOI: <http://dx.doi.org/10.1016/j.cma.2004.01.034>.
- [98] M. Movahhedy, M. S. Gadala, and Y. Altintas. Simulation of the orthogonal metal cutting process using an arbitrary Lagrangian–Eulerian finite-element method. *Journal of Materials Processing Technology* **103.2** (2000), 267–275. ISSN: 0924-0136. DOI: [http://dx.doi.org/10.1016/S0924-0136\(00\)00480-5](http://dx.doi.org/10.1016/S0924-0136(00)00480-5).
- [99] L. Olovsson, L. Nilsson, and K. Simonsson. An ALE formulation for the solution of two-dimensional metal cutting problems. *Computers & Structures* **72.4–5** (1999), 497–507. ISSN: 0045-7949. DOI: [http://dx.doi.org/10.1016/S0045-7949\(98\)00332-0](http://dx.doi.org/10.1016/S0045-7949(98)00332-0).
- [100] L. M. Galantucci and L. Tricarico. Thermo-mechanical simulation of a rolling process with an FEM approach. *Journal of Materials Processing Technology* **92–93** (1999), 494–501. ISSN: 0924-0136. DOI: [10.1016/S0924-0136\(99\)00242-3](https://doi.org/10.1016/S0924-0136(99)00242-3).
- [101] N. S. Ottosen and H. Petersson. *Introduction to the finite element method*. Prentice Hall, 1992. ISBN: 9780134738772.
- [102] R. D. Cook et al. *Concepts and applications of finite element analysis*. New York, NY: Wiley, 2001. ISBN: 978-0471356059.
- [103] S. C. Brenner and L. R. Scott. *The mathematical theory of finite element methods*. Ed. by J. E. Marsden, L. Sirovich, and S. S. Antman. 3rd ed. Vol. 15. Texts in

- applied mathematics. Springer, 2008. ISBN: 978-0-387-75933-3. DOI: 10.1007/978-0-387-75934-0.
- [104] R. Codina. Comparison of some finite element methods for solving the diffusion-convection-reaction equation. *Computer Methods in Applied Mechanics and Engineering* **156**.1–4 (1998), 185–210. ISSN: 0045-7825. DOI: 10.1016/S0045-7825(97)00206-5.
- [105] J. C. Heinrich et al. An ‘upwind’ finite element scheme for two-dimensional convective transport equation. *International Journal for Numerical Methods in Engineering* **11**.1 (1977), 131–143. ISSN: 1097-0207. DOI: 10.1002/nme.1620110113.
- [106] T. J. R. Hughes. A simple scheme for developing ‘upwind’ finite elements. *International Journal for Numerical Methods in Engineering* **12**.9 (1978), 1359–1365. ISSN: 1097-0207. DOI: 10.1002/nme.1620120904.
- [107] F. Brezzi et al. Link-cutting bubbles for the stabilization of convection-diffusion-reaction problems. *Mathematical Models and Methods in Applied Sciences* **13**.3 (2003). cited By (since 1996)25, 445–461. DOI: 10.1142/S0218202503002581.
- [108] G. Rogé. “On the approximation and the convergence acceleration in the finite element numerical simulation of compressible viscous flows”. PhD thesis. Université Paris, 1990.
- [109] F. Brezzi et al. A relationship between stabilized finite element methods and the Galerkin method with bubble functions. *Computer Methods in Applied Mechanics and Engineering* **96**.1 (1992), 117–129. ISSN: 0045-7825. DOI: 10.1016/0045-7825(92)90102-P.
- [110] C. Baiocchi, F. Brezzi, and L. P. Franca. Virtual bubbles and Galerkin-least-squares type methods (Ga.L.S.) *Computer Methods in Applied Mechanics and Engineering* **105**.1 (1993), 125–141. ISSN: 0045-7825. DOI: 10.1016/0045-7825(93)90119-I.
- [111] L. P. Franca, A. Nesliturk, and M. Stynes. On the stability of residual-free bubbles for convection-diffusion problems and their approximation by a two-level finite element method. *Computer Methods in Applied Mechanics and Engineering* **166**.1–2 (1998). Advances in Stabilized Methods in Computational Mechanics, 35–49. ISSN: 0045-7825. DOI: [http://dx.doi.org/10.1016/S0045-7825\(98\)00081-4](http://dx.doi.org/10.1016/S0045-7825(98)00081-4).
- [112] F. Brezzi, L. P. Franca, and A. Russo. Further considerations on residual-free bubbles for advective-diffusive equations. *Computer Methods in Applied Mechanics and Engineering* **166**.1–2 (1998). Advances in Stabilized Methods in Computational Mechanics, 25–33. ISSN: 0045-7825. DOI: [http://dx.doi.org/10.1016/S0045-7825\(98\)00080-2](http://dx.doi.org/10.1016/S0045-7825(98)00080-2).
- [113] F. Brezzi et al. $b = \int G$. 1996.
- [114] T. J. R. Hughes. Multiscale phenomena: Green’s functions, the Dirichlet-to-Neumann formulation, subgrid scale models, bubbles and the origins of stabilized methods. *Computer Methods in Applied Mechanics and Engineering* **127**.1–4 (1995), 387–401. ISSN: 0045-7825. DOI: 10.1016/0045-7825(95)00844-9.
- [115] T. J. R. Hughes et al. The variational multiscale method—A paradigm for computational mechanics. *Computer Methods in Applied Mechanics and Engineering* **166**.1–2 (1998). Advances in Stabilized Methods in Computational Mechanics, 3–24. ISSN: 0045-7825. DOI: [http://dx.doi.org/10.1016/S0045-7825\(98\)00079-6](http://dx.doi.org/10.1016/S0045-7825(98)00079-6).

- [116] T. Hughes and G. Sangalli. Variational multiscale analysis: the fine-scale Green's function, projection, optimization, localization, and stabilized methods. *SIAM Journal on Numerical Analysis* **45.2** (2007), 539–557. DOI: 10.1137/050645646.

Part II
Appended Papers A–D

Paper A

Numerical evaluation of the transient response due to non-smooth rolling contact using an arbitrary Lagrangian–Eulerian formulation

Numerical evaluation of the transient response due to non-smooth rolling contact using an arbitrary Lagrangian–Eulerian formulation

A Draganis*, F Larsson, and A Ekberg

Department of Applied Mechanics, Chalmers University of Technology, Gothenburg, Sweden

The manuscript was received on 28 January 2011 and was accepted after revision for publication on 17 May 2011.

DOI: 10.1177/1350650111422015

Abstract: A theoretical and numerical framework to evaluate rolling contact using an arbitrary Lagrangian–Eulerian (ALE) formulation is established. A finite element formulation is implemented featuring cylinder–plate contact, automated mesh refinement, non-reflecting boundary conditions, and the ability to incorporate surface roughness through user-defined gap functions. Presented examples include rolling contact on a corrugated surface and negotiation of a surface discontinuity. Sensitivity and validation analyses are presented and show the model to be robust and the trends in parametric responses to be reasonable as compared to results in literature. Owing to the ALE formulation, the model can be kept very compact and the computational demands very modest.

Keywords: rolling contact, transient analysis, finite element method, arbitrary Lagrangian–Eulerian

1 INTRODUCTION

The numerical modelling of rolling contact can, simplistically, be classified into two approaches: setting out from semi-analytical contact modelling or based on finite element (FE) simulations. If one focuses on normal contact, the first approach typically adopts a Hertzian contact formulation, whereas an FE approach typically adopts a contact formulation involving Lagrangian multipliers or a penalty-based method. A Hertzian approach is computationally efficient, but has drawbacks regarding its generality since it presumes (among other things) elastic material response, smooth and continuous profiles, and a relatively small contact patch. More details can be found in literature [1, 2].

In contrast, the FE method is very versatile regarding both geometry of the contacting components and the material response. On the other hand, the simulations are computationally expensive, in particular if the simulations should feature rolling over longer distances. This is due to the requirement for a dense FE mesh in the contact patch and the fact that the location of contact shifts as the rolling progresses. Further, the rolling motion will introduce the need to account for large displacements.

To alleviate these drawbacks, the approach adopted in this study is to employ an arbitrary Lagrangian–Eulerian (ALE) approach. Here, a computational domain consisting of the roller and a small part of the plate on which it is rolling is defined. Such an approach significantly reduces the size of the numerical model and related computational efforts, as detailed in section 4.

Considering purely mechanical wheel–rail contact, most research is devoted to quasi-static loading conditions and a (classical) Lagrangian description, where the material domain is chosen as reference.

*Corresponding author: Department of Applied Mechanics, Chalmers University of Technology, SE-412 96 Gothenburg, Sweden.
email: andreas.draganis@chalmers.se

However, in Dang Van *et al.* [3], elastic–plastic analysis of rail is carried out based on an ALE formulation. This allows for material flowing through the computational domain and thus studying the response under a moving load without explicitly modelling a large domain of the rail. Furthermore, in Chang *et al.* [4], the full three-dimensional (3D) wheel–rail contact situation is analysed using a similar framework. However, none of these papers address the dynamic situation. The dynamic effects of wheel–rail contact irregularities are significant and have been presented in a simplified form using measured transfer functions between irregularities and different components in Thompson [5]. The influence has further been assessed through numerical simulation and measurement [6–9].

The employed 2D model is valid under conditions where line contact is a good approximation. For conditions resulting in more elliptic contact patches, it should be considered as a first approximation.

The novel features of the employed model include a synthesis of computational frameworks: the application of non-reflecting boundary conditions in an ALE formulation of rolling contact and application of the ALE formulation to operational conditions featuring transient rolling contact dynamics under non-smooth (i.e. corrugated or discontinuous) contact conditions, modelled by an offset in the pertinent contact conditions [5].

2 MATHEMATICAL MODEL

2.1 Model description

A 2D model of a hollow cylinder rolling on a plate is studied (Fig. 1). The model features plane strain and an isotropic, homogeneous, and linear elastic material. Pure rolling and constant velocity of the

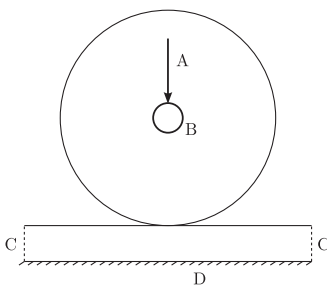


Fig. 1 Schematic illustration of the mechanical model: A, applied load; B, cylinder hub (rigid elements); C, plate domain ends (non-reflecting boundary conditions); and D, plate base (fixed in all degrees of freedom)

cylinder centre is assumed. An ALE description of motion is used, in which the reference frame of the computational domain translates with the cylinder. At the (non-physical) vertical boundaries of the plate, non-reflecting boundary conditions are imposed. The base of the plate is fixed while the top of the plate and the outer boundary of the cylinder is free. The inner boundary of the cylinder (the hub) is modelled to be rigid and is fixed in the horizontal direction.

The axle load acting on the cylinder is modelled as a vertical load applied to the hub. The static weights of cylinder, plate, and (in relevant cases) point masses are neglected, whereas their inertia is accounted for. Figure 1 outlines geometry, boundary conditions, and load case used for the employed model.

2.2 Kinematical description

An ALE formulation of motion is employed [10, 11]. In the current implementation, two intermediate configurations are utilized in addition to the reference ('undeformed') configuration, $\Omega_X \ni X$, and the current ('deformed') configuration, $\omega_x \ni x$. The first intermediate configuration is denoted as $\Omega_{\hat{X}} \ni \hat{X}$. The map from Ω_X to $\Omega_{\hat{X}}$ accounts for *rotation* of the cylinder and a *translation* of the plate. The second intermediate configuration is denoted as $\omega_{\hat{x}} \ni \hat{x}$. The map from $\Omega_{\hat{X}}$ to $\omega_{\hat{x}}$ accounts for the *deformation* of cylinder and plate. Both intermediate configurations feature a moving reference frame that follows the cylinder. The map from $\omega_{\hat{x}}$ to ω_x accounts for pure translation of the system in going back to the original fixed reference frame.

The maps between the configurations are formulated as $\hat{X} = \hat{\phi}(X, t)$, $\hat{x} = \hat{\phi}(\hat{X}, t)$, $x = \check{\phi}(\hat{x}, t)$, and $x = \varphi(X, t)$, so that $\varphi = \check{\phi} \circ \hat{\phi} \circ \hat{\phi}$. Figure 2 shows a schematic illustration of the employed configurations with their intermediary maps.

Since the maps $\hat{X} = \hat{\phi}(X, t)$ and $x = \check{\phi}(\hat{x}, t)$ can be expressed *a priori* from knowledge of the

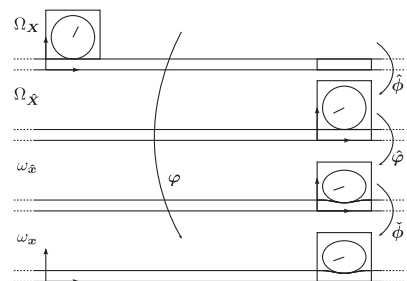


Fig. 2 Illustration of configurations and maps relevant to the employed ALE description

translational and rotational motions of the cylinder along the plate, the Lagrangian problem of finding the map $\mathbf{x} = \varphi(\hat{\mathbf{X}}, t)$ (or the displacement $\mathbf{u}(\hat{\mathbf{X}}, t) = \varphi(\hat{\mathbf{X}}, t) - \hat{\mathbf{X}}$) can be narrowed down to the ALE problem of finding the map $\hat{\mathbf{x}} = \hat{\varphi}(\hat{\mathbf{X}}, t)$ (or the displacement $\hat{\mathbf{u}}(\hat{\mathbf{X}}, t) = \hat{\varphi}(\hat{\mathbf{X}}, t) - \hat{\mathbf{X}}$).

2.3 Equation of motion

The local balance of momentum equation with respect to a volume element in the initial configuration $\Omega_{\mathbf{X}}$ is

$$\rho_{\mathbf{X}} \mathbf{a} - \mathbf{P} \cdot \nabla_{\mathbf{X}} = \mathbf{B} \quad \text{in } \Omega_{\mathbf{X}} \quad (1)$$

where \mathbf{P} is the first Piola–Kirchhoff stress tensor, $\rho_{\mathbf{X}}$ the density in the initial configuration, \mathbf{B} the external body force per unit volume (in the initial configuration), and \mathbf{a} the acceleration: $\mathbf{a} = D_{tt}\mathbf{x} = D_{tt}\mathbf{u}$, where $D_t(\cdot) \equiv \partial(\cdot)/\partial t|_{\hat{\mathbf{x}}}$, $D_{tt}(\cdot) \equiv \partial^2(\cdot)/\partial t^2|_{\hat{\mathbf{x}}}$. $\nabla_{\mathbf{X}}$ is the gradient operator with respect to $\Omega_{\mathbf{X}}$. Boundary conditions are imposed as

$$\mathbf{P} \cdot \mathbf{N} = \mathbf{T} \quad \text{on } \partial\Omega_{\mathbf{X},N} \quad (2)$$

$$\mathbf{u} = \mathbf{g} \quad \text{on } \partial\Omega_{\mathbf{X},D} \quad (3)$$

where \mathbf{N} is the outward normal, \mathbf{T} the external traction per unit area with respect to $\Omega_{\mathbf{X}}$, and \mathbf{g} the known displacements.

In terms of the ALE description, the boundary value problem is stated as[†]

$$\begin{aligned} \rho_{\hat{\mathbf{x}}} \left[\ddot{\hat{\mathbf{X}}} + d_{tt}\hat{\mathbf{u}} + 2 \left[(d_t\hat{\mathbf{u}}) \otimes \hat{\mathbf{V}} \right] \cdot \bar{\mathbf{v}} + \hat{\mathbf{F}} \cdot (D_t\bar{\mathbf{v}}) \right. \\ \left. + \hat{\mathbf{G}} : (\bar{\mathbf{v}} \otimes \bar{\mathbf{v}}) \right] - \hat{\mathbf{P}} \cdot \hat{\mathbf{V}} - \hat{\mathbf{B}} = 0 \quad \text{in } \Omega_{\hat{\mathbf{x}}} \end{aligned} \quad (4)$$

$$\hat{\mathbf{P}} \cdot \hat{\mathbf{N}} = \hat{\mathbf{T}} \quad \text{on } \partial\Omega_{\hat{\mathbf{x}},N} \quad (5)$$

$$\hat{\mathbf{u}} = \hat{\mathbf{g}} \quad \text{on } \partial\Omega_{\hat{\mathbf{x}},D} \quad (6)$$

where $d_t(\cdot) \equiv \partial(\cdot)/\partial t|_{\hat{\mathbf{x}}}$, $d_{tt}(\cdot) \equiv \partial^2(\cdot)/\partial t^2|_{\hat{\mathbf{x}}}$, $\hat{\mathbf{F}} \equiv \hat{\mathbf{x}} \otimes \hat{\mathbf{V}}$, $\hat{\mathbf{G}} \equiv \hat{\mathbf{x}} \otimes \hat{\mathbf{V}} \otimes \hat{\mathbf{V}}$, $\hat{\mathbf{X}}$ the translation of the cylinder centre and $\bar{\mathbf{v}} = D_t\hat{\mathbf{X}}$ the convective velocity; (\cdot) denotes quantities related to $\Omega_{\hat{\mathbf{x}}}$.

2.4 Contact formulation

In this contribution, frictionless contact is studied. The employed contact formulation is based on a standard Lagrange multiplier method [11], which involves evaluation of *gap functions* for all cylinder nodes that are candidates for contact. Each gap function represents the distance of the corresponding cylinder node from the plate surface (or the negative of the

penetration distance through the surface). Instances of negative gap functions give rise to contact forces in the form of Lagrange multipliers (required to be compressive), introduced as additional unknowns of the problem. Additional constraint equations are also added, requiring that the gap functions are zero.

To simulate irregular surface profiles, these gap functions are modified by an arbitrary offset function on the surface of the plate mesh for the purposes of contact evaluation: in effect, contact is checked against this modified surface rather than against the plate mesh surface [5]. Figure 3 illustrates this: the solid line represents the boundary of the plate mesh and the dotted line the modified surface, on the basis of which the gap functions are evaluated.

2.5 Non-reflecting boundary conditions

In order to prevent reflection of propagating mechanical waves at the non-physical ends of the plate domain, a boundary condition that allows the transmission of plane waves of specified propagation direction is imposed [12]. In short, the known relation between spatial and temporal derivatives of the displacement function, valid for plane waves, is imposed at the given boundaries. This means that the traction term in the weak form will be expressed in terms of velocity instead of strain, which leads to a contribution to the damping matrix (instead of the stiffness matrix) in the FE formulation. In the current implementation, the propagation direction of the elastic waves at the vertical ends of the plate is assumed to be perpendicular to these boundaries for all simulations performed.

3 NUMERICAL IMPLEMENTATION

3.1 Mesh and model parameters

A FE formulation of the problem is implemented in MATLAB. The element type used is a linear triangular element with two degrees of freedom per node: horizontal and vertical displacements. The employed mesh (containing 3282 elements and 1757 nodes) is shown in Fig. 4. The mesh of the cylinder is constructed from a coarse basic mesh that is refined successively in a series of gradually smaller domains centred at the point of initial contact. The tolerance for element size is defined to guarantee three to five



Fig. 3 Schematic illustration of the plate domain with a superimposed surface profile offset

^{*} $\hat{\mathbf{X}}$ held fixed.

[†] \otimes denotes the dyadic product.

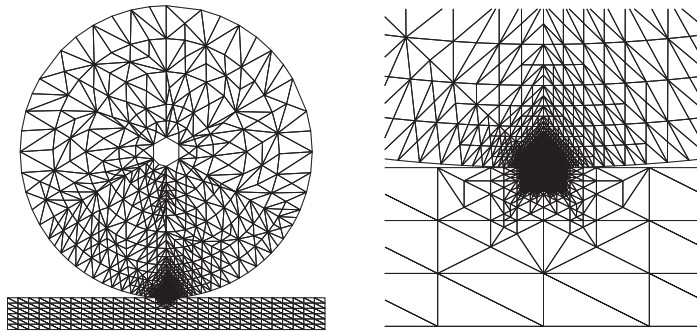


Fig. 4 The mesh, along with a zoomed-in view of the refined contact region

elements across the analytically determined contact patch (of size d_c) in the resulting mesh. Finally, three global refinements are performed, after which all nodes are remapped radially so that the outer nodes describe a circle.

The initial mesh of the plate domain features 31 and 7 nodes in the horizontal and vertical directions, respectively. The mesh is then refined locally in a rectangular area centred at the point of initial contact and extending a distance $2d_c$ horizontally and d_c vertically (Fig. 4). The minimum size for an element in the final mesh of the plate is 1.5 times the size of the smallest element in the cylinder mesh.

All mesh refinements are performed according to Rivara's longest-edge refinement technique [13], whereby the aspect ratio of the elements is controlled.

A standard parameter set-up, chosen to reflect typical values encountered in a train-track interaction setting, is now defined and employed for all subsequent simulations unless otherwise stated. Material parameters for cylinder and plate are: Young's modulus $E=200$ GPa, Poisson's ratio $\nu=0.3$, and density $\rho_X=8000$ kg/m³. Outer and inner radii of the cylinder are $r_o=460$ mm and $r_i=46$ mm, respectively, the height of the plate $h=10$ cm, and the width of the plate domain is chosen as $b=1$ m.

The applied force, $P=4.7$ MN/m, results in a contact pressure peak of $p_0=1$ GPa and a contact patch size of 7 mm, according to Hertzian theory.

The velocity of the cylinder (and thus the velocity of the reference frame of the computational domain) is chosen as $\bar{v}=100$ km/h. The rotational velocity of the cylinder is then \bar{v}/r_o , due to the assumption of pure rolling.

For the transient simulations, a Crank–Nicholson time integration scheme is used with a time step of $\Delta t=5 \cdot 10^{-5}$ s. In each transient simulation, the solution to the corresponding static problem is used as the start configuration. Rayleigh damping is applied

to the system with a damping matrix of $\underline{C}=\alpha_0\underline{M}+\alpha_1\underline{K}$, with $\alpha_0=0$, $\alpha_1=10^{-4}$ s, whereby the relative modal damping for the lowest eigenfrequency of the system becomes 11 per cent. The reason for setting the mass-proportional damping coefficient to zero is to have the damping affect only high-frequency oscillations.

3.2 Sensitivity and validation

A mesh convergence study is performed featuring a sinusoidally corrugated plate with an amplitude of 5 μ m and a wavelength 5 cm. The (steady state) amplitude of the vertical contact force evaluated on the cylinder is normalized by the standard mesh magnitude. This normalized contact force amplitude is denoted by \bar{F}_{Cy} .

Mesh parameters varied are the number of global refinements of the cylinder mesh, n_r , and the number of nodes in the horizontal direction of the mesh of the plate (before local refinement), n_{nx} . Table 1 gives the results of the study. The conclusion is that an increase in mesh resolution in the chosen mesh does not significantly influence the results. Based on the results of this study, the standard configuration was chosen to feature $n_r=3$ and $n_{nx}=31$.

The sensitivity to a change in chosen time step size Δt is investigated and the results are presented in Table 2. Here, \bar{F}_{Cy} corresponds to normalization with respect to $\Delta t=5 \cdot 10^{-5}$ s. Based on the results, the standard configuration was chosen to feature $\Delta t=5 \cdot 10^{-5}$ s.

The width of the plate domain should represent an acceptable trade-off between compactness of the computational domain and numerical accuracy (with respect to quantities of interest). A comparative study is performed in which the width of the computational domain of the plate, b , and the type of boundary condition at the plate domain ends (free

or non-reflecting) are varied. The same measure is used for the comparison as above, except that \bar{F}_{Cy} now corresponds to normalization with respect to the standard case of $b=1$ m and non-reflecting boundary conditions. As observed from Table 3, both the choice of boundary condition and the magnitude of b seems to be insignificant regarding the magnitude of \bar{F}_{Cy} for the parametric ranges studied.

The influence of the non-reflecting boundary conditions can better be demonstrated by studying the flux of mechanical energy. The model employed for the study is illustrated in Fig. 5. An element width of 1/30 m and a time step 10^{-5} s is employed. A vertical point load with a sinusoidally varying magnitude is applied on the surface. The frequency is $5 \cdot 10^4$ rad/s and the load is applied for 1/4 of a period. Three cases are studied:

- (a) a domain coinciding with the shaded area ($b=1$ m) with non-reflecting boundary conditions at the ends;

- (b) a larger domain of width $4b$ (Fig. 5) with free boundary conditions at the ends;
- (c) a reference case featuring a domain of width b with free boundaries.

Figure 6 shows the mechanical energy contained in the shaded area of Fig. 5 versus time, normalized with respect to the value of the energy (for case 3) immediately after the load has been removed.

The presumption is that case 2 will provide a ‘true’ reference, which – in a suitably chosen time window – ideally is unaffected by waves reflected from the boundaries (located at the distance $4b/2$ from the point load). That is, the better the performance of the non-reflecting boundary conditions, the more similar the response between cases 1 and 2. Start and end times of the plot in Fig. 6 correspond to the instants in time when the external load is removed and when a theoretical P-wave reaches the end of the larger domain, respectively. The solid and dashed vertical lines correspond to the instants in

Table 1 Influence on normalized contact force \bar{F}_{Cy} of the FE mesh as characterized by the number of global refinements of the cylinder mesh, n_r , and the number of nodes in the horizontal direction of the plate mesh, n_{nx}

n_r	n_{nx}	No. of elements	\bar{F}_{Cy}
1	11	729	1.28
1	31	1021	1.12
3	11	2820	1.13
3	31	3282	1
3	61	4044	0.97
4	31	5994	0.99
4	61	7540	0.96

Table 2 Influence of time step size Δt on normalized contact force \bar{F}_{Cy}

Δt (s)	\bar{F}_{Cy}
10^{-5}	1.01
$5 \cdot 10^{-5}$	1
10^{-4}	0.96

Table 3 Influence on normalized contact force \bar{F}_{Cy} of the width of the computational domain of the plate, b , and the adopted boundary condition at the plate ends

b (m)	Boundary condition at ends	\bar{F}_{Cy}
0.6	Free	1.00
0.6	Non-reflecting	1.00
1	Non-reflecting	1
4	Free	1.00
4	Non-reflecting	1.00

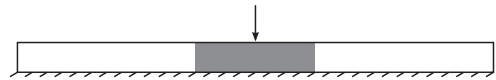


Fig. 5 Model employed to study the content of mechanical energy under varying boundary conditions. The upper surface is free whereas the lower surface is fixed in all degrees of freedom

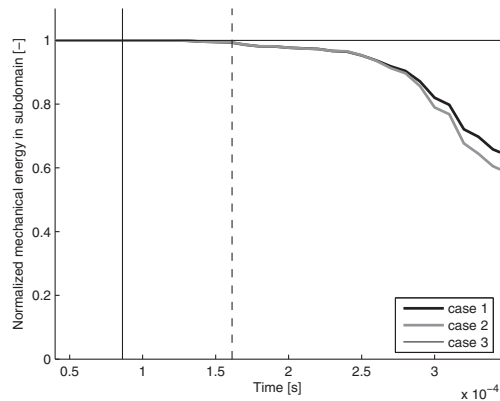


Fig. 6 Normalized mechanical energy content in the shaded subdomain of Fig. 5 as a function of time for the three configurations studied. The legend corresponds to the non-vertical curves. The solid and dashed vertical lines correspond to the instants in time when theoretical P- and S-waves (respectively) reach the end of the smaller domain

time when theoretical P- and S-waves (respectively) reach the end of the smaller domain.

Regarding the influence of the distributed static weight of the cylinder, it can be noted that the vertical force applied to the cylinder hub is 4.7 MN/m, whereas the total weight of the cylinder corresponds to 52 kN/m. Thus, neglecting the latter is reasonable.

In order to validate the numerical model versus Hertzian contact theory, a simulation was performed with $n_r = 5$ and $n_{nx} = 61$. The resulting peak contact pressure was 96.8 per cent of the corresponding value obtained from Hertzian contact theory. Increasing the width and the height of the plate domain by a factor of five (while keeping node spacing constant) – in order to more closely match the Hertzian half-plane assumption – this figure increased to 99.7 per cent. The agreement is deemed to be satisfying.

4 RESULTS

To evaluate the dynamic response, three plate profile configurations are employed in the study. Typical values for train-track interaction are used for the parameters.

1. A corrugated plate featuring a sinusoidal profile with an amplitude of 5 μm and a wavelength 5 cm.
2. A corrugated plate with a roughness spectrum based on field measurements of rail corrugation in a curve in the Stockholm metro system [14]. The roughness spectrum, shown in Fig. 7, has been rescaled to make the highest occurring amplitude roughly 5 μm .
3. A plate featuring a sharp discontinuity of width 5 mm (Fig. 14).

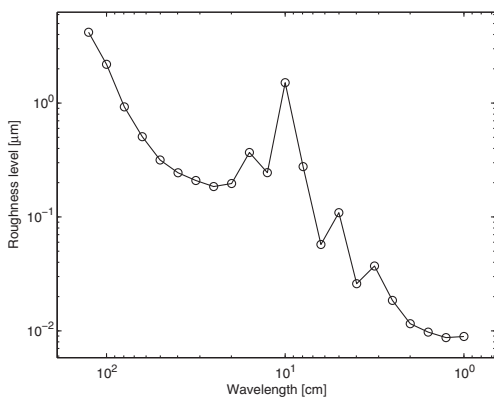


Fig. 7 Roughness level spectrum of the corrugation pattern used as the plate profile of type 2

For results presented in the form of probability density graphs of the vertical contact force (evaluated on the cylinder), the probability density p corresponding to a given force interval ΔP is plotted against the midpoint of the interval. Here

$$p = \frac{n}{\Delta P \cdot N} \tag{7}$$

where n is the number of time increments with a contact force magnitude within the given interval and N the total number of time increments.

Figures 8 and 9 show probability density graphs for a plate profile of type 2 (roughness spectrum) with the velocity (\bar{v}) and applied load (P) as varied parameters.

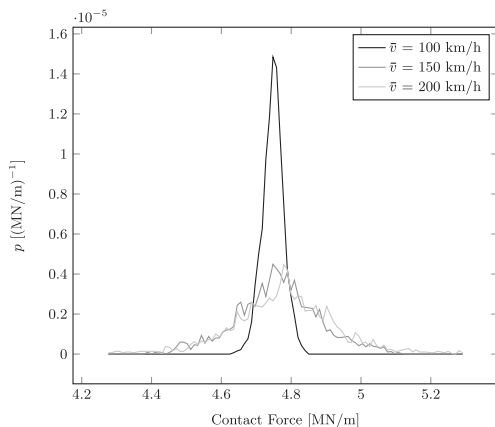


Fig. 8 Probability density graph of contact force magnitudes for varying velocity, \bar{v} , of the rolling cylinder

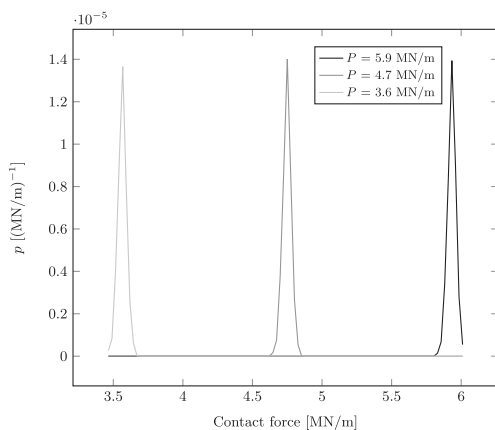


Fig. 9 Probability density graph of contact force magnitudes for varying applied load magnitude, P

Further, Fig. 10 gives the probability density graph for simulations featuring a point mass (M) rigidly attached to the inner boundary of the cylinder. It is emphasized that the addition of the point mass affects only the inertia of the system: no corresponding static weight is added. It is seen how an altered operational velocity or size of an added point mass will affect the dynamic response towards an increased influence of inertial effects, whereas an altered contact load magnitude will only shift the resulting response corresponding to the change in

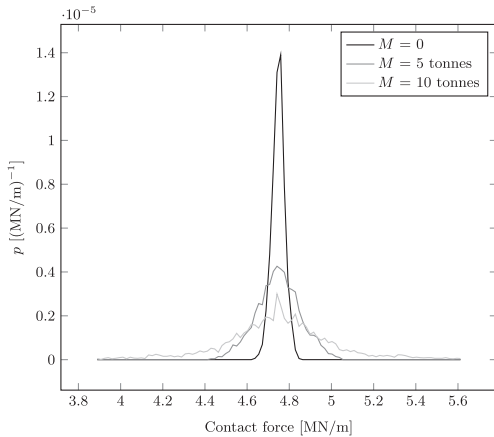


Fig. 10 Probability density graph of contact force magnitudes for varying magnitude of the added point mass, M

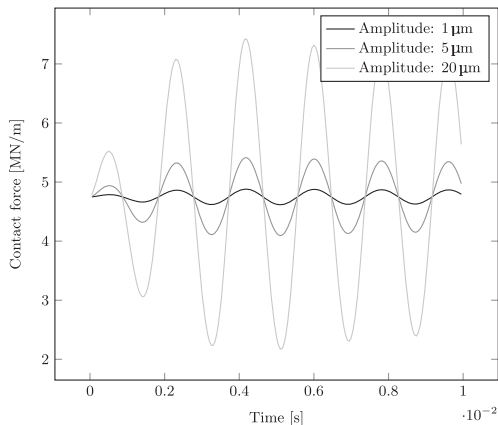


Fig. 11 Evolution in time of the contact force magnitude during negotiation of a plate with a sinusoidal corrugation pattern of varying amplitude

applied force magnitude. Figure 8 shows a narrowing of the probability density peak around the magnitude of the applied force for decreasing operational velocity, indicating a trend towards a quasi-static response. The predictive results can be compared to similar analyses in literature [9, 15].

In Fig. 11, the time evolution of the contact force magnitude is presented. The simulation features a plate profile with a sinusoidal corrugation pattern (type 1). An increased corrugation amplitude will increase the amplitude of the contact force. The relation between corrugation amplitude and steady state

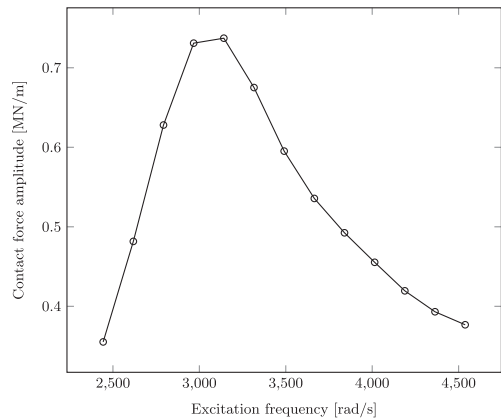


Fig. 12 Steady state contact force amplitude versus excitation frequency due to rolling with varying velocity on a plate with a sinusoidal corrugation pattern

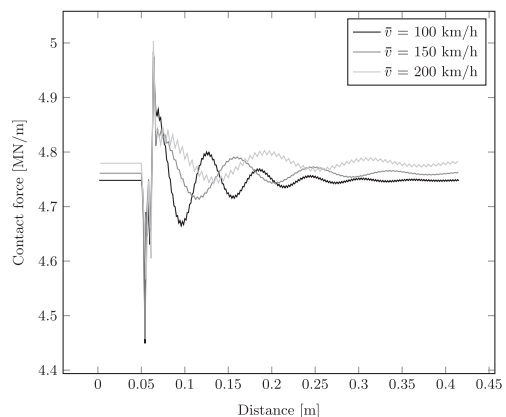


Fig. 13 Contact force evolution during negotiation of a sharp, 5 mm wide discontinuity of the plate for three different operational velocities

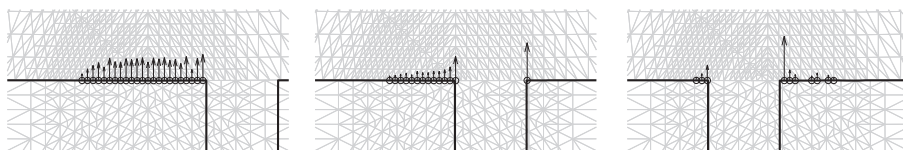


Fig. 14 Nodal contact force distribution when negotiating the plate discontinuity

contact force amplitude is linear for the parametric range studied. The influence of the operational velocity is non-linear, as seen in Fig. 12, where the steady state amplitude of the contact force is plotted versus the excitation frequency, calculated as \bar{v}/λ , where \bar{v} is the varied velocity and λ the fixed wavelength of the profile. The peak at $\bar{v}/\lambda \approx 3.05 \cdot 10^3$ rad/s corresponds to an eigenfrequency of the system corresponding to vertical oscillation of the cylinder on the plate. This conclusion was supported by an analytical consideration in which the contact was approximated as a (linearized) spring. This analysis predicted a natural frequency of $2.85 \cdot 10^3$ rad/s.

Figure 13 shows the time evolution of the vertical contact force magnitude while passing a sharp, 5 mm wide discontinuity (profile type 3). It is seen how the discontinuity pass triggers a contact force oscillation, the wavelength and amplitude of which will depend on the operational velocity. This response can be compared to similar analyses in literature [15].

In Fig. 14, the nodal contact force distribution (evaluated on the cylinder) at three instances in time when passing the discontinuity are presented. The operational velocity is $\bar{v} = 100$ km/h. The deformed cylinder and plate meshes are included, as is the plate profile (thick solid). Furthermore, cylinder nodes in contact are encircled and corresponding node contact forces plotted as arrows. It is seen how the reconnection of the two surfaces after the discontinuity involves high contact forces and local loss of contact within the contact patch.

To appreciate the computational efforts involved, it can be noted that all simulations were performed on a system with an Intel Core 2 Quad Q9400 (2.67 GHz) processor, 4 GB RAM, Windows 7 (64 bit), and MATLAB R2009b. The simulation (corresponding to $\bar{v} = 100$ km/h) presented in Fig. 8 featured 6000 time steps and 3282 elements. For this set-up, the wall clock time for the simulation was 50 min.

5 CONCLUDING REMARKS

A theoretical and numerical framework to evaluate rolling contact has been established based on an ALE formulation. A FE formulation featuring a

cylinder in contact with a plate has been implemented. The model features automated mesh refinement, non-reflecting boundary conditions, and the ability to incorporate arbitrary surface profiles. The presented examples show how the model can handle harsh contact conditions such as contact surface corrugation and discontinuities. Sensitivity and validation studies where the influence of numerical parameters are investigated are presented in this article and shows the model to be robust and trends in parametric responses to be reasonable compared to similar results in literature. Extreme analyses (not reported in this article) have shown the model to be capable of handling a complete lack of contact between the cylinder and the plate. Despite this versatility, the ALE formulation enables the model to be very compact and the computational demands very modest.

The results presented show the influence of surface roughness on the dynamical response of a cylinder–plate contact. The influence of an eigenmode where the cylinder is vibrating on the contacting plate while negotiating a corrugated plate was captured, as was the transient response when negotiating a severe discontinuity. The simulations further allowed the influence of operational parameters to be quantified. In an extension, the model will be extended to incorporate frictional contact and the related thermal loading.

FUNDING

The project is financed by the Swedish Research Council (www.vr.se) under contract 2008-3860 and is a part of the ongoing activities in the National Centre of Excellence CHARMEC (www.chalmers.se/charmec).

ACKNOWLEDGEMENT

The authors thank Peter Torstensson for providing rail roughness data.

© Authors 2011

REFERENCES

- 1 **Kalker, J. J.** *Three-dimensional elastic bodies in rolling contact*, 1990, p. 314 (Kluwer, Dordrecht).
- 2 **Johnson, K. L.** *Contact mechanics*, 1985, p. 452 (Cambridge University Press, Cambridge).
- 3 **Dang Van, K., Maitournam, M. H., and Prasil, B.** Elastoplastic analysis of repeated moving contact: application to railways damage phenomena. *Wear*, 1996, **196**, 77–81.
- 4 **Chang, C., Wang, C., Chen, B., and Li, L.** A study of a numerical analysis method for the wheel–rail wear of a heavy-haul train. *Proc. IMechE, Part F: J. Rail and Rapid Transit*, 2010, **224**, 473–482.
- 5 **Thompson, D. J.** Theoretical modelling of wheel–rail noise generation. *Proc. IMechE, Part F: J. Rail and Rapid Transit*, 1991, **205**, 137–149.
- 6 **Gullers, P., Andersson, L., and Lundén, R.** High-frequency vertical wheel–rail contact forces: field measurements and influence of track irregularities. *Wear*, 2008, **265**, 1472–1478.
- 7 **Nielsen, J. C. O.** High-frequency vertical wheel–rail contact forces validation of a prediction model by field testing. *Wear*, 2008, **265**, 1465–1471.
- 8 **Nielsen, J. C. O., Ekberg, A., and Lundén, R.** Influence of short-pitch wheel–rail corrugation on rolling contact fatigue of railway wheels. *Proc. IMechE, Part F: J. Rail and Rapid Transit*, 2005, **219**, 177–187.
- 9 **Ekberg, A., Kabo, E., Nielsen, J. C. O., and Lundén, R.** Subsurface initiated rolling contact fatigue of railway wheels as generated by rail corrugation. *Int. J. Solids Struct.*, 2007, **44**, 7975–7987.
- 10 **Donea, J. and Huerta, A.** *Finite element methods for flow problems*, 2003 (Wiley, New York).
- 11 **Wriggers, P.** *Computational contact mechanics*, edition 2, 2006 (Springer, Heidelberg).
- 12 **Krenk, S. and Kirkegaard, P. H.** Local tensor radiation conditions for elastic waves. *J. Sound Vib.*, 2001, **247**, 875–896.
- 13 **Rivara, M. C.** Algorithms for refining triangular grids suitable for adaptive and multigrid techniques. *Int. J. Numer. Methods Engng*, 1984, **20**, 745–756.
- 14 **Torstensson, P. T. and Nielsen, J. C. O.** Monitoring of rail corrugation growth due to irregular wear on a railway metro curve. *Wear*, 2009, **267**, 556–561.
- 15 **Kabo, E., Nielsen, J. C. O., and Ekberg, A.** Prediction of dynamic train–track interaction and subsequent material deterioration in the presence of insulated rail joints. *Veh. Sys. Dyn.*, 2006, **44**, 718–729.

APPENDIX

Notation

- a** acceleration related to standard configurations
- b** plate domain width
- B** external body force per unit volume in initial configuration

- \hat{B} external body force per unit volume in ALE reference configuration
- \underline{C} FE damping matrix
- \underline{d}_c analytically determined contact patch size
- E Young's modulus
- \hat{F} deformation gradient related to ALE configurations
- \bar{F}_{Cy} normalized contact force amplitude
- \mathbf{g} known displacements related to standard configurations
- $\hat{\mathbf{g}}$ known displacements related to ALE configurations
- \hat{G} deformation Hessian related to ALE configurations
- h plate domain height
- \underline{K} FE stiffness matrix
- \underline{M} FE mass matrix
- n number of realizations (time increments) within a given interval (probability density)
- n_{nx} number of nodes in plate in horizontal direction
- n_r number of global refinements of cylinder mesh
- N number of time steps
- N outward normal related to initial configuration
- \hat{N} outward normal related to ALE reference configuration
- p probability density
- P applied force magnitude
- \mathbf{P} first Piola–Kirchhoff stress tensor
- $\hat{\mathbf{P}}$ first Piola–Kirchhoff stress tensor related to ALE reference configuration
- r_i cylinder inner radius
- r_o cylinder outer radius
- T external traction per unit area in initial configuration
- \hat{T} external traction per unit area in ALE reference configuration
- \mathbf{u} deformation related to standard configurations
- $\hat{\mathbf{u}}$ deformation related to ALE configurations
- \bar{v} cylinder velocity
- \bar{v} convective velocity
- \mathbf{x} coordinate in deformed configuration
- $\hat{\mathbf{x}}$ coordinate in ALE deformed configuration
- \underline{X} coordinate in undeformed configuration
- $\hat{\underline{X}}$ coordinate in ALE reference configuration
- \underline{X} translation of the cylinder center
- α_0 mass-proportional Rayleigh damping coefficient
- α_1 stiffness-proportional Rayleigh damping coefficient

ΔP	force interval length for probability density	$\hat{\phi}$	placement map from $\Omega_{\hat{x}}$ to $\omega_{\hat{x}}$
Δt	time step size	ω_x	current configuration
λ	wavelength of plate profile	$\omega_{\hat{x}}$	ALE deformed configuration
ν	Poisson's ratio	Ω_X	initial configuration
ρ_X	density in initial configuration	$\Omega_{\hat{x}}$	ALE reference configuration
$\rho_{\hat{x}}$	density in ALE reference configuration	∇_X	gradient related to initial configuration
ϕ	placement map from Ω_X to $\Omega_{\hat{x}}$	$\hat{\nabla}$	gradient related to ALE reference configuration
ϕ	placement map from $\omega_{\hat{x}}$ to ω_x		
φ	placement map from Ω_X to ω_x		

Paper B

Finite element analysis of transient thermomechanical rolling contact using an efficient arbitrary Lagrangian–Eulerian description

Finite element analysis of transient thermomechanical rolling contact using an efficient arbitrary Lagrangian–Eulerian description

Andreas Draganis · Fredrik Larsson · Anders Ekberg

Received: 20 April 2012 / Accepted: 30 January 2014 / Published online: 27 February 2014
© The Author(s) 2014. This article is published with open access at Springerlink.com

Abstract A theoretical and computational framework for the analysis of thermomechanically coupled transient rolling contact, based on an arbitrary Lagrangian–Eulerian (ALE) kinematical description, is developed. A finite element formulation featuring 2D cylinder–plate rolling contact is implemented. The implementation features penalty-type contact formulations for mechanical and thermal contact. It is noted that the ALE formulation allows for a simplified time description, a compact computational domain and localized mesh refinement. Numerical simulations considering stationary and transient rolling conditions are presented. Highlighted aspects include the influence of variations in thermal contact conductivity, rolling speed and external mechanical load on the contact interface heat flow. The model is shown to give predictions in qualitative agreement with results in the literature. For the velocity range studied, numerical issues such as spurious numerical dissipation/oscillations in the temperature field are noted to have a prominent influence. These phenomena are addressed using a Streamline-Upwind Petrov–Galerkin stabilization scheme together with a bubble function approach.

Keywords Thermomechanical analysis · Arbitrary Lagrangian–Eulerian · Rolling contact · Transient analysis · Finite element method

1 Introduction

Thermomechanical analysis of bodies in rolling contact is of significant engineering and theoretical interest. Thermal

expansion, dissipative heat generation and frictional heat generation [1] are all modes of thermomechanical coupling which may significantly influence the mechanical and thermal behaviour of the contacting bodies, as well as their material properties. Examples of applications where a thermomechanical analysis might be crucial for an accurate description of the response include rolling mills, roller bearings and wheel–rail contacts [2]. It should here be noted that the flow of heat through the contact interface (in railway applications denoted “rail chill”), as well as the partitioning of the frictional heat generated at the contact interface, depend strongly on the rolling velocity [3,4]. This point will be further discussed in subsequent sections.

A common approach to numerical modelling of rolling contact is to employ a semi-analytical contact model based on Hertz theory [5–7]. Such an implementation is simple and fast, but limited by assumptions of elastic material response, smooth, continuous surfaces and a small relative dimension of the contact patch. In contrast, a contact formulation involving deformation dependent contact forces and an iterative contact search algorithm [7,8] adds a significant (often much-needed) versatility. However, this approach is relatively complicated to implement and increases computational demands.

In finite element modelling of solid mechanics problems, a Lagrangian kinematical description is usually employed. When modelling rolling contact in particular, a problem formulation based instead on an arbitrary Lagrangian–Eulerian (ALE) description provides important advantages [8,9]. These (elaborated in following sections) include the possibility to linearize the mechanical response, the compactness of the computational domain, the simplified time description, the possibility for highly localized mesh refinement and the elimination of the need for velocity-dependent contact conductivity modelling.

A. Draganis (✉) · F. Larsson · A. Ekberg
Department of Applied Mechanics, Chalmers University
of Technology, 412 96 Göteborg, Sweden
e-mail: andreas.draganis@chalmers.se

The mathematical foundations of mechanical rolling contact in the context of an ALE description were first presented in Nackenhorst [9]. Here, the relevant kinematical description, balance laws, weak forms and contact kinematics are discussed in elaborate detail. The paper highlights the advantages of the ALE approach, but also discusses complications stemming from the intrinsic difficulty of tracing material points in this case. These include the difficulty of handling inelastic material behaviour as well as keeping track of relative slip distances. Both of these issues were addressed in Ziefle and Nackenhorst [10], where a staggered solution scheme is suggested, i.e. involving solution of the advection equation to keep track of internal variable data. In a recent paper [11], the use of an ALE method for thermomechanically coupled stationary rolling contact is introduced. Here, a thermoviscoelastic constitutive model is employed, involving large deformations and temperature-dependent constitutive parameters.

The present paper aims to provide a comprehensive presentation of thermomechanically coupled transient rolling contact in the context of an ALE description. Specific attention is here given to the stress, the deformation-induced heat source, the heat flux and the mechanical and thermal boundary conditions as they appear in the ALE framework. Furthermore, issues of numerical inaccuracy related to the solution of the discretized energy balance equation are discussed in detail, and stabilization measures are suggested.

The paper is outlined as follows: In Sect. 2, the kinematical description of the rolling cylinder on the plate is presented. The thermomechanical boundary value problem, including its finite element formulation, is defined in Sect. 3. Section 4 contains a discussion about element choice and numerical stabilization measures necessary for an accurate numerical response. In Sect. 5, the mechanical and thermal contact formulations are described. Numerical examples are presented in Sect. 6. In particular, the model is validated and the influence of key operational parameters is evaluated. With Sect. 7, the paper is concluded with a summary and an outlook towards future work.

2 ALE description of rolling contact

The employed ALE description of cylinder–plate rolling motion [12] can be described as follows: Two intermediate configurations are utilized in addition to the initial (“undeformed”) configuration, $\Omega \ni X$, and the current (“deformed”) configuration, $\omega \ni x$. The first intermediate configuration is denoted $\hat{\Omega} \ni \hat{X}$. The map from Ω to $\hat{\Omega}$ accounts for a rigid body rotation of the cylinder and a pure translation of the plate. The second intermediate configuration is denoted $\check{\omega} \ni \check{x}$. The map from $\hat{\Omega}$ to $\check{\omega}$ accounts for the deformation of cylinder and plate. Both intermediate configurations

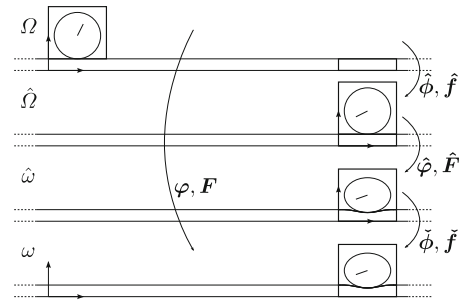


Fig. 1 Illustration of configurations and maps relevant to the employed ALE description

feature a moving coordinate system that follows the cylinder centre. The map from $\hat{\omega}$ to ω accounts for a pure translation of the system in going back to the original fixed coordinate system.

The maps between the configurations are formulated as $\hat{X} = \hat{\phi}(X, t)$, $\check{x} = \check{\phi}(\hat{X}, t)$, $x = \check{\phi}(\check{x}, t)$ and $x = \varphi(X, t)$, so that $\varphi(X, t) = \check{\phi}(\hat{\phi}(X, t), t)$. The corresponding deformation gradients are, in respective order: \hat{f} , \hat{F} , \check{f} and F . Figure 1 shows a schematic illustration of the employed configurations, with their intermediary maps and deformation gradients.

The rigid body maps $\hat{X} = \hat{\phi}(X, t)$ and $x = \check{\phi}(\check{x}, t)$ can be expressed a priori from knowledge of the translational and rotational motion of the cylinder along the plate:

$$\hat{X} = \hat{\phi}(X, t) = \begin{cases} R(t) \cdot (X - X_0) + X_0 & \text{for } X \in \Omega^c \\ X - \bar{X}(t) & \text{for } X \in \Omega^p \end{cases}, \quad (1)$$

$$x = \check{\phi}(\check{x}, t) = \check{x} + \bar{X}(t) \quad \text{for } \check{x} \in \hat{\omega}, \quad (2)$$

where R is a rotation tensor, X_0 is the position of the cylinder centre in the undeformed configuration, \bar{X} is the translation of the cylinder centre and Ω^c and Ω^p are the subsets of Ω representing the cylinder and plate domains, respectively. Note that $\hat{f} = R$ and $\hat{f} = I$ in the domain of the cylinder and plate, respectively, and that $\check{f} = I$. The Lagrangian problem of finding the map $x = \varphi(X, t)$ (or the displacement $u(X, t) = \varphi(X, t) - X$) is thus narrowed down to the ALE problem of finding the map $\check{x} = \check{\phi}(\hat{X}, t)$ (or the displacement $\hat{u}(\hat{X}, t) = \check{\phi}(\hat{X}, t) - \hat{X}$). For small strains, the ALE displacements \hat{u} will be small, which is generally not the case for the standard Lagrangian displacements u . Consequently, in the former case (but not the latter) it is possible to linearize the mechanical response. In particular, it is noted that the total deformation gradient can be expressed as

$$F = \check{f} \cdot \hat{F} \cdot \hat{f} = \hat{F} \cdot \hat{f}, \quad (3)$$

since $\hat{f} = I$. The linearization of the material behaviour pertains to the assumption that $\hat{F} \approx I$ while \hat{f} is arbitrary. This point is elaborated in Sect. 3.

Another advantage of the presented convective kinematical description is the fact that it allows for a compact computational model: only a relatively short section of the plate domain needs to be modelled, regardless of rolling distance. Further, the position (in the intermediate domains) of the contact region in both cylinder and plate is largely stationary throughout the rolling motion, allowing for localized mesh refinement. Figure 10 in Sect. 6 illustrates these points.

A potential difficulty in convective formulations is the tracking of boundaries. In the present case, since a round cylinder and a flat plate are considered, the boundaries are stationary and this is not a problem. However, numerical problems due to convective effects will require attention (see Sect. 4).

3 Thermomechanical problem

In the following, the strong and weak forms as well as the finite element formulation of the thermomechanically coupled problem are derived in terms of the ALE description. Isotropic, homogeneous and thermoelastic materials are initially assumed. Plane strain and linear elasticity are later assumed in the derivation of the FE formulation.

3.1 Strong form

The local balance of momentum equation with respect to a volume element in the initial configuration Ω is

$$\rho a - P \cdot \nabla_X - B = 0 \text{ in } \Omega, \tag{4}$$

where $P = P(F, \theta)$ is the first Piola–Kirchhoff stress tensor, ρ is the density in the initial configuration, B is the external body force per unit volume (in the initial configuration) and a is the acceleration: $a = D_{tt}x = D_{tt}u$, where $D_t(\cdot) := \partial(\cdot)/\partial t|_X^1$, $D_{tt}(\cdot) := \partial^2(\cdot)/\partial t^2|_X$. ∇_X is the vector differential operator with respect to Ω . Boundary conditions are imposed as ($\Gamma := \partial\Omega$)

$$\begin{cases} T = T_P & \text{on } \Gamma_{N_u}, \\ u = u_P & \text{on } \Gamma_{D_u}, \end{cases} \tag{5}$$

where $T := P \cdot N$ (N is the outward normal), T_P is the prescribed external traction per unit area with respect to Ω and u_P represents prescribed displacements.

¹ X held fixed.

In terms of the ALE description, the momentum balance equation takes the form² [12]

$$\begin{aligned} \hat{\rho} \left[\ddot{\hat{X}} + d_{tt}\hat{u} + 2 \left[(d_t\hat{u}) \otimes \hat{\nabla} \right] \cdot \bar{v} + \hat{F} \cdot (D_t\bar{v}) \right. \\ \left. + \hat{G} : (\bar{v} \otimes \bar{v}) \right] - \hat{P} \cdot \hat{\nabla} - \hat{B} = 0 \text{ in } \hat{\Omega}, \end{aligned} \tag{6}$$

where $d_t(\cdot) := \partial(\cdot)/\partial t|_{\hat{X}}$, $d_{tt}(\cdot) := \partial^2(\cdot)/\partial t^2|_{\hat{X}}$ are referential time derivatives, $\hat{F} := \hat{x} \otimes \hat{\nabla}$, $\hat{G} := \hat{x} \otimes \hat{\nabla} \otimes \hat{\nabla}$, and

$$\bar{v} = D_t\hat{X} = \begin{cases} \hat{R} \cdot R^T \cdot (\hat{X} - X_0) & \text{for } \hat{X} \in \hat{\Omega}^c \\ -\hat{X} & \text{for } \hat{X} \in \hat{\Omega}^p \end{cases} \tag{7}$$

is the convective velocity pertinent to the map $\hat{\phi}$ (see Eq. (1)). Note that due to the nature of the rotation tensor, $\hat{\nabla} \cdot \bar{v} = 0$. $\hat{(\cdot)}$ denotes quantities related to $\hat{\Omega}$. In particular, $\hat{P} = P \cdot \hat{f}^T$ is the push-forward of the first Piola–Kirchhoff stress tensor to $\hat{\Omega}$.

For a thermoelastic material, the constitutive relation $P(F, \theta)$ for the first Piola–Kirchhoff stress can be defined from a free energy function $\Psi(F, \theta)$ such that $P(F, \theta) = \partial\Psi(F, \theta)/\partial F$. For an isotropic material, Ψ should be independent of any rotation prior to the deformation, i.e.

$$\Psi(F \cdot R, \theta) = \Psi(F, \theta), \tag{8}$$

for an arbitrary deformation gradient F , temperature θ and rotation tensor R . Consequently, the derivatives of Ψ with respect to F (i.e. the stress) must satisfy the conditions

$$\begin{aligned} \frac{\partial\Psi(\tilde{F} \cdot R, \theta)}{\partial\tilde{F}} &= \frac{\partial\Psi(\tilde{F}, \theta)}{\partial\tilde{F}} \Rightarrow P(\tilde{F} \cdot R, \theta) \cdot R^T \\ &= P(\tilde{F}, \theta) \end{aligned} \tag{9}$$

for any \tilde{F} and any R . As a consequence,

$$P(\hat{F} \cdot \hat{f}, \theta) \cdot \hat{f}^T = P(\hat{F}, \theta) \tag{10}$$

for any \hat{f} being either a rotation (as in the cylinder) or the identity (as in the plate). Hence, the original constitutive model can be used and $\hat{P} (= \hat{P}(\hat{F}, \theta) = P(F, \theta) \cdot \hat{f}^T = P(\hat{F} \cdot \hat{f}, \theta) \cdot \hat{f}^T = P(\hat{F}, \theta))$ can be expressed independently of \hat{f} . For small deformation/temperature thermoelasticity ($F \approx I$ and $\theta \approx \theta^{ref}$) it is commonly adopted that $P \approx E : [H - \alpha\bar{\theta}I]$, where $H = F - I$, E is the elasticity tensor, α is the thermal expansion coefficient and $\bar{\theta} = \theta - \theta^{ref}$ is the excess temperature with respect to the reference θ^{ref} . Therefore, the linearization of \hat{P} for small strains ($\hat{F} \approx I$) and small temperature fluctuations ($\theta \approx \theta^{ref}$), becomes

$$\hat{P} = E : [\hat{H} - \alpha\bar{\theta}I] = E : \hat{H} - 3K\alpha\bar{\theta}I, \tag{11}$$

² \otimes denotes the dyadic product.

where $\hat{\mathbf{H}} = \hat{\mathbf{F}} - \mathbf{I}$ and K is the bulk modulus. Hence, for an unconstrained specimen ($\hat{\mathbf{P}} = 0$), the temperature driven deformation is $\hat{\mathbf{F}} = (1 + \alpha\bar{\theta})\mathbf{I}$.

Remark 1 In the cylinder domain, it is only the relation $\hat{\mathbf{P}}(\hat{\mathbf{F}})$ —and not $\mathbf{P}(\mathbf{F})$ — that can be linearized, since \mathbf{F} will here contain a finite rotation (see Eqs. (3) and (1)).

The boundary conditions can in the ALE framework be phrased as

$$\begin{cases} \hat{\mathbf{T}}^{\text{TOT}} + \hat{\rho}(\hat{\mathbf{H}} \cdot \bar{\mathbf{v}})(\bar{\mathbf{v}} \cdot \hat{\mathbf{N}}) = \hat{\mathbf{T}}_P & \text{on } \hat{\Gamma}_{R_u} \\ \hat{\mathbf{u}} = \hat{\mathbf{u}}_P & \text{on } \hat{\Gamma}_{D_u}, \end{cases} \tag{12}$$

where $\hat{\mathbf{T}}^{\text{TOT}}$ in the Robin-type boundary condition (12a) is the natural boundary traction obtained via integration by parts in the weak form (see Sect. 3.2).

The strong form of the energy balance equation with respect to the initial configuration Ω is [13,14]

$$\begin{aligned} (\theta^{\text{ref}} + \bar{\theta})\beta : (D_t \mathbf{F}) + \rho c D_t \bar{\theta} \\ + \mathbf{q} \cdot \nabla_X - r = 0 \text{ in } \Omega, \end{aligned} \tag{13}$$

where

$$\beta = - \frac{\partial^2 \Psi}{\partial \theta \partial \mathbf{F}} = - \frac{\partial \mathbf{P}}{\partial \theta}, \tag{14}$$

is the deformation-induced heat source, c is the mass specific heat capacity, \mathbf{q} is the heat flux and r is the external heat power per unit volume (in the initial configuration). Boundary conditions are imposed as

$$\begin{cases} q_N = q_{N,P} & \text{on } \Gamma_{N_\theta} \\ \bar{\theta} = \bar{\theta}_P & \text{on } \Gamma_{D_\theta}, \end{cases} \tag{15}$$

where $q_N := \mathbf{q} \cdot \mathbf{N}$. In terms of the ALE description, the energy balance equation takes the form

$$\begin{aligned} (\theta^{\text{ref}} + \bar{\theta})\hat{\beta} : [d_t \hat{\mathbf{H}} + (\hat{\mathbf{F}} \cdot \bar{\mathbf{v}}) \otimes \hat{\mathbf{V}}] \\ + \hat{\rho}c \left(\hat{\mathbf{V}}\bar{\theta} \cdot \bar{\mathbf{v}} + d_t \bar{\theta} \right) + \hat{\mathbf{q}} \cdot \hat{\mathbf{V}} - \hat{r} = 0 \text{ in } \hat{\Omega}, \end{aligned} \tag{16}$$

where $\hat{(\cdot)}$ denotes quantities related to $\hat{\Omega}$. In particular, $\hat{\beta} = \beta \cdot \hat{\mathbf{f}}^T$ and $\hat{\mathbf{q}} = \hat{\mathbf{f}} \cdot \mathbf{q}$ were introduced. Furthermore, for isotropic materials,

$$\begin{aligned} \hat{\beta} = \beta(\mathbf{F}, \theta) \cdot \hat{\mathbf{f}}^T &= - \frac{\partial [\mathbf{P}(\mathbf{F}, \theta) \cdot \hat{\mathbf{f}}^T]}{\partial \theta} \\ &= - \frac{\partial \mathbf{P}(\hat{\mathbf{F}}, \theta)}{\partial \theta} = \beta(\hat{\mathbf{F}}, \theta), \end{aligned} \tag{17}$$

where Eq. (10) was used and a known constitutive relation $\beta(\mathbf{F}, \theta)$ in the initial configuration was assumed. Hence,

$$\hat{\beta} = - \frac{\partial \mathbf{P}(\hat{\mathbf{F}}, \theta)}{\partial \theta} = - \frac{\partial \hat{\mathbf{P}}}{\partial \theta} = 3K\alpha\mathbf{I}, \tag{18}$$

where the last equality is valid for the linearized case (see Eq. (11)).

Furthermore, in analogy with the result for the first Piola–Kirchhoff stress, it can be shown that for an isotropic material (and for $\hat{\mathbf{f}}$ being a rotation or the identity tensor),

$$\hat{\mathbf{q}} = \mathbf{q}(\nabla_X \bar{\theta}) \cdot \hat{\mathbf{f}}^T = \mathbf{q}(\hat{\mathbf{V}}\bar{\theta} \cdot \hat{\mathbf{f}}) \cdot \hat{\mathbf{f}}^T = \mathbf{q}(\hat{\mathbf{V}}\bar{\theta}), \tag{19}$$

where it was tacitly assumed that the heat flux only depends on the gradient of the temperature with respect to the initial configuration. In particular, the linear Fourier’s law is henceforth adopted, whereby it is obtained that

$$\hat{\mathbf{q}} = -k \hat{\mathbf{V}}\bar{\theta}, \tag{20}$$

where k is the constant heat conductivity.

The boundary conditions can in the ALE framework be phrased as

$$\begin{cases} \hat{q}_N^{\text{TOT}} - \hat{\rho}c\bar{\theta}(\bar{\mathbf{v}} \cdot \hat{\mathbf{N}}) = \hat{q}_{N,P} & \text{on } \hat{\Gamma}_{R_\theta} \\ \bar{\theta} = \bar{\theta}_P & \text{on } \hat{\Gamma}_{D_\theta}, \end{cases} \tag{21}$$

where \hat{q}_N^{TOT} in the Robin-type boundary condition (21a) is the natural boundary flux obtained via integration by parts in the weak form (see Sect. 3.2).

Linearizing the energy balance Eq. (16) for small strains and small temperature fluctuations gives

$$\begin{aligned} \theta^{\text{ref}}\hat{\beta} : (d_t \hat{\mathbf{H}} + (\hat{\mathbf{H}} \cdot \bar{\mathbf{v}}) \otimes \hat{\mathbf{V}}) + (\theta^{\text{ref}} + \bar{\theta})\hat{\beta} : [\bar{\mathbf{v}} \otimes \hat{\mathbf{V}}] \\ + \hat{\rho}c \left(\hat{\mathbf{V}}\bar{\theta} \cdot \bar{\mathbf{v}} + d_t \bar{\theta} \right) + \hat{\mathbf{q}} \cdot \hat{\mathbf{V}} - \hat{r} = 0 \text{ in } \hat{\Omega}. \end{aligned} \tag{22}$$

For isotropic materials, (18) is valid, and we obtain

$$\begin{aligned} 3K\alpha\theta^{\text{ref}}(\mathbf{I} : d_t \hat{\mathbf{H}} + (\hat{\mathbf{H}} \cdot \bar{\mathbf{v}}) \cdot \hat{\mathbf{V}}) \\ + \hat{\rho}c \left(\hat{\mathbf{V}}\bar{\theta} \cdot \bar{\mathbf{v}} + d_t \bar{\theta} \right) + \hat{\mathbf{q}} \cdot \hat{\mathbf{V}} - \hat{r} = 0 \text{ in } \hat{\Omega}, \end{aligned} \tag{23}$$

where it was used that $\bar{\mathbf{v}}$ is divergence free (see Eq. (7)).

In summary: For homogeneous, isotropic materials, the residuals of the linearized strong form of the transient thermomechanically coupled problem are

$$\begin{aligned} \mathbf{R}_u^s(\hat{\mathbf{u}}, \bar{\theta}) &= \hat{\rho} \left[\ddot{\mathbf{X}} + d_t \hat{\mathbf{u}} + 2 \left[(d_t \hat{\mathbf{u}}) \otimes \hat{\mathbf{V}} \right] \cdot \bar{\mathbf{v}} \right. \\ &\quad \left. + \hat{\mathbf{F}} \cdot (D_t \bar{\mathbf{v}}) + \hat{\mathbf{G}} : (\bar{\mathbf{v}} \otimes \bar{\mathbf{v}}) \right] - \hat{\mathbf{P}} \cdot \hat{\mathbf{V}} - \hat{\mathbf{B}} = 0, \\ \mathbf{R}_\theta^s(\hat{\mathbf{u}}, \bar{\theta}) &= 3K\alpha\theta^{\text{ref}}(\mathbf{I} : d_t \hat{\mathbf{H}} + (\hat{\mathbf{H}} \cdot \bar{\mathbf{v}}) \cdot \hat{\mathbf{V}}) \\ &\quad + \hat{\rho}c \left(\hat{\mathbf{V}}\bar{\theta} \cdot \bar{\mathbf{v}} + d_t \bar{\theta} \right) + \hat{\mathbf{q}} \cdot \hat{\mathbf{V}} - \hat{r} = 0, \end{aligned} \tag{24}$$

where the linearized form of $\hat{\mathbf{P}}$ is given in (11). It is clear from (11) that $\hat{\mathbf{P}}$ is temperature dependent, due to the influence of thermal expansion. This constitutes the influence of the temperature field on the momentum balance equation. Furthermore, the deformation-dependent terms in the second equation above represents the Gough–Joule effect: reversible heating/cooling of the material resulting from a nonzero strain rate [15]. In the ALE context, this term is split into a referential derivative and a convective term (as seen above). In a stationary analysis, the former vanishes. It should be noted that the Gough–Joule effect is negligible for thermoelastic materials [13]. Consequently, the thermomechanical coupling is one-sided in this case.

It can be seen that when the translational and rotational velocity of the system is constant in time, $\bar{\mathbf{v}}$ and $\bar{\mathbf{X}}$ are constant in time (specifically, $\ddot{\mathbf{X}} = 0$) and the time dependence in the above equations is confined to the solution fields (and the external loads).

If stationary rolling conditions are assumed, all referential time derivatives (d_t, d_{tt}) as well as $\ddot{\mathbf{X}}$ are zero, resulting in a time-independent problem involving the residuals

$$\begin{aligned} \mathbf{R}_u^s(\hat{\mathbf{u}}, \bar{\theta}) &= \hat{\rho} \left[\hat{\mathbf{P}} \cdot (D_t \bar{\mathbf{v}}) + \hat{\mathbf{G}} : (\bar{\mathbf{v}} \otimes \bar{\mathbf{v}}) \right] \\ &\quad - \hat{\mathbf{P}} \cdot \hat{\mathbf{V}} - \hat{\mathbf{B}}, \\ R_\theta^s(\hat{\mathbf{u}}, \bar{\theta}) &= 3K\alpha\theta^{\text{ref}} (\hat{\mathbf{H}} \cdot \bar{\mathbf{v}}) \cdot \hat{\mathbf{V}} + \hat{\rho} c \hat{\mathbf{V}} \bar{\theta} \cdot \bar{\mathbf{v}} \\ &\quad + \hat{\mathbf{q}} \cdot \hat{\mathbf{V}} - \hat{r}. \end{aligned} \tag{25}$$

3.2 Weak form

The weak form is obtained by weighting the local expressions in Eq. (24) with arbitrary (time-independent) test functions $(\delta \hat{\mathbf{u}}, \delta \bar{\theta}) \in \mathbf{V}_u^0 \times \mathcal{V}_\theta^0$, integrating over the whole domain $\hat{\Omega}$ and performing integration by parts. The weak residuals are thus defined as

$$\begin{aligned} &\int_{\hat{\Omega}} \delta \hat{\mathbf{u}} \cdot \mathbf{R}_u^s(\hat{\mathbf{u}}, \bar{\theta}) dV \\ &= \hat{\rho} \int_{\hat{\Omega}} \delta \hat{\mathbf{u}} \cdot d_{tt} \hat{\mathbf{u}} dV \\ &\quad + 2\hat{\rho} \int_{\hat{\Omega}} \delta \hat{\mathbf{u}} \cdot \left[(d_t \hat{\mathbf{u}}) \otimes \hat{\mathbf{V}} \right] \cdot \bar{\mathbf{v}} dV \\ &\quad + \int_{\hat{\Omega}} (\delta \hat{\mathbf{u}} \otimes \hat{\mathbf{V}}) : \hat{\mathbf{P}}^{\text{TOT}} dV + \int_{\hat{\Omega}} \delta \hat{\mathbf{u}} \cdot \hat{r} dV \\ &\quad - \int_{\hat{\Omega}} \delta \hat{\mathbf{u}} \cdot \hat{\mathbf{B}}^{\text{TOT}} dV - \int_{\hat{\Gamma}_{N_u}} \delta \hat{\mathbf{u}} \cdot \hat{\mathbf{T}}^{\text{TOT}} dA, \end{aligned} \tag{26}$$

where

$$\begin{aligned} \hat{\mathbf{P}}^{\text{TOT}} &:= \mathbf{E} : \hat{\mathbf{H}} - \hat{\rho} \hat{\mathbf{H}} \cdot (\bar{\mathbf{v}} \otimes \bar{\mathbf{v}}) - 3K\alpha\bar{\theta} \mathbf{I}, \\ \hat{r} &:= \hat{\rho} \hat{\mathbf{H}} \cdot (D_t \bar{\mathbf{v}} - (\bar{\mathbf{v}} \otimes \bar{\mathbf{v}}) \cdot \hat{\mathbf{V}}), \\ \hat{\mathbf{B}}^{\text{TOT}} &:= \hat{\mathbf{B}} - \hat{\rho} D_t \bar{\mathbf{v}} - \hat{\rho} \ddot{\mathbf{X}}, \end{aligned}$$

$$\begin{aligned} \hat{\mathbf{T}}^{\text{TOT}} &:= \hat{\mathbf{T}} - \hat{\rho} (\hat{\mathbf{H}} \cdot \bar{\mathbf{v}}) (\bar{\mathbf{v}} \cdot \hat{\mathbf{N}}), \\ &\int_{\hat{\Omega}} \delta \bar{\theta} \mathbf{R}_\theta^s(\hat{\mathbf{u}}, \bar{\theta}) dV \\ &= 3K\alpha\theta^{\text{ref}} \int_{\hat{\Omega}} \delta \bar{\theta} \mathbf{I} : d_t \hat{\mathbf{H}} dV \\ &\quad + 3K\alpha\theta^{\text{ref}} \int_{\hat{\Gamma}} \delta \bar{\theta} (\hat{\mathbf{H}} \cdot \bar{\mathbf{v}}) \cdot \hat{\mathbf{N}} dA \\ &\quad - 3K\alpha\theta^{\text{ref}} \int_{\hat{\Omega}} (\hat{\mathbf{V}} \delta \bar{\theta}) \cdot (\hat{\mathbf{H}} \cdot \bar{\mathbf{v}}) dV \\ &\quad + \int_{\hat{\Omega}} (\hat{\mathbf{V}} \delta \bar{\theta}) \cdot [k \hat{\mathbf{V}} \bar{\theta} - \hat{\rho} c \bar{\mathbf{v}} \bar{\theta}] dV \\ &\quad + \hat{\rho} c \int_{\hat{\Omega}} \delta \bar{\theta} d_t \bar{\theta} dV - \int_{\hat{\Omega}} \delta \bar{\theta} \hat{r} dV \\ &\quad + \int_{\hat{\Gamma}_{N_\theta}} \delta \bar{\theta} \hat{\mathbf{q}}_N^{\text{TOT}} dA, \end{aligned} \tag{27}$$

where

$$\hat{\mathbf{q}}_N^{\text{TOT}} := \hat{\mathbf{q}}_N + \hat{\rho} c \bar{\theta} (\bar{\mathbf{v}} \cdot \hat{\mathbf{N}}),$$

and it was used that

$$\hat{\mathbf{q}} = -k \hat{\mathbf{V}} \bar{\theta}.$$

Remark 2 As shown in Nackenhorst [9], it is possible to obtain a higher degree of symmetry in the weak form (26) by partial integration of the second term on the right-hand side:

$$\begin{aligned} &\hat{\rho} \int_{\hat{\Omega}} \delta \hat{\mathbf{u}} \cdot \left[(d_t \hat{\mathbf{u}}) \otimes \hat{\mathbf{V}} \right] \cdot \bar{\mathbf{v}} dV \\ &\quad + \hat{\rho} \int_{\hat{\Omega}} \delta \hat{\mathbf{u}} \cdot \left[(d_t \hat{\mathbf{u}}) \otimes \hat{\mathbf{V}} \right] \cdot \bar{\mathbf{v}} dV \\ &= \hat{\rho} \int_{\hat{\Omega}} \delta \hat{\mathbf{u}} \cdot \left[(d_t \hat{\mathbf{u}}) \otimes \hat{\mathbf{V}} \right] \cdot \bar{\mathbf{v}} dV \\ &\quad - \hat{\rho} \int_{\hat{\Omega}} (\delta \hat{\mathbf{u}} \otimes \hat{\mathbf{V}}) : ((d_t \hat{\mathbf{u}}) \otimes \bar{\mathbf{v}}) dV \\ &\quad + \hat{\rho} \int_{\hat{\Gamma}} \delta \hat{\mathbf{u}} \cdot (d_t \hat{\mathbf{u}}) \bar{\mathbf{v}} \cdot \hat{\mathbf{N}} dA, \end{aligned}$$

where the divergence theorem and the fact that $\bar{\mathbf{v}}$ is divergence free were used. It is noted that the first two terms on the right-hand side constitute an antisymmetric contribution to the weak form.

The term $\hat{\mathbf{T}}^{\text{TOT}}$ emerges from the ALE formulation of the momentum balance equation. Thus, prescribing $\hat{\mathbf{T}}^{\text{TOT}}$ on $\hat{\Gamma}_{N_u}$ constitutes a natural (Neumann) boundary condition:

$$\hat{\mathbf{T}}_P^{\text{TOT}} = \hat{\mathbf{T}} - \hat{\rho} (\hat{\mathbf{H}} \cdot \bar{\mathbf{v}}) (\bar{\mathbf{v}} \cdot \hat{\mathbf{N}}) \text{ on } \hat{\Gamma}_{N_u}.$$

If instead the intrinsic (physical) traction $\hat{\mathbf{T}} := \hat{\mathbf{P}} \cdot \hat{\mathbf{N}}$ is prescribed, a Robin-type boundary condition is obtained:

$$\hat{\mathbf{T}}^{\text{TOT}} + \hat{\rho} (\hat{\mathbf{H}} \cdot \bar{\mathbf{v}}) (\bar{\mathbf{v}} \cdot \hat{\mathbf{N}}) = \hat{\mathbf{T}}_P \text{ on } \hat{\Gamma}_{R_u},$$

where the boundary $\hat{\Gamma}_{N_u}$ was simply renamed $\hat{\Gamma}_{R_u}$ in order to reflect the type of boundary condition in effect. Similarly, prescribing the quantity $\hat{q}_{\hat{N}_\theta}^{\text{TOT}}$ on $\hat{\Gamma}_{N_\theta}$ constitutes a natural (Neumann) boundary condition:

$$\hat{q}_{\hat{N}_P}^{\text{TOT}} = \hat{\rho}c\bar{\theta}(\bar{\mathbf{v}} \cdot \hat{\mathbf{N}}) + \hat{q}_{\hat{N}} \text{ on } \hat{\Gamma}_{N_\theta}.$$

If instead the intrinsic (physical) heat flux \hat{q} is prescribed, a Robin-type boundary condition is obtained:

$$\hat{q}_{\hat{N}}^{\text{TOT}} - \hat{\rho}c\bar{\theta}(\bar{\mathbf{v}} \cdot \hat{\mathbf{N}}) = \hat{q}_{\hat{N},P} \text{ on } \hat{\Gamma}_{R_\theta},$$

where the boundary $\hat{\Gamma}_{N_\theta}$ was renamed $\hat{\Gamma}_{R_\theta}$.

In order to state the final version of the weak form, trial and test spaces are introduced for the respective solution fields $\hat{\mathbf{u}}(\hat{X}, t)$ and $\bar{\theta}(\hat{X}, t)$:

$$\begin{aligned} \mathcal{V}_u &= \{ \mathbf{v} : v = \hat{\mathbf{u}}_P \text{ on } \hat{\Gamma}_{D_u}, \mathbf{v} \text{ sufficiently regular} \}, \\ \mathcal{V}_u^0 &= \{ \mathbf{v} : v = \mathbf{0} \text{ on } \hat{\Gamma}_{D_u}, \mathbf{v} \text{ sufficiently regular} \}, \\ \mathcal{V}_\theta &= \{ v : v = \bar{\theta}_P \text{ on } \hat{\Gamma}_{D_\theta}, v \text{ sufficiently regular} \}, \\ \mathcal{V}_\theta^0 &= \{ v : v = 0 \text{ on } \hat{\Gamma}_{D_\theta}, v \text{ sufficiently regular} \}. \end{aligned} \tag{28}$$

The exact meaning of *sufficiently regular* is not elaborated here (see eg. Brenner and Scott [16]). The weak form of the ALE boundary value problem derived in the previous section can now be stated as: Find $\hat{\mathbf{u}} \in \mathcal{V}_u$ and $\bar{\theta} \in \mathcal{V}_\theta$ such that

$$\begin{aligned} R_u^w(\hat{\mathbf{u}}, \bar{\theta}; \delta\hat{\mathbf{u}}) &= 0 \quad \forall \delta\hat{\mathbf{u}} \in \mathcal{V}_u^0, \\ R_\theta^w(\hat{\mathbf{u}}, \bar{\theta}; \delta\bar{\theta}) &= 0 \quad \forall \delta\bar{\theta} \in \mathcal{V}_\theta^0, \end{aligned} \tag{29}$$

where the residuals are obtained by inserting the aforementioned Robin-type boundary conditions into the integral expressions in Eqs. (26), (27):

$$\begin{aligned} R_u^w(\hat{\mathbf{u}}, \bar{\theta}; \delta\hat{\mathbf{u}}) &:= \hat{\rho} \int_{\hat{\Omega}} \delta\hat{\mathbf{u}} \cdot d_{tt}\hat{\mathbf{u}} \, dV \\ &\quad + 2\hat{\rho} \int_{\hat{\Omega}} \delta\hat{\mathbf{u}} \cdot \left[(d_t\hat{\mathbf{u}}) \otimes \hat{\mathbf{v}} \right] \cdot \bar{\mathbf{v}} \, dV \\ &\quad + \int_{\hat{\Omega}} (\delta\hat{\mathbf{u}} \otimes \hat{\mathbf{v}}) : \hat{\mathbf{P}}^{\text{TOT}} \, dV + \int_{\hat{\Omega}} \delta\hat{\mathbf{u}} \cdot \hat{\mathbf{r}} \, dV \\ &\quad - \int_{\hat{\Omega}} \delta\hat{\mathbf{u}} \cdot \hat{\mathbf{B}}^{\text{TOT}} \, dV - \int_{\hat{\Gamma}_{R_u}} \delta\hat{\mathbf{u}} \cdot \hat{\mathbf{T}}_P \, dA \\ &\quad + \hat{\rho} \int_{\hat{\Gamma}_{R_u}} \delta\hat{\mathbf{u}} \cdot (\hat{\mathbf{H}} \cdot \bar{\mathbf{v}})(\bar{\mathbf{v}} \cdot \hat{\mathbf{N}}) \, dA, \end{aligned} \tag{30}$$

$$\begin{aligned} R_\theta^w(\hat{\mathbf{u}}, \bar{\theta}; \delta\bar{\theta}) &:= 3K\alpha\theta^{\text{ref}} \int_{\hat{\Omega}} \delta\bar{\theta} \mathbf{I} : d_t \hat{\mathbf{H}} \, dV \\ &\quad + 3K\alpha\theta^{\text{ref}} \int_{\hat{\Gamma}} \delta\bar{\theta} (\hat{\mathbf{H}} \cdot \bar{\mathbf{v}}) \cdot \hat{\mathbf{N}} \, dA \\ &\quad - 3K\alpha\theta^{\text{ref}} \int_{\hat{\Omega}} (\hat{\mathbf{v}}\delta\bar{\theta}) \cdot (\hat{\mathbf{H}} \cdot \bar{\mathbf{v}}) \, dV \\ &\quad + \int_{\hat{\Omega}} (\hat{\mathbf{v}}\delta\bar{\theta}) \cdot [k\hat{\mathbf{v}}\bar{\theta} - \hat{\rho}c\bar{\theta}\bar{\theta}] \, dV \\ &\quad + \hat{\rho}c \int_{\hat{\Omega}} \delta\bar{\theta} d_t \bar{\theta} \, dV - \int_{\hat{\Omega}} \delta\bar{\theta} \hat{\mathbf{r}} \, dV \end{aligned}$$

$$\begin{aligned} &+ \int_{\hat{\Gamma}_{R_\theta}} \delta\bar{\theta} \hat{q}_{\hat{N},P} \, dA \\ &+ \hat{\rho}c \int_{\hat{\Gamma}_{R_\theta}} \delta\bar{\theta} \bar{\theta} (\bar{\mathbf{v}} \cdot \hat{\mathbf{N}}) \, dA. \end{aligned} \tag{31}$$

3.3 Finite element formulation

A finite element formulation of the problem based on plane strain and linear elasticity is now presented. Voigt matrix notation is employed. Displacement and temperature fields are approximated by piecewise linear or piecewise quadratic functions: Shape function matrices for displacement and temperature are denoted by \underline{N}_u and \underline{N}_θ , respectively. Furthermore, $\underline{B}_u := \hat{\mathbf{v}}_u \underline{N}_u$ and $\underline{B}_\theta := \hat{\mathbf{v}}_\theta \underline{N}_\theta$, where

$$\hat{\mathbf{v}}_u := \begin{bmatrix} \frac{\partial}{\partial \hat{X}} & 0 \\ 0 & \frac{\partial}{\partial \hat{Y}} \\ \frac{\partial}{\partial \hat{Y}} & 0 \\ 0 & \frac{\partial}{\partial \hat{X}} \end{bmatrix}, \quad \hat{\mathbf{v}}_\theta := \begin{bmatrix} \frac{\partial}{\partial \hat{X}} \\ \frac{\partial}{\partial \hat{Y}} \end{bmatrix}. \tag{32}$$

Inserting solution field approximations and employing Galerkin test functions yields the FE formulation

$$\begin{aligned} \underline{M}_{uu} \ddot{\underline{\mathbf{u}}} + \underline{C}_{uu} \dot{\underline{\mathbf{u}}} + \underline{K}_{uu} \underline{\mathbf{u}} + \underline{K}_{u\theta} \bar{\theta} &= \underline{f}_{uv} + \underline{f}_{us}, \\ \underline{C}_{\theta u} \dot{\underline{\mathbf{u}}} + \underline{K}_{\theta u} \underline{\mathbf{u}} + \underline{C}_{\theta\theta} \dot{\bar{\theta}} + \underline{K}_{\theta\theta} \bar{\theta} &= \underline{f}_{\theta v} + \underline{f}_{\theta s}, \end{aligned} \tag{33}$$

where

$$\begin{aligned} \underline{M}_{uu} &= \hat{\rho} \int_{\hat{\Omega}} \underline{N}_u^T \underline{N}_u \, dV, \\ \underline{C}_{uu} &= 2\hat{\rho} \int_{\hat{\Omega}} \underline{N}_u^T \bar{\mathbf{v}}_1 \underline{B}_u \, dV, \\ \underline{K}_{uu} &= \int_{\hat{\Omega}} \underline{B}_u^T \underline{E}^{\text{TOT}} \underline{B}_u \, dV \\ &\quad + \hat{\rho} \int_{\hat{\Omega}} \underline{N}_u^T \bar{\mathbf{v}}_r \underline{B}_u \, dV + \hat{\rho} \int_{\hat{\Gamma}_{R_u}} (\bar{\mathbf{v}} \cdot \hat{\mathbf{N}}) \underline{N}_u^T \bar{\mathbf{v}}_1 \underline{B}_u \, dA, \\ \underline{K}_{u\theta} &= -3K\alpha \int_{\hat{\Omega}} \underline{B}_u^T \mathbf{1} \underline{N}_\theta \, dV, \\ \underline{f}_{uv} &= \int_{\hat{\Omega}} \underline{N}_u^T \hat{\mathbf{B}}^{\text{TOT}} \, dV, \\ \underline{f}_{us} &= \int_{\hat{\Gamma}_{R_u}} \underline{N}_u^T \hat{\mathbf{T}}_P \, dA \\ \underline{C}_{\theta u} &= 3K\alpha\theta^{\text{ref}} \int_{\hat{\Omega}} \underline{N}_\theta^T \mathbf{1}^T \underline{B}_u \, dV, \\ \underline{K}_{\theta u} &= 3K\alpha\theta^{\text{ref}} \int_{\hat{\Gamma}_{R_\theta}} \underline{N}_\theta^T (\hat{\mathbf{N}} \otimes \bar{\mathbf{v}})^T \underline{B}_u \, dA \\ &\quad - 3K\alpha\theta^{\text{ref}} \int_{\hat{\Omega}} \underline{B}_\theta^T \bar{\mathbf{v}}_1 \underline{B}_u \, dV, \\ \underline{C}_{\theta\theta} &= \hat{\rho}c \int_{\hat{\Omega}} \underline{N}_\theta^T \underline{N}_\theta \, dV, \\ \underline{K}_{\theta\theta} &= k \int_{\hat{\Omega}} \underline{B}_\theta^T \underline{B}_\theta \, dV - \hat{\rho}c \int_{\hat{\Omega}} \underline{B}_\theta^T \bar{\mathbf{v}} \underline{N}_\theta \, dV \end{aligned}$$

$$\begin{aligned}
 & + \hat{\rho}c \int_{\hat{\Gamma}_{R_\theta}} (\bar{\mathbf{v}} \cdot \hat{\mathbf{N}}) \underline{\mathbf{N}}_\theta^T \underline{\mathbf{N}}_\theta dA, \\
 \underline{\mathbf{f}}_{\theta v} & = \int_{\hat{\Omega}} \underline{\mathbf{N}}_\theta^T \hat{\mathbf{r}} dV, \\
 \underline{\mathbf{f}}_{\theta s} & = - \int_{\hat{\Gamma}_{R_\theta}} \underline{\mathbf{N}}_\theta^T \hat{q}_{\hat{\mathbf{N}}, P} dA.
 \end{aligned}$$

Here, $(\mathbf{E}^{\text{TOT}})_{ijkl} = E_{ijkl} - \hat{\rho} \delta_{ik} \bar{v}_j \bar{v}_l$ (\mathbf{E}^{TOT} is the Voigt matrix representation of \mathbf{E}^{TOT}), $\underline{\mathbf{1}} = [1 \ 1 \ 0 \ 0]^T$, and $\bar{\mathbf{v}}_l$ and $\bar{\mathbf{v}}_r$ are the Voigt matrix representations of the tensors $\delta_{ij} \bar{v}_k$ and $\delta_{ij} (D_r \bar{v}_k - (\bar{v}_k \bar{v}_l)_{,l})$, respectively.

In the above FE formulation, the “ $u\theta$ ”- and “ θu ”-terms represent the thermomechanical coupling effects previously described under Eq. (24).

Recall from Sect. 3.1 that the time dependence of the problem is confined to the solution fields and the loads when the translational and rotational motion of the system is constant in time. It is clear from the above that this property is manifested as time-independent matrices in the FE formulation.

In the stationary case, the FE equations reduce to the time-independent system

$$\begin{aligned}
 \underline{\mathbf{K}}_{uu} \hat{\mathbf{u}} + \underline{\mathbf{K}}_{u\theta} \hat{\boldsymbol{\theta}} & = \underline{\mathbf{f}}_{uv} + \underline{\mathbf{f}}_{us}, \\
 \underline{\mathbf{K}}_{\theta u} \hat{\mathbf{u}} + \underline{\mathbf{K}}_{\theta\theta} \hat{\boldsymbol{\theta}} & = \underline{\mathbf{f}}_{\theta v} + \underline{\mathbf{f}}_{\theta s}.
 \end{aligned} \tag{34}$$

4 Element choice and numerical stabilization

Previous studies [12] indicated that, at least for rolling speeds up to the order of a few hundred km/h, no stability problems arise related to the discretized momentum balance equation for the present implementation. By contrast, various numerical problems have been found to have a prominent influence for the discretized energy balance equation, even for very modest rolling speeds. The numerical problems are manifested as node-to-node oscillations in the plate domain and oscillations together with a damped temperature profile in the cylinder domain. The former case, involving a uniform convective velocity field that intersects the boundaries of the domain, is well understood and amenable to a standard application of the SUPG method. The implementation and performance of this method will not be elaborated further in this paper, see instead the references below. The latter case— involving circular, closed convective streamlines—has been found to pose more of a challenge to these techniques, however.

The numerical stabilization methods employed in this paper is the SUPG method (see Donéa and Huerta [17] and Codina et al. [18] (for quadratic elements)) and an approach employing a variant of residual-free bubbles [19,20].

The employed bubble function approach bears similarities to that of Brezzi et al. [21], and is implemented as follows:

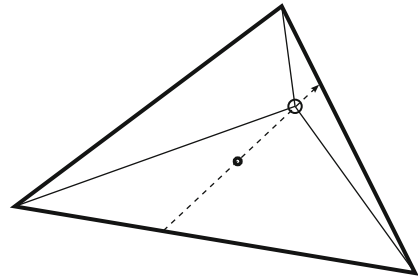


Fig. 2 Illustration of local element subgrid used in the bubble function scheme

In each triangular element, an additional node is inserted, resulting in a subdivision into three triangles (see Fig. 2). The extra node is positioned along the directed line segment represented in the figure by a dashed arrow. This line segment passes through the element centroid (the black dot) and is parallel with the direction of the convective velocity evaluated at the centroid. The position of the node along this line segment is chosen to correspond to the stationary point of the analytical solution along the line segment, of the pertinent 1D convection-diffusion problem. The shape functions related to this node (the bubble functions) thus serve as a rough approximation of the shape of the solution in the element. Further, their support coincides with the given element, so static condensation can be used to keep the global degree of freedom set unchanged. The bubbles will be chosen as piecewise polynomials of the same order as that of the global approximation (even though it is possible to choose these functions independently).

The local subgrid is treated as a standard FE mesh—no two shape functions are nonzero at any node (not even the added node). This means that the stated subgrid enrichment scheme is equivalent to a standard Galerkin formulation featuring an enriched discrete function space (i.e. on a refined mesh) [22]. The choice of the positions of the extra nodes in this refined mesh have been informed by appropriate observations of the convective velocity field, as discussed above.

To illustrate the aforementioned numerical difficulties arising for sufficiently high convective velocities in the cylinder domain, a simple Eulerian formulation of stationary, pure heat transfer is considered (cf. Eq. (23)):

$$\mathbf{a} \cdot \nabla \theta + \mathbf{q} \cdot \nabla = s, \tag{35}$$

where θ is the temperature, \mathbf{q} is the heat flux and s is the external heat source. Further,

$$\mathbf{a} = \rho c \bar{\mathbf{v}},$$

where ρ is the density, c is the mass-specific heat capacity and $\bar{\mathbf{v}}$ is the convective velocity. A two-dimensional annular

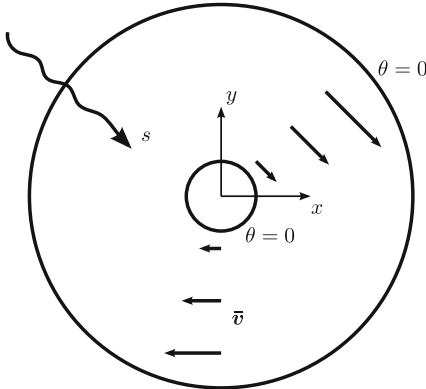


Fig. 3 Illustration of the problem used to study the influence of numerical instability

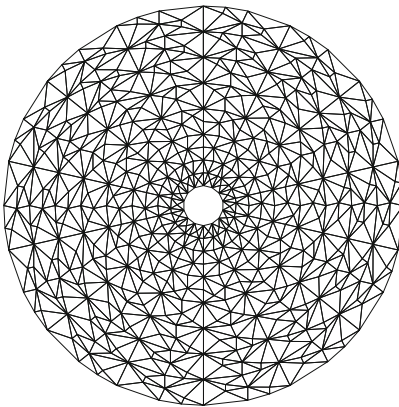


Fig. 4 Mesh used for the annular domain

domain is considered, in which the convective velocity field is

$$\vec{v}(r) = \omega r \mathbf{e}_\varphi = \omega(y, -x),$$

where ω is the angular velocity, r is the distance from the center and \mathbf{e}_φ is the circumferential unit vector. The temperature is fixed to zero at both the inner and the outer boundary and the external heat source s is uniform. Figure 3 shows a schematic illustration of the considered problem. It is noted that the geometry, boundary conditions and loads result in a problem that is one-dimensional (radially symmetric) and has an analytical solution independent of ω [23].

Results presented below correspond to a finite element solution of Eq. (35). The mesh used (deliberately unstructured) is shown in Fig. 4. Gaussian quadrature of order 5 (7 integration points) is employed. Unless otherwise stated, the parameters used are as follows: Outer and inner radii of the cylinder $r_o = 50$ cm and $r_i = 5$ cm and external heat

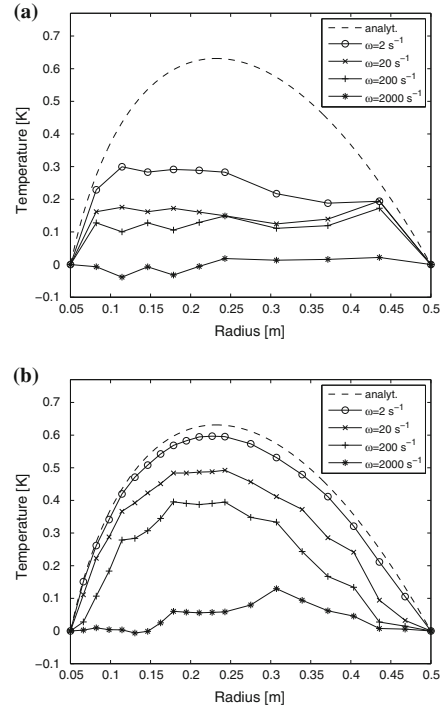


Fig. 5 Temperature distribution along radial line segment for the studied test problem. No numerical stabilization. **a** Linear elements, **b** Quadratic elements

source $s = 1000 \text{ Wm}^{-3}$. Material parameters are chosen to represent a standard steel material.

Figure 5a, b show the temperature distribution along the radial line segment $x = 0, y < 0$ for varying ω and for linear and quadratic shape functions, respectively. Figures 6, 7 show the same thing, but implementing a SUPG stabilization method and the stated bubble function method, respectively.

The decay (due to spurious numerical dissipation) of the solution for an increasing rotation speed ω is clear from Fig. 5, as is the presence of numerical oscillations. As seen in Fig. 6, the SUPG method is able to smooth out the response, but unable to deal with the numerical damping effect: instead seemingly exacerbating it. The same can in general be said for the bubble function approach using linear elements (Fig. 7a), while the use of quadratic elements seems to work much better (see Fig. 7b). It should be noted that an integration order of at least four was found to be necessary in the latter case: below that, the solution started to decay.

In summary, the following choice of element and stabilization scheme has been found to be the most effective in reducing the influence of the aforementioned numerical issues: linear elements and a SUPG method in the plate domain (details

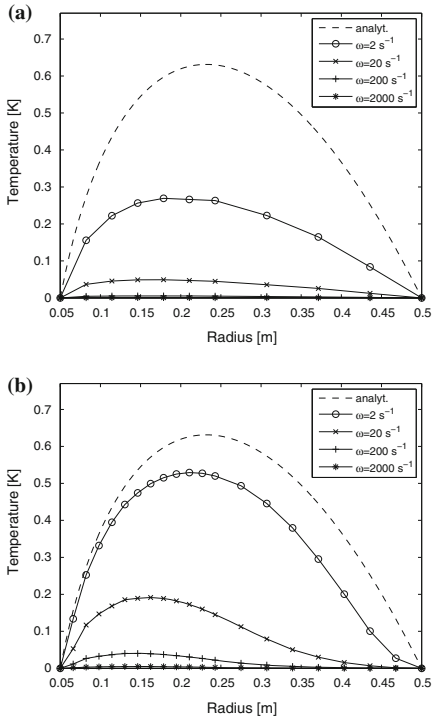


Fig. 6 Temperature distribution along radial line segment for the studied test problem. SUPG stabilization. **a** Linear elements. **b** Quadratic elements

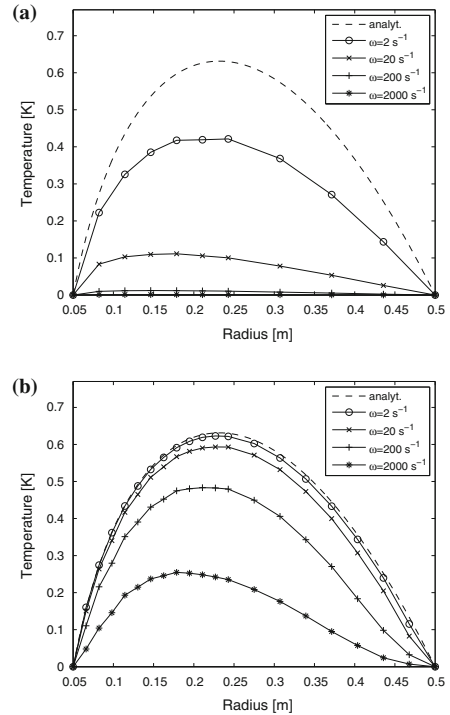


Fig. 7 Temperature distribution along radial line segment for the studied test problem. Bubble function stabilization. **a** Linear elements. **b** Quadratic elements

not shown here), quadratic elements and a bubble function scheme such as described above in the cylinder domain (see Figs. 5, 6, 7). An integration order of four for the Gauss quadrature is used. Due to the similarity between the problem studied here and the rolling contact problem studied in Sect. 6, it is likely that the scheme described above will be suitable also for the latter, although a mesh convergence study is necessary to ascertain numerically robust results for the specific cases studied.

Remark 3 A comparison between Figs. 5b and 7b shows that the implemented bubble function scheme serves to reduce both the spurious numerical oscillations and the amount of spurious numerical dissipation. It is plausible that an unbiased mesh refinement scheme—where the extra node is instead placed in the centroid of each element—would provide a stronger reduction of the numerical dissipation, but at the cost of a poorer ability of diminishing the numerical oscillations. The test problem studied here exhibits a high degree of symmetry, which means that the influence of numerical instability (oscillatory behaviour) is especially weak. A problem that is more true to life is likely to be less

symmetrical and thus more sensitive to numerical instability. The need for the stabilizing effect of the bubble function scheme would be clearer in such a case.

5 Contact formulation

The employed contact formulation is presented below in the context of the ALE description. As the focus of this paper lies elsewhere than in realistic contact interface modelling, the simplest possible laws are chosen for this purpose. However, it is emphasized that the computational framework has been constructed with modularity and extensibility in mind. The implementation of more complex contact laws should therefore be straightforward. Examples of more advanced mechanical/thermal contact interface laws (for frictionless contact), based on microgeometrical and statistical considerations, can be found in [24–28]. Furthermore, [29] is noted, in which homogenization of thermal contact resistances is suggested.

The presentation given below of the mechanical and thermal components of the implemented contact formulation relies heavily on concepts described in Wriggers [8].

5.1 Mechanical contact formulation

A standard penalty method is employed for the formulation of normal mechanical contact. This involves applying a penalty traction at each point $\hat{X} \in \hat{\Omega}$ on the cylinder surface (here denoted the “slave” surface) that, in the deformed configuration $\hat{\omega}$, penetrates the plate surface (here denoted the “master” surface). This traction is proportional to the gap function g (the negative of the penetration distance) and is directed normal to the master surface. An opposing traction is applied at the point $\hat{X}^m(\hat{X}) = \hat{\varphi}^{-1}(\hat{x}^m(\hat{x}))$ on the master surface, i.e. the point in $\hat{\Omega}$ corresponding to $\hat{x}^m(\hat{x})$: the normal projection of $\hat{x} = \hat{\varphi}(\hat{X})$ on the deformed master surface. Assigning superscripts “s” and “m” to terms related to the slave and master surfaces, respectively, enables formulation of the normal contact tractions as

$$\begin{aligned} \mathbf{t}_{nm}^s(\hat{X}) &= t_n \hat{\mathbf{n}} \quad \text{for } \hat{X} \in \hat{\Gamma}_{\text{cand}}^s, \\ \mathbf{t}_{nm}^m(\hat{X}^m(\hat{X})) &= -\mathbf{t}_{nm}^s(\hat{X}) \quad \text{for } \hat{X} \in \hat{\Gamma}_{\text{cand}}^s, \end{aligned} \tag{36}$$

where $\hat{\mathbf{n}}$ is the normal of the deformed master surface at $\hat{X}^m(\hat{X})$, $\hat{\Gamma}_{\text{cand}}^s$ is the candidate contact surface subset of the slave surface $\partial\hat{\Omega}^s$ and

$$t_n = \epsilon(-g) \tag{37}$$

is the scalar $\hat{\mathbf{n}}$ -component of the normal contact force acting on the slave surface. Here, ϵ is the penalty stiffness,

$$g(\hat{X}) = (\hat{x} - \hat{x}^m) \cdot \hat{\mathbf{n}} = (\hat{\varphi}(\hat{X}) - \hat{\varphi}(\hat{X}^m(\hat{X}))) \cdot \hat{\mathbf{n}} \tag{38}$$

is the gap function corresponding to the pair of points \hat{X} and $\hat{X}^m(\hat{X})$ and $\langle \cdot \rangle$ are Macaulay brackets. Note that in theory, $\lim_{\epsilon \rightarrow \infty} g = 0$. In a practical numerical implementation, an increased penalty stiffness ϵ leads to a decreased absolute value of the gap function, but an excessive increase leads to ill-conditioning of the discretized equation system. ϵ is typically taken as mesh-dependent, scaling inversely with some measure of the mesh size (thus having a higher value in more refined regions) [8]. For the purposes of the current implementation, the simple choice $\epsilon = \epsilon_n/h$ is deemed adequate, where ϵ_n is a constant and h is a local measure of mesh size. Note that this choice results in the desired property $\lim_{h \rightarrow 0} \epsilon = \infty \Rightarrow \lim_{h \rightarrow 0} g = 0$.

If $\hat{\Gamma}_{\text{c}}^s \subset \hat{\Gamma}_{\text{cand}}^s$ is the contact surface—the subset of the slave surface corresponding to negative gap functions—the

contribution to the weak form residual (30) due to the contact tractions is

$$\begin{aligned} R_{u,c}^w(\delta \hat{\mathbf{u}}, \hat{\mathbf{u}}) &= \int_{\hat{\Gamma}_{\text{cand}}^s} \delta \hat{\mathbf{u}}(\hat{X}) \cdot \mathbf{t}_{nm}^s(\hat{X}) \, d\mathcal{L} \\ &\quad + \int_{\hat{\Gamma}_{\text{cand}}^m} \delta \hat{\mathbf{u}}(\hat{X}^m(\hat{X})) \cdot \mathbf{t}_{nm}^m(\hat{X}^m(\hat{X})) \, d\mathcal{L} \\ &= \int_{\hat{\Gamma}_{\text{c}}^s} \epsilon g(\hat{X}) [\delta \hat{\mathbf{u}}(\hat{X}^m(\hat{X})) - \delta \hat{\mathbf{u}}(\hat{X})] \cdot \mathbf{n}(\hat{X}) \, d\mathcal{L}. \end{aligned} \tag{39}$$

Introducing Galerkin test functions ($\delta \hat{\mathbf{u}} \rightarrow \underline{N}_u \underline{\mathbf{c}}_u$) results in the following contribution to the left-hand side of the finite element formulation (33a):

$$\int_{\hat{\Gamma}_{\text{c}}^s} \epsilon g(\hat{X}) [\underline{N}_u^T(\hat{X}^m(\hat{X})) - \underline{N}_u^T(\hat{X})] \underline{\mathbf{n}}(\hat{X}) \, d\mathcal{L}.$$

At this point, the discretization of the master and slave surfaces is introduced. Linear contact elements are used regardless of the order of the elements used for the discretization of the contacting bodies. This is for compatibility reasons in case the latter discretizations are of different orders. The above expression is in this context evaluated via a one-point quadrature scheme with the integration points coinciding with the nodes of the discretized slave surface (see Wriggers [8]). The result is the finite element load vector pertaining to the normal mechanical contact interaction, to be added to the right-hand side of Eq. (33)a:

$$\underline{\mathbf{f}}_{u,c}(\underline{\mathbf{x}}) = \sum_{i=1}^{n_c} W_i \epsilon g_i [\underline{N}_u^T(\hat{X}_{a_i}^m) - \underline{N}_u^T(\hat{X}_{a_i})] \underline{\mathbf{n}}_i. \tag{40}$$

Here, $g_i = g(\hat{X}_{a_i})$, $\underline{\mathbf{n}}_i = \underline{\mathbf{n}}(\hat{X}_{a_i})$, W_i are integration weights (related to edge element lengths) and $\{a_i\}_{i=1}^{n_c}$ is the active set: the set of nodes in contact. $\hat{X}_{a_i}^m$ and \hat{X}_{a_i} are the undeformed positions of the respective points $\hat{x}_{a_i}^m$ and \hat{x}_{a_i} in the deformed configuration, where $\hat{x}_{a_i}^m$ is the point on the master surface closest to the point \hat{x}_{a_i} . Figure 8 illustrates a contact element in the deformed discretized domain. Here, $W_i = \frac{1}{2}(W_i^l + W_i^r)$.

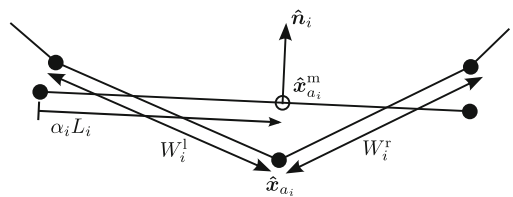


Fig. 8 The i :th contact element. The length of the master element is L_i

5.2 Thermal contact formulation

The formulation of thermal conduction in the contact region is derived in a manner analogous to the case of normal mechanical contact. A “penalty” heat flux proportional to the temperature difference is imposed on surfaces in contact:

$$q_{n,c}^s(\hat{X}) = \begin{cases} k_c \Delta\theta & \hat{X} \in \hat{F}_c^s \\ 0 & \hat{X} \notin \hat{F}_c^s \end{cases},$$

$$q_{n,c}^m(\hat{X}^m(\hat{X})) = -q_{n,c}^s(\hat{X}), \tag{41}$$

where k_c is the (velocity-independent) contact conductivity and

$$\Delta\theta(\hat{X}) = \theta(\hat{X}) - \theta(\hat{X}^m(\hat{X})) = \bar{\theta}(\hat{X}) - \bar{\theta}(\hat{X}^m(\hat{X})) \tag{42}$$

is the temperature difference. Note that perfect thermal contact is represented by $\lim_{k_c \rightarrow \infty} \Delta\theta = 0$. That is, the contact conductivity k_c would play a role similar to that of the penalty stiffness ϵ in the mechanical normal contact formulation. However, k_c should here in general be interpreted as a physical conductivity pertaining to the surface properties at the contact. In reality, this parameter exhibits a complex dependence on e.g. microgeometry, third body characteristics and contact pressure. However, following the stated ambition to keep the contact interface model as simple as possible, k_c is taken as constant. This choice is adequate for the purposes of the present paper, but would obviously be an oversimplification in implementations striving for more realistic modelling of the contact interface.

The contribution from the contact fluxes to the weak form residual (31) is

$$R_{\bar{\theta},c}^w(\hat{u}, \bar{\theta}; \delta\bar{\theta}) = \int_{\hat{F}_{cand}^{fs}} \delta\bar{\theta}(\hat{X}) q_n^s(\hat{X}) d\mathcal{L} + \int_{\hat{F}_{cand}^{ms}} \delta\bar{\theta}(\hat{X}^m(\hat{X})) q_n^m(\hat{X}^m(\hat{X})) d\mathcal{L} = \int_{\hat{F}_c^s} k_c \Delta\theta(\hat{X}) [\delta\bar{\theta}(\hat{X}) - \delta\bar{\theta}(\hat{X}^m(\hat{X}))] d\mathcal{L}. \tag{43}$$

Introducing Galerkin test functions ($\delta\bar{\theta} \rightarrow \underline{N}_{\bar{\theta}} \underline{c}_{\bar{\theta}}$) and employing one-point quadrature as above yields the finite element load vector pertaining to the interfacial thermal conduction, to be added to the right-hand side of Eq. (33)b:

$$\underline{f}_{\bar{\theta},c}(\bar{\theta}) = \sum_{i=1}^{n_c} W_i k_c [\underline{N}_{\bar{\theta}}^T(\hat{X}_{a_i}) - \underline{N}_{\bar{\theta}}^T(\hat{X}_{a_i}^m)] \Delta\bar{\theta}_i, \tag{44}$$

where, $\Delta\bar{\theta}_i = \Delta\bar{\theta}(\hat{X}_{a_i})$.

5.3 Solution method

The addition of the (generally nonlinear) contact contributions (40) and (44) to the (otherwise linear) FE formulation of the thermomechanical boundary value problem (Eq. (33)) leads to a nonlinear equation system. This system is solved monolithically by the Newton method (which requires linearization of the contact contributions, although these expressions are not shown in this paper).

The employed contact iteration scheme is identical to the one described in Wriggers [8]: In each iteration of the Newton solver, the residual vector and the tangent stiffness matrix are constructed, followed by an update of the solution guess. The construction of the residual and the tangent involves a contact search procedure, a central step of which being the identification of the set of active nodes (using the contact condition $g_i < 0$).

6 Numerical investigations

6.1 Numerical model

The following numerical examples are based on a 2D (plane strain) model of an annular cylinder rolling on a plate. Owing to the convective ALE description, the latter can be kept fairly short, regardless of the actual distance traversed by the cylinder during a simulation. As mentioned in Sect. 3, the model features an isotropic, homogeneous, linear elastic material. Pure rolling and constant rolling velocity (velocity of the cylinder centre relative to a fixed coordinate system) are assumed. A vertical distributed load is applied along the inner boundary of the cylinder. In addition, a constant normal heat flux is applied to given sections of the cylinder perimeter (each having an angular extension of 45°). Gravitational loads on the bodies are not included. The base of the plate is fixed in all degrees of freedom and the cylinder inner boundary is fixed in the horizontal direction. All other boundaries are free. The temperature at the plate ends is fixed (to the reference temperature) while all other boundaries (not in contact) are thermally insulated. Figure 9 shows a schematic illustration of the geometry, boundary conditions and loads in the employed model. It is noted that these exhibit vertical symmetry.

A standard parameter setup (used in the following simulations unless otherwise indicated) is now defined. Material parameters for cylinder and plate are: Young’s modulus $E = 200$ GPa, Poisson’s ratio $\nu = 0.3$, specific heat capacity $c = 460$ Jkg⁻¹K⁻¹, thermal conductivity $k = 45$ Wm⁻¹K⁻¹, thermal expansion coefficient $\alpha = 4.8 \cdot 10^{-6}$ K⁻¹, density $\rho = 8 \cdot 10^3$ kgm⁻³. Outer and inner radii of the cylinder are $r_o = 50$ cm and $r_i = 5$ cm, respectively. The height of the plate is $h = 0.1$ m and the width of the plate domain is

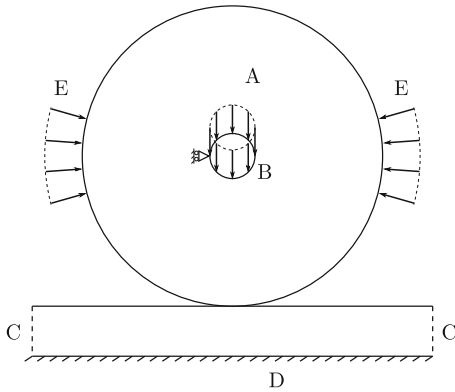


Fig. 9 Schematic illustration of the thermomechanical model. *A* applied mechanical load, *B* cylinder inner boundary (fixed in horizontal direction), *C* artificial plate domain ends (fixed temperature), *D* plate base (fixed in all degrees of freedom), *E* interfaces with prescribed heat flux

chosen as $b = 1$ m. The contact conductivity is $k_c = 10^7 \text{ Wm}^{-2} \text{ K}^{-1}$ and the penalty stiffness is $\epsilon_N = 5 \text{ TN/m}$. The reference (environmental) temperature is $\theta^{\text{ref}} = 293 \text{ K}$. The mechanical load is $P = 10 \text{ kN/m}$ and the heat flux into the cylinder at each interface *E* is $W_{\text{in}} = 30 \text{ W/m}$.

The rolling velocity is chosen as constant with magnitude $\bar{v} = 50 \text{ km/h}$. The rotational velocity of the cylinder is then \bar{v}/r_0 , due to the assumption of pure rolling.

As mentioned in the discussion following Eq. (24), the Gough–Joule effect is negligible for thermoelastic materials. It will therefore not be modeled in the following numerical examples.

Much of the following presentation will study the weighted mean temperature $\bar{\theta}_m$, which for an arbitrary domain V_0 can be defined as

$$\bar{\theta}_m = \frac{1}{|V_0|} \int_{V_0} \bar{\theta} dV. \tag{45}$$

where $|V_0|$ is the volume of V_0 . In the following, V_0 will be chosen to represent the cylinder domain and the plate domain, alternatively. It should here be emphasized that in the latter case, the magnitude of the resulting mean temperature is rather arbitrary, since it depends strongly on the volume of the arbitrary domain over which the mean is taken.

6.2 Discretization

The finite element formulation of the problem is implemented in MATLAB. The element type used is a triangular element with two or one degrees of freedom per node in the mechanical and thermal problems, respectively. The approximation for both displacements and temperatures is piecewise linear

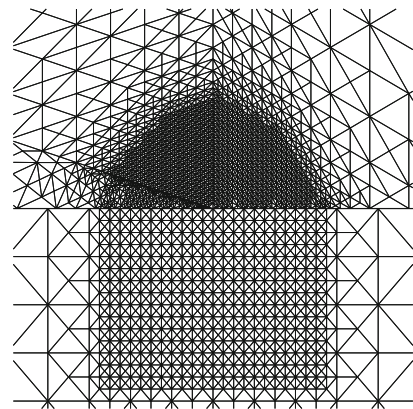
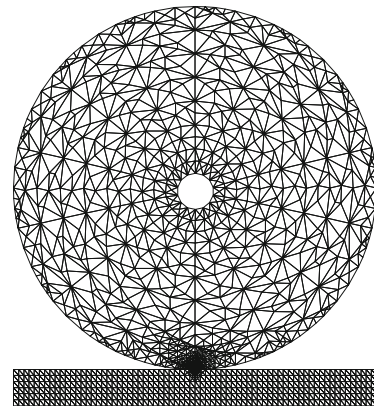


Fig. 10 The employed finite element mesh, with a zoomed-in view of the refined contact region

in the plate and piecewise quadratic in the cylinder. Note that the discrepancy in element order between cylinder and plate has implications for the contact formulation. The approach taken here is to regard both domains as linear as far as the contact formulation is concerned (as was discussed in Sect. 5.1).

The employed mesh is shown in Fig. 10. The mesh of the cylinder is constructed from a coarse basic mesh which is refined according to the following scheme: successive refinement in a series of gradually smaller domains centered at the point of initial contact \rightarrow global refinements (2 are here used) \rightarrow refinement of the largest elements along the periphery. After that, all nodes are remapped radially so that the outer nodes describe a circle. At this point, even though measures have been taken to ensure that the outer boundary is as round as possible despite local refinement near the contact region (via peripheral refinement), the centroid is inevitably slightly

displaced compared to that of the enclosing circle. This has the effect of making the resultant of the centrifugal force vector (the second component of the vector f_{mv} , see Eqs. (33), (26)) nonzero, which is unphysical for a circular domain. Further, this causes considerable errors in the contact computation. For this reason, the inner boundary is rigidly moved so that the position of the centroid of the discretized domain is corrected (thus slightly modifying the geometry). The positions of the inner nodes of the mesh are then determined by linear elastic equilibrium.

The plate domain mesh is constructed by starting from a structured mesh and refining it locally in a rectangular area centered at the point of initial contact. This area extends a distance $2d_c$ horizontally and d_c vertically, where d_c is an analytical prediction (using Hertz theory) of the contact patch size. The minimum allowed size for an element in the final mesh of the plate is 1.5 times the size of the largest element in the cylinder mesh in the most refined region.

All mesh refinements are performed according to Rivara’s longest-edge refinement technique [30], and the final mesh contains 8017 elements and 12608 nodes.

6.3 Numerical stabilization

SUPG stabilization is employed in the plate (linear elements) and a bubble function scheme (according to the description in Sect. 4) is used in the cylinder (quadratic elements). An integration order of four is employed for the Gauss quadrature.

6.4 Convergence study

A mesh convergence study is performed in which the number of global refinements of the cylinder mesh, n_r , is varied. Figure 11 shows a plot of the temperature along the radial line segment $x = 0, y < 0$ (see Fig. 3) for varying values of n_r . Note that the horizontal axis represents the dis-

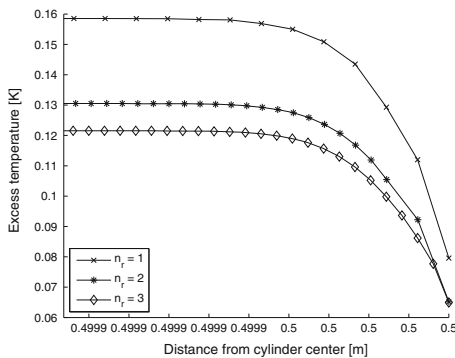


Fig. 11 Mesh convergence study

tance r from the cylinder center. The range is here limited to $r_o - d_c/5 < r < r_o$. These results indicate that the employed choice $n_r = 2$ results in a mesh that is sufficiently fine for the purposes of the subsequent numerical investigations.

6.5 Stationary analysis

Figure 12 shows the stationary temperature distribution in two small regions close to the contact patch (each having the dimensions 2 mm × 1 mm). The regions are displaced to the left: the middle of the contact patch is highlighted by a vertical gray mark. The combined influence of heat flux across the contact interface and convective effects is here evident. In particular, the skewing influence of the latter, despite the symmetrical boundary conditions and loads, is noted.

Figure 13 shows a comparison between the computed normal contact stress distribution and the analytical Hertzian solution [6,31]. It is clear from the close correspondence between the two curves that the influence of thermomechanical effects on the mechanical solution is not enough to visibly affect the contact stress distribution.

6.5.1 Influence of rolling speed

Figure 14 shows weighted mean temperatures of cylinder and plate (calculated using Eq. (45) for each subdomain) versus the rolling speed. The figure shows that the model is successful in capturing the effect of an increased cooling rate of the cylinder with increasing rolling speed (even with a velocity-independent contact conductivity k_c). Note that the free boundary of the cylinder is insulated, implying that the cause of the cylinder mean temperature decrease can only be a higher heat flux through the contact interface, in turn caused by a decreased local temperature in the plate at the contact due to an increased convection in the plate. Furthermore, the latter phenomenon leads to a higher rate of heat extraction out of the modeled plate domain (which is bounded by the artificial edges denoted by C in Fig. 9). This explains the significant decrease in mean temperature in the plate with increasing rolling speed, seen in the figure.

6.5.2 Influence of thermal contact conductivity

Figures 15 (top) and (middle) show weighted mean temperatures in cylinder and plate, respectively, versus the contact conductivity k_c . Figure 15 (bottom) shows the temperature difference between the cylinder and plate nodes of initial contact. The temperatures in cylinder and plate are seen to approach each other (although the increase in temperature in the plate is very slight), and

Fig. 12 Zoomed in plot of temperature distribution in cylinder and plate [K]. The center of the contact patch (to the right in the figure) is highlighted by a vertical gray mark

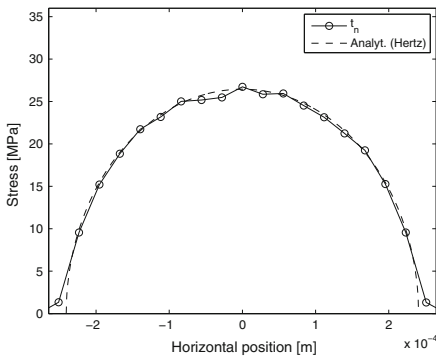
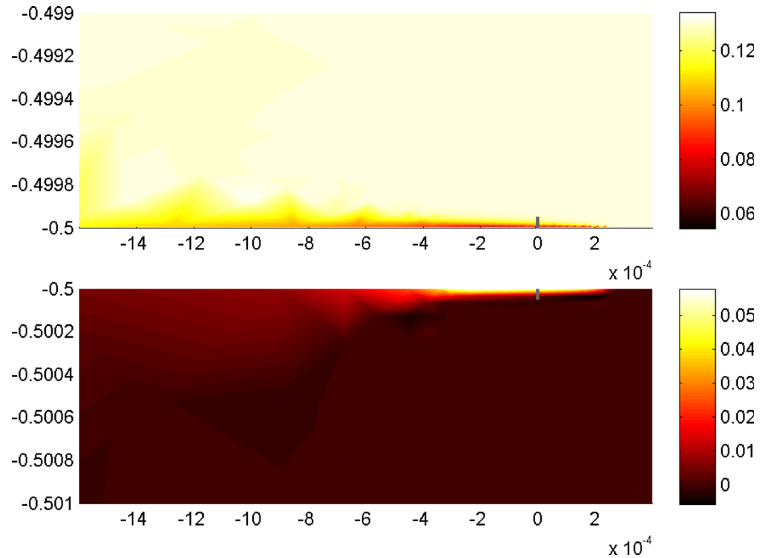


Fig. 13 Normal contact stress distribution

concluded that the interval $k_c > 10^7 \text{ Wm}^{-2}\text{K}^{-1}$ may be considered as resulting in a state of perfect thermal contact. A similar behaviour was observed in Vernersson [3], where a numerical model of wheel–rail heat transfer was used to model the rail chill effect on tread braked railway wheels.

6.5.3 Influence of mechanical load

Figures 16 (top) and (middle) show weighted mean temperatures in cylinder and plate, respectively, for varying applied mechanical load. Figure 16 (bottom) shows the contact patch width. The redistribution of temperature between cylinder and plate as the applied load increases is clear from the two upper graphs (although, also in this case, the change in mean

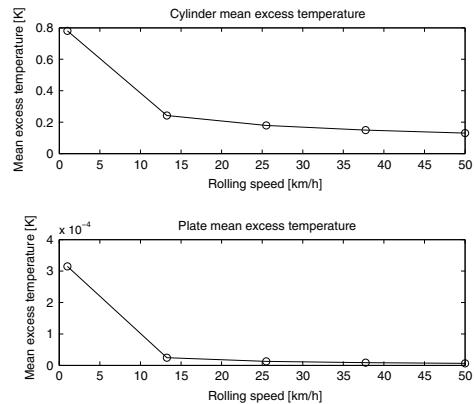


Fig. 14 Weighted mean temperatures of cylinder and plate versus rolling speed

temperature in the plate is very small), and is due to the increased contact patch width (as seen in the lower graph). Note that this effect would have been even stronger had the contact conductivity been modeled as pressure-dependent.

6.6 Transient analysis

For the transient simulations, a backward Euler time integration scheme is used. Three different scenarios involving transient processes are simulated: (i) the external heat flux W_{in} is applied at time $t = 0$, (ii) the external heat flux is retracted at $t = 0$, (iii) a sharp hole of width 0.2 mm in the plate is traversed. In all cases, the appropriate stationary solution (i.e.

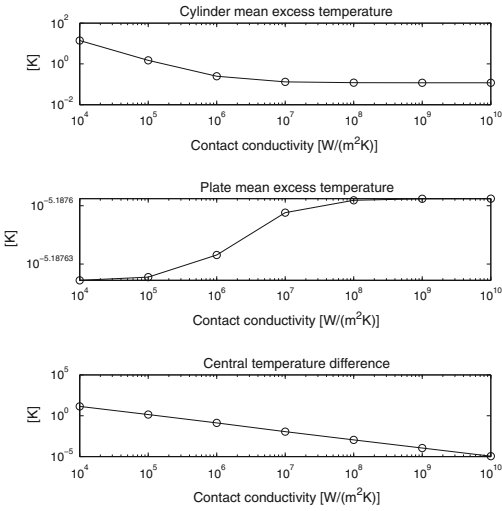


Fig. 15 Weighted mean temperatures of cylinder (*top*) and plate (*middle*) versus contact conductivity. *Bottom* temperature difference between the cylinder and plate nodes of initial contact versus contact conductivity

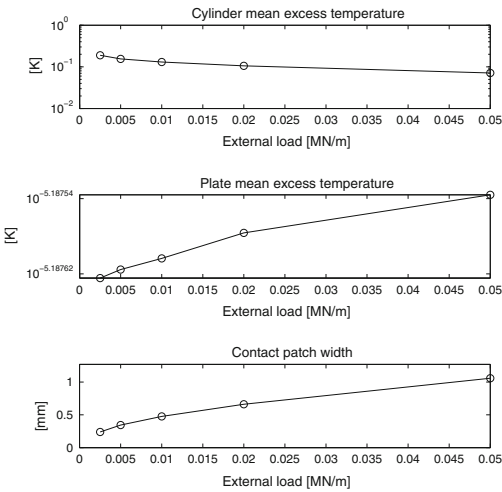


Fig. 16 Weighted mean temperatures of cylinder (*top*) and plate (*middle*) versus applied mechanical load. *Bottom* size of contact patch versus applied load

featuring i: $W_{in} = 0$, ii/iii: $W_{in} = 30 \text{ W/m}$ is employed as the initial configuration.

The plate profile used in case iii is implemented in the manner described in Draganis et al. [12], which in turn is based a methodology described in Thompson [32]. In this approach, a given offset function is imposed on the gap func-

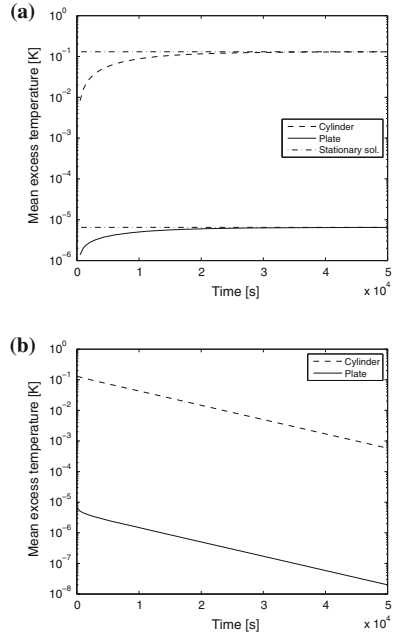


Fig. 17 Time evolution of weighted mean temperatures in cylinder and plate. **a** External heat flux applied at $t = 0$. **b** External heat flux retracted at $t = 0$

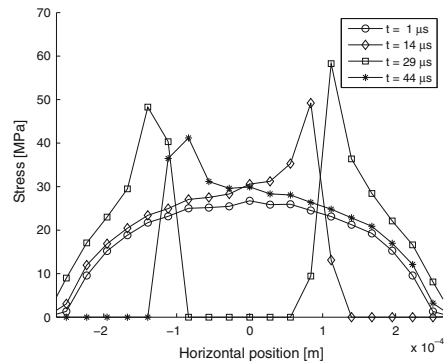


Fig. 18 Normal contact stress distribution at four distinct points in time as the hole is traversed

tions (38), effectively resulting in a modified plate profile. As time progresses, this profile will be advected through the computational domain. This approach is limited in that there is no actual modification of the plate domain—only of the gap functions. However, where applicable (e.g. when the analysis is focused on contact pressures and/or resultant contact forces), it is highly preferable to actual modifications of the computational domain in the context of an ALE description,

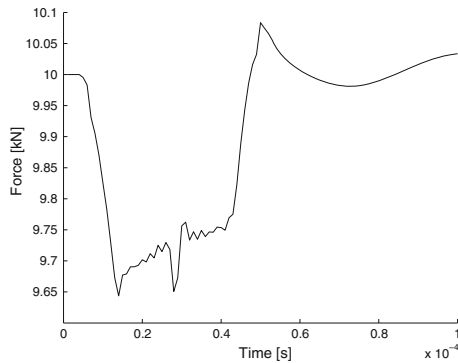


Fig. 19 Time evolution of contact force resultant as the hole is traversed

due to the intrinsic difficulty of tracking material boundaries in this case.

In cases i and ii, the time evolution of the weighted mean temperatures in both bodies is studied, while in case iii, the analysis is focused on the evolution of contact stresses and -forces as the hole in the plate is traversed. The former phenomenon occurs on a vastly larger time scale than the latter. The time steps used in the respective cases are i/ii: $\Delta t = 500$ s and iii: $\Delta t = 10^{-6}$ s. These time step sizes have been verified (details not given here) to give a numerically convergent response with respect to phenomena of interest in the present analysis. It is noted that the former time step size implies that the cylinder undergoes many revolutions per time step. In particular, this means that the simulation is unable to resolve mechanical phenomena in this case, which occur on vastly smaller time scales. However, their influence on the studied quantity in cases i and ii: the comparatively very slow evolution of the temperature distribution, is negligible. Taking into account also that the constitutive model does not include inelastic material parameters, it is concluded that the given choice of time step is admissible in this case.

Figure 17 shows the time evolution of the weighted mean temperatures in cylinder and plate for the respective cases i, ii. Figure 17a also shows the stationary solution for reference. Due to the large difference in magnitude of the cylinder and plate temperatures (discussed in previous sections), a logarithmic axis is used for the vertical axis in these figures. The exponential decay of the temperature in 17b is noted. Figure 18 shows the contact stress distribution at four distinct points in time as the hole is traversed. Figure 19 shows the time evolution of the resultant contact force. Note that in order to resolve higher frequencies of the oscillations resulting from the contact interaction at the discontinuity, a smaller time step would be required.

7 Concluding remarks

A theoretical and computational framework governing thermomechanically coupled transient rolling contact based on an ALE kinematical description has been developed. The ALE formulation allows for linearization of the mechanical response, localized mesh refinement and a compact computational domain. Further, it was shown to simplify the time-description of the transient rolling contact problem and enable the formulation of the stationary rolling problem as time-independent.

Numerical simulations featuring both mechanical and thermal loads were performed. The results showed the thermomechanical contact model (featuring a velocity-independent contact conductivity) to be able to capture the effect of convective chilling of the cylinder due to the contact with the plate. A study of the influence of the contact conductivity was performed, and results were found to correspond qualitatively to results in the literature. Further, the relation between the magnitude of the heat flux through the contact interface and the applied mechanical load (owing to the influence of the latter on the contact patch width) was emphasized. Transient simulations showed the model to be able to capture phenomena occurring on disparate time scales, as well as simulations featuring very rough contact geometries.

The convective ALE formulation of the energy balance equation was found to be sensitive to stability problems and other numerical issues in its discretized form. Numerical stabilization techniques were implemented, satisfyingly addressing these problems. Since the numerical issues manifest themselves in essentially different ways in the two domains (due to the differences in the convective velocity fields), the numerical stabilization techniques implemented in these domains had to be designed thereafter.

Upcoming work will be focused on modelling frictional contact. Particular applications of interest include modelling of stick/slip phenomena and frictional heat generation.

Acknowledgments The project is financed by the Swedish Research Council (www.vr.se) under contract 2008-3860 and is a part of the ongoing activities in the National Centre of Excellence CHARMEC (www.chalmers.se/charmec).

Open Access This article is distributed under the terms of the Creative Commons Attribution License which permits any use, distribution, and reproduction in any medium, provided the original author(s) and the source are credited.

References

1. Vernersson T et al (2010) Wheel tread damage: a numerical study of railway wheel tread plasticity under thermomechanical loading. Proc IME Part F J Rail Rapid Transit 224(5):435–443. doi:10.1243/09544097JRR358

2. Johnson KL (1989) The strength of surfaces in rolling contact. *Proc IME Part C J Mech Eng Sci* 203(3):151–163. doi:[10.1243/PIME_PROC_1989_203_100_02](https://doi.org/10.1243/PIME_PROC_1989_203_100_02)
3. Vernerström T (2006). Tread braking of railway wheels-noise-related tread roughness and dimensioning wheel temperatures. Field tests, rig measurements and numerical simulations. PhD thesis, Chalmers University of Technology
4. Teimourimaneh S, Lundén R, Vernerström T (2010). Tread braking of railway wheels-state-of-the-art survey. In: Proceedings 6th European conference on braking JEF2010, pp 293–302
5. Hertz H (1882) Über die Berührung fester elastischer Körper (On the contact of elastic solids). *J Reine Angew Math* 92: 156–171
6. Johnson KL (1987) Contact mechanics. Cambridge University Press, Cambridge. ISBN: 9780521347969
7. Kalker JJ (1990) Three-dimensional elastic bodies in rolling contact. In: Gladwell GML (ed) Solid mechanics and its applications. Kluwer Academic Publishers, Dordrecht. ISBN: 9780792307129
8. Wriggers P (2006) Computational contact mechanics. Springer, Berlin. ISBN: 9783540326083
9. Nackenhorst U (2004) The ALE-formulation of bodies in rolling contact theoretical foundations and finite element approach. *Comput Methods Appl Mech Eng* 193:299–4322. doi:[10.1016/j.cma.2004.01.033](https://doi.org/10.1016/j.cma.2004.01.033)
10. Zieffe M, Nackenhorst U (2008) Numerical techniques for rolling rubber wheels: treatment of inelastic material properties and frictional contact. *Comput Mech* 42(3):337–356. doi:[10.1007/s00466-008-0243-9](https://doi.org/10.1007/s00466-008-0243-9). ISSN 0178-7675
11. Suwannachit A, Nackenhorst U (2013) A novel approach for thermomechanical analysis of stationary rolling tires within an ALE-kinematic framework. *Tire Sci Technol* 41(3):174–195
12. Draganis A, Larsson F, Ekberg A (2012) Numerical evaluation of the transient response due to non-smooth rolling contact using an arbitrary Lagrangian-Eulerian formulation. *Proc IME Part J J Eng Tribol* 226(1):36–45. doi:[10.1177/1350650111422015](https://doi.org/10.1177/1350650111422015)
13. Ottosen NS, Ristinmaa M (2005) The mechanics of constitutive modeling. Elsevier, Amsterdam. ISBN: 9780080446066
14. Holzapfel GA (2000) Nonlinear solid mechanics: a continuum approach for engineering. Wiley, Chichester. ISBN: 9780471823193
15. Schweizer B, Wauer J (2001) Atomistic explanation of the Gough-Joule-effect. *Eur Phys J B* 23(3):383–390. doi:[10.1007/s100510170058](https://doi.org/10.1007/s100510170058). ISSN: 1434-6028
16. Brenner SC, Scott LR (2008) The mathematical theory of finite element methods. In: Marsden JE, Sirovich L, Antman SS (eds) Texts in applied mathematics, vol 15, 3rd edn. Springer, New York. doi:[10.1007/978-0-387-75934-0](https://doi.org/10.1007/978-0-387-75934-0). ISBN: 978-0-387-75933-3
17. Donéa J, Huerta A (2003) Finite element methods for flow problems. Wiley, Chichester. ISBN: 9780471496663
18. Codina R, Onate E, Cervera M (1992) The intrinsic time for the streamline upwind/Petrov–Galerkin formulation using quadratic elements. *Comput Methods Appl Mech Eng* 94(2):239–262. doi:[10.1016/0045-7825\(92\)90149-E](https://doi.org/10.1016/0045-7825(92)90149-E). ISSN: 0045-7825
19. Brezzi F et al (1992) A relationship between stabilized finite element methods and the Galerkin method with bubble functions. *Comput Methods Appl Mech Eng* 96(1):117–129. doi:[10.1016/0045-7825\(92\)90102-P](https://doi.org/10.1016/0045-7825(92)90102-P). ISSN: 0045-7825
20. Baiocchi C, Brezzi F, Franca LP (1993) Virtual bubbles and Galerkin-least-squares type methods (Ga.L.S.). *Comput Methods Appl Mech Eng* 105(1):125–141. doi:[10.1016/0045-7825\(93\)90119-1](https://doi.org/10.1016/0045-7825(93)90119-1). ISSN: 0045-7825
21. Brezzi F, Marini D, Russo A (1998) Applications of the pseudo residual-free bubbles to the stabilization of convection-diffusion problems. *Comput Methods Appl Mech Eng* 166(1–2):51–63. *Advances in Stabilized Methods in Computational Mechanics*. doi:[10.1016/S0045-7825\(98\)00082-6](https://doi.org/10.1016/S0045-7825(98)00082-6). ISSN: 0045-7825
22. Brezzi F et al (2003) Link-cutting bubbles for the stabilization of convection-diffusion-reaction problems. *Math Models Methods Appl Sci* 13(3):445–461. doi:[10.1142/S0218202503002581](https://doi.org/10.1142/S0218202503002581) [cited By (since 1996)25]
23. Hetnarski RB, Eslami R (2008) Thermal stresses-advanced theory and applications. In: Gladwell GML (ed) Solid mechanics and its applications. Springer, New York. ISBN: 9781402092466
24. Schrefler BA, Zavarise G (1993) Constitutive laws for normal stiffness and thermal resistance of a contact element. *Comput-Aided Civ Infrastruct Eng* 8(4):299–308. doi:[10.1111/j.1467-8667.tb00215.x](https://doi.org/10.1111/j.1467-8667.tb00215.x). ISSN: 1467-8667
25. Wriggers P, Zavarise G (1993) Application of augmented Lagrangian techniques for non-linear constitutive laws in contact interfaces. *Commun Numer Methods Eng* 9(10): 815–824. doi:[10.1002/cnm.1640091005](https://doi.org/10.1002/cnm.1640091005). ISSN: 1099-0887
26. Wriggers P, Zavarise G (1993) Thermomechanical contact—a rigorous but simple numerical approach. *Comput Struct* 46(1):47–53. doi:[10.1016/0045-7949\(93\)90166-B](https://doi.org/10.1016/0045-7949(93)90166-B). ISSN: 0045-7949
27. Zavarise G et al (1992) A numerical model for thermomechanical contact based on microscopic interface laws. *Mech Res Commun* 19(3):173–182. doi:[10.1016/0093-6413\(92\)90062-F](https://doi.org/10.1016/0093-6413(92)90062-F). ISSN: 0093-6413
28. Zavarise G et al (1992) Real contact mechanisms and finite element formulation—a coupled thermomechanical approach. *Int J Numer Methods Eng* 35(4):767–785. doi:[10.1002/nme.1620350409](https://doi.org/10.1002/nme.1620350409). ISSN: 1097-0207
29. Temizer I, Wriggers P (2010) Thermal contact conductance characterization via computational contact homogenization: a finite deformation theory framework. *Int J Numer Methods Eng* 83(1):27–58. doi:[10.1002/nme.2822](https://doi.org/10.1002/nme.2822). ISSN: 1097-0207
30. Rivara MC (1984) Algorithms for refining triangular grids suitable for adaptive and multigrid techniques. *Int J Numer Methods Eng* 20(4):745–756. doi:[10.1002/nme.1620200412](https://doi.org/10.1002/nme.1620200412). ISSN: 1097-0207
31. Timoshenko SP, Goodier JN (1951) Theory of elasticity. Engineering societies monographs. McGraw-Hill, New York
32. Thompson DJ (1991) Theoretical modelling of wheel-rail noise generation. *Proc IME Part F J Rail Rapid Transit* 205(2):137–149. doi:[10.1243/PIME_PROC_1991_205_227_02](https://doi.org/10.1243/PIME_PROC_1991_205_227_02)

Paper C

Finite element modelling of frictional thermomechanical rolling/sliding contact using an arbitrary Lagrangian–Eulerian formulation

FINITE ELEMENT MODELLING OF FRICTIONAL THERMOMECHANICAL ROLLING/SLIDING CONTACT USING AN ARBITRARY LAGRANGIAN–EULERIAN FORMULATION

Andreas Draganis^{1,2}, Fredrik Larsson¹ and Anders Ekberg^{1,2}

¹Department of Applied Mechanics, Chalmers University of Technology, Gothenburg, Sweden

²CHARMEC, Chalmers University of Technology, Gothenburg, Sweden

Abstract

A theoretical and computational framework for the analysis of thermomechanically coupled, frictional, stationary (steady-state) rolling contact based on an Arbitrary Lagrangian–Eulerian (ALE) kinematical description is presented. The finite element method is employed in an implementation featuring 2D cylinder–plate rolling contact, with a contact formulation including mechanical and thermal frictional contact. The ALE formulation is noted to allow for linearization of the governing equations, localized mesh refinement, a time-independent description of stationary dynamics and velocity-independent contact interface modelling, etc. Numerical simulations show the model to be able to capture e.g. stick/slip behaviour and a range of thermal phenomena, including the effect of convective cooling of the cylinder due to the contact with the plate.

Keywords: thermomechanical analysis, arbitrary Lagrangian–Eulerian, rolling contact, friction, partial slip, finite element method

1 Introduction

The current paper presents a versatile methodology for the analysis of thermomechanical, frictional, stationary (steady-state) rolling/sliding contact. The motivation for the study and the goal for the development of the model is the application to wheel–rail contact situations. Currently, such analyses are most often based on semi-analytical contact models, e.g. Hertz- and Carter theory [1, 2, 3]. Such simplified models are sufficient in many situations. For instance, wheel–rail contact analyses as a basis for train–track interaction models usually do not require high-resolution evaluation of the contact stress distribution. However, there are other cases within wheel–rail contact applications where this is vital. This includes cases where an accurate prediction of plastic deformation [4], wear [5] and/or rolling contact fatigue [6] of wheel and rail is required.

The current paper builds on previously published developments [7, 8] in order to present a finite element framework for the analysis of frictional, thermomechanically coupled rolling/sliding contact, based on an Arbitrary Lagrangian–Eulerian (ALE) kinematical description [9, 10, 11]. This approach leads to a more complicated boundary value problem, but also allows for highly localized mesh refinement, a more compact computational domain, linearization of the governing equations, a time-independent description of stationary rolling/sliding contact and velocity-independent contact interface modelling. In following sections, a 2D implementation of cylinder–plate rolling/sliding contact is em-

ployed to illustrate these points, as well as investigate the computational capabilities of the model, in terms of both mechanical and thermal characteristics.

2 Kinematical description

The employed ALE description of cylinder–plate rolling motion [9, 7, 8] can be described as follows: Two intermediate configurations are utilized in addition to the initial (“undeformed”) configuration, $\Omega \ni \mathbf{X}$, and the current (“deformed”) configuration, $\omega \ni \mathbf{x}$. The first intermediate configuration is denoted $\hat{\Omega} \ni \hat{\mathbf{X}}$. The map from Ω to $\hat{\Omega}$ accounts for a rigid body *rotation* of the cylinder and a pure *translation* of the plate. The second intermediate configuration is denoted $\hat{\omega} \ni \hat{\mathbf{x}}$. The map from $\hat{\Omega}$ to $\hat{\omega}$ accounts for the *deformation* of cylinder and plate. Both intermediate configurations feature a moving coordinate system that follows the cylinder center. The map from $\hat{\omega}$ to ω accounts for a pure translation of the system in going back to the original fixed coordinate system.

The maps between the configurations are formulated as $\hat{\mathbf{X}} = \hat{\phi}(\mathbf{X}, t)$, $\hat{\mathbf{x}} = \hat{\varphi}(\hat{\mathbf{X}}, t)$, $\mathbf{x} = \check{\phi}(\hat{\mathbf{x}}, t)$ and $\mathbf{x} = \varphi(\mathbf{X}, t)$, so that $\varphi(\mathbf{X}, t) = \check{\phi}(\hat{\varphi}(\hat{\phi}(\mathbf{X}, t), t), t)$, with corresponding deformation gradients $\hat{\mathbf{F}}$, $\hat{\mathbf{F}}$, $\check{\mathbf{f}}$ and \mathbf{F} . Figure 1 shows a schematic illustration of the employed configurations, with their intermediary maps and deformation gradients.

The rigid body maps $\hat{\mathbf{X}} = \hat{\phi}(\mathbf{X}, t)$ and $\mathbf{x} = \check{\phi}(\hat{\mathbf{x}}, t)$ can be expressed a priori from knowledge of the translational and rotational motion of the cylinder along the

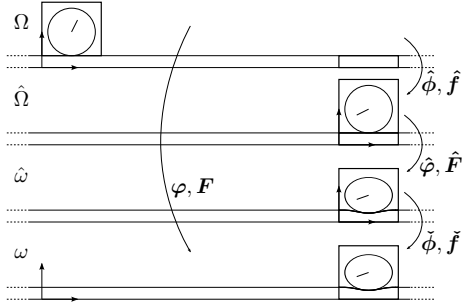


Figure 1. Illustration of configurations and maps relevant to the employed ALE description.

plate:

$$\begin{aligned} \hat{\mathbf{X}} &= \hat{\phi}(\mathbf{X}, t) \\ &= \begin{cases} \mathbf{R}(t) \cdot (\mathbf{X} - \mathbf{X}_0) + \mathbf{X}_0 & \text{for } \mathbf{X} \in \Omega^c \\ \mathbf{X} - \bar{\mathbf{X}}(t) & \text{for } \mathbf{X} \in \Omega^p \end{cases}, \end{aligned} \quad (1)$$

$$\mathbf{x} = \check{\phi}(\hat{\mathbf{x}}, t) = \hat{\mathbf{x}} + \bar{\mathbf{X}}(t) \quad \text{for } \hat{\mathbf{x}} \in \hat{\omega}, \quad (2)$$

where \mathbf{R} is a rotation tensor, \mathbf{X}_0 is the position of the cylinder centre in the undeformed configuration, $\bar{\mathbf{X}}$ is the translation of the cylinder centre, and Ω^c and Ω^p are the subsets of Ω corresponding to the cylinder and plate domains, respectively. Note that $\hat{\mathbf{f}} = \mathbf{R}$ and $\hat{\mathbf{f}} = \mathbf{I}$ in the domain of the cylinder and plate, respectively, and that $\check{\mathbf{f}} = \mathbf{I}$. The Lagrangian problem of finding the map $\mathbf{x} = \varphi(\mathbf{X}, t)$ (or the displacement $\mathbf{u}(\mathbf{X}, t) = \varphi(\mathbf{X}, t) - \mathbf{X}$) is thus narrowed down to the ALE problem of finding the map $\hat{\mathbf{x}} = \hat{\varphi}(\hat{\mathbf{X}}, t)$ (or the displacement $\hat{\mathbf{u}}(\hat{\mathbf{X}}, t) = \hat{\varphi}(\hat{\mathbf{X}}, t) - \hat{\mathbf{X}}$). For small strains, the ALE displacements $\hat{\mathbf{u}}$ will be small, which is generally not the case for the standard Lagrangian displacements \mathbf{u} . Consequently, in the former case (but not the latter) it is possible to linearize the mechanical response.

Another advantage of the presented convective kinematical description is the fact that it allows for a compact computational model: only a relatively short section of the plate domain needs to be modelled, regardless of rolling distance. Further, the position (in the intermediate domains) of the contact region in both cylinder and plate is largely stationary throughout the rolling motion, allowing for localized mesh refinement. Figure 4 illustrates these points.

A potential difficulty in convective formulations is the tracking of boundaries. In the present case, since a round cylinder and a flat plate are considered, the boundaries are stationary and this is not a problem. However, numerical problems due to convective effects will require attention, as elaborated in following sections.

3 Thermomechanical problem

In the present section, the ALE-formulation of the thermomechanically coupled boundary value problem (assuming isotropic, homogeneous and thermoelastic materials) is presented. For a more detailed derivation, cf. Draganis et al. [8].

In terms of the ALE description, the momentum balance equation takes the form¹

$$\begin{aligned} \hat{\rho} \left[\ddot{\hat{\mathbf{X}}} + d_{tt} \hat{\mathbf{u}} + 2 \left[(d_t \hat{\mathbf{u}}) \otimes \hat{\nabla} \right] \cdot \bar{\mathbf{v}} + \hat{\mathbf{F}} \cdot (D_t \bar{\mathbf{v}}) + \right. \\ \left. \hat{\mathbf{G}} : (\bar{\mathbf{v}} \otimes \bar{\mathbf{v}}) \right] - \hat{\mathbf{P}} \cdot \hat{\nabla} - \hat{\mathbf{B}} = 0 \quad \text{in } \hat{\Omega}, \end{aligned} \quad (3)$$

where $d_t(\cdot) := \partial(\cdot)/\partial t|_{\hat{\mathbf{X}}}$, $d_{tt}(\cdot) := \partial^2(\cdot)/\partial t^2|_{\hat{\mathbf{X}}}$ are referential time derivatives, $\hat{\mathbf{F}} := \hat{\mathbf{x}} \otimes \hat{\nabla}$, $\hat{\mathbf{G}} := \hat{\mathbf{x}} \otimes \hat{\nabla} \otimes \hat{\nabla}$, $\hat{\rho}$ is the density in $\hat{\Omega}$ and $\hat{\mathbf{B}}$ is the external body force per unit volume in $\hat{\Omega}$. Further,

$$\bar{\mathbf{v}} = D_t \hat{\mathbf{X}} = \begin{cases} \dot{\mathbf{R}} \cdot \mathbf{R}^T \cdot (\hat{\mathbf{X}} - \mathbf{X}_0) & \text{for } \hat{\mathbf{X}} \in \hat{\Omega}^c \\ -\dot{\bar{\mathbf{X}}} & \text{for } \hat{\mathbf{X}} \in \hat{\Omega}^p \end{cases} \quad (4)$$

is the convective velocity. Note that due to the nature of the rotation tensor, $\hat{\nabla} \cdot \bar{\mathbf{v}} = 0$. Finally, $\hat{\mathbf{P}} = \mathbf{P} \cdot \hat{\mathbf{f}}^T$ is the push-forward of the first Piola–Kirchhoff stress tensor to $\hat{\Omega}$.

For a thermoelastic, isotropic material, it can be shown that $\hat{\mathbf{P}} = \mathbf{P}(\hat{\mathbf{F}}, \theta)$ [8], where $\mathbf{P}(\mathbf{F}, \theta)$ is the original constitutive relation in the material reference frame. This means that $\hat{\mathbf{P}}$ can be linearized for small strains ($\hat{\mathbf{F}} \approx \mathbf{I}$) and small temperature fluctuations ($\theta \approx \theta^{\text{ref}}$) using the original constitutive model, i.e.:

$$\hat{\mathbf{P}} = \mathbf{E} : \hat{\mathbf{H}} - 3K\alpha\bar{\theta}\mathbf{I}, \quad (5)$$

where the isotropic tensor of elasticity $\mathbf{E} = \frac{\partial \mathbf{P}}{\partial \hat{\mathbf{H}}} = 2G\mathbf{I}_{\text{dev}}^{\text{sym}} + K\mathbf{I} \otimes \mathbf{I}$ (where G is the shear modulus and K is the bulk modulus) was introduced. Furthermore, $\hat{\mathbf{H}} = \hat{\mathbf{F}} - \mathbf{I}$ is the displacement gradient, α is the thermal expansion coefficient, and $\bar{\theta} = \theta - \theta^{\text{ref}}$ is the excess temperature with respect to the reference θ^{ref} .

The boundary conditions can in the ALE framework be phrased as

$$\begin{cases} \hat{\mathbf{T}}^{\text{TOT}} + \hat{\rho}(\hat{\mathbf{H}} \cdot \bar{\mathbf{v}})(\bar{\mathbf{v}} \cdot \hat{\mathbf{N}}) = \hat{\mathbf{T}}_P & \text{on } \hat{\Gamma}_{R_u} \\ \hat{\mathbf{u}} = \hat{\mathbf{u}}_P & \text{on } \hat{\Gamma}_{D_u} \end{cases}, \quad (6)$$

where $\hat{\mathbf{T}}^{\text{TOT}}$ in the Robin-type boundary condition (6a) is the natural boundary traction obtained via integration by parts in the weak form [8]. Further, $\hat{\mathbf{T}}$ is the intrinsic (physical) traction, $\hat{\mathbf{N}}$ is the outward normal of $\hat{\Omega}$, and the subscript P represents prescribed quantities.

¹ \otimes denotes the dyadic (open) product.

In terms of the ALE description, the energy balance equation takes the form

$$(\theta^{\text{ref}} + \bar{\theta})\hat{\beta} : \left[d_t \hat{\mathbf{H}} + (\hat{\mathbf{F}} \cdot \bar{\mathbf{v}}) \otimes \hat{\nabla} \right] + \hat{\rho}c \left(\hat{\nabla} \bar{\theta} \cdot \bar{\mathbf{v}} + d_t \bar{\theta} \right) + \hat{\mathbf{q}} \cdot \hat{\nabla} - \hat{r} = 0 \text{ in } \hat{\Omega}, \quad (7)$$

where c is the (mass-) specific heat capacity and \hat{r} is the external heat power per unit volume in $\hat{\Omega}$. Further, $\hat{\beta} = \beta \cdot \hat{\mathbf{f}}^T$ and $\hat{\mathbf{q}} = \hat{\mathbf{f}} \cdot \mathbf{q}$ (where β is the deformation-induced heat source and \mathbf{q} is the heat flux) were introduced. For a thermoelastic, isotropic material, it can be shown that $\hat{\beta} = \beta(\hat{\mathbf{F}}, \theta)$ [8], where $\beta(\mathbf{F}, \theta)$ is the original constitutive relation in the material reference frame.

Linearizing the energy balance equation (7) for small strains and small temperature fluctuations and assuming isotropic materials gives

$$3K\alpha\theta^{\text{ref}}(\mathbf{I} : d_t \hat{\mathbf{H}} + (\hat{\mathbf{H}} \cdot \bar{\mathbf{v}}) \cdot \hat{\nabla}) + \hat{\rho}c \left(\hat{\nabla} \bar{\theta} \cdot \bar{\mathbf{v}} + d_t \bar{\theta} \right) + \hat{\mathbf{q}} \cdot \hat{\nabla} - \hat{r} = 0 \text{ in } \hat{\Omega}, \quad (8)$$

where it was used that $\bar{\mathbf{v}}$ is divergence free. The linear Fourier's law is henceforth adopted, whereby

$$\hat{\mathbf{q}} = -k \hat{\nabla} \bar{\theta}, \quad (9)$$

where k is the constant heat conductivity.

The boundary conditions can in the ALE framework be phrased as

$$\begin{cases} \hat{q}_{\hat{N}}^{\text{TOT}} - \hat{\rho}c\bar{\theta}(\bar{\mathbf{v}} \cdot \hat{N}) = \hat{q}_{\hat{N},P} & \text{on } \hat{\Gamma}_{R_\theta} \\ \bar{\theta} = \hat{\theta}_P & \text{on } \hat{\Gamma}_{D_\theta} \end{cases}, \quad (10)$$

where $\hat{q}_{\hat{N}}^{\text{TOT}}$ in the Robin-type boundary condition (10a) is the natural boundary flux obtained via integration by parts in the weak form [8]. Further, $\hat{q}_{\hat{N}}$ is the intrinsic (physical) heat flux, and the subscript P represents prescribed quantities.

If stationary rolling conditions are assumed, all referential time derivatives (d_t , d_{tt}) as well as $\ddot{\mathbf{X}}$ are zero, resulting in a time-independent problem involving the strong form

$$\hat{\rho} \left[\hat{\mathbf{F}} \cdot (D_t \bar{\mathbf{v}}) + \hat{\mathbf{G}} : (\bar{\mathbf{v}} \otimes \bar{\mathbf{v}}) \right] - \hat{\mathbf{P}} \cdot \hat{\nabla} - \hat{\mathbf{B}} = 0, \quad (11)$$

$$3K\alpha\theta^{\text{ref}}(\hat{\mathbf{H}} \cdot \bar{\mathbf{v}}) \cdot \hat{\nabla} + \hat{\rho}c \hat{\nabla} \bar{\theta} \cdot \bar{\mathbf{v}} + \hat{\mathbf{q}} \cdot \hat{\nabla} - \hat{r} = 0.$$

It is clear from (5) that $\hat{\mathbf{P}}$ is temperature dependent, due to the influence of thermal expansion. This constitutes the influence of the temperature field on the momentum balance equation. Furthermore, the deformation-dependent terms in the energy balance equation represent the Gough-Joule effect: reversible heating/cooling of the material resulting from a nonzero strain rate [12]. This effect is negligible for thermoelastic metals [13], and will therefore not be modelled in the following numerical simulations.

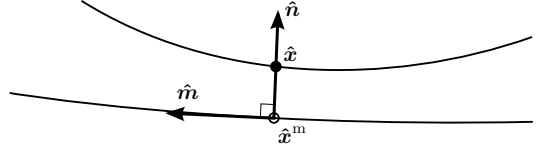


Figure 2. A point on the slave surface and its projection on the master surface, along with relevant unit vectors.

4 Contact formulation

The mechanical and thermal components of the employed contact formulation are presented below in the context of the ALE description. Contact interface laws are kept simple in the interest of clarity. However, it is emphasized that the computational framework has been constructed with modularity and extensibility in mind. The implementation of more complex contact laws would therefore be straightforward. Much of the presentation relies on concepts described in Wriggers [14].

4.1 Mechanical contact formulation

As a point $\hat{\mathbf{x}}$ on the *slave* surface (here chosen as the cylinder) comes into contact with the *master* surface (the plate), its projection point $\hat{\mathbf{x}}^m(\hat{\mathbf{x}})$ on the master surface, as well as the associated normal ($\hat{\mathbf{n}}$) and tangential ($\hat{\mathbf{m}}$) vectors, can be identified (see Figure 2). The gap function corresponding to the points $\hat{\mathbf{x}}$ and $\hat{\mathbf{x}}^m$, or their respective undeformed counterparts $\hat{\mathbf{X}}$ and $\hat{\mathbf{X}}^m(\hat{\mathbf{X}})$, can then be computed as

$$g = (\hat{\mathbf{x}} - \hat{\mathbf{x}}^m) \cdot \hat{\mathbf{n}} = (\hat{\varphi}(\hat{\mathbf{X}}) - \hat{\varphi}(\hat{\mathbf{X}}^m(\hat{\mathbf{X}}))) \cdot \hat{\mathbf{n}}. \quad (12)$$

A standard penalty method is employed for the formulation of normal mechanical contact. This involves applying a penalty traction $t_n \hat{\mathbf{n}}$ at each point $\hat{\mathbf{x}} \in \hat{\Gamma}_c^s$, where $\hat{\Gamma}_c^s$ is the set of points on the slave surface penetrating the master surface, i.e. for which $g < 0$. An opposing force is imposed at $\hat{\mathbf{x}}^m(\hat{\mathbf{x}})$. Here,

$$t_n = -\epsilon g, \quad (13)$$

where ϵ is the penalty stiffness. In theory, $\lim_{\epsilon \rightarrow \infty} g = 0$. In a practical numerical implementation, an increased penalty stiffness ϵ leads to a decreased absolute value of the gap function, but an excessive increase leads to ill-conditioning of the discretized equation system. ϵ is typically taken as mesh-dependent, scaling inversely with some measure of the mesh size (thus having a higher value in more refined regions) [14]. In the current implementation, $\epsilon = \epsilon_n/h$ is employed, where ϵ_n is a constant and h is a local measure of mesh size.

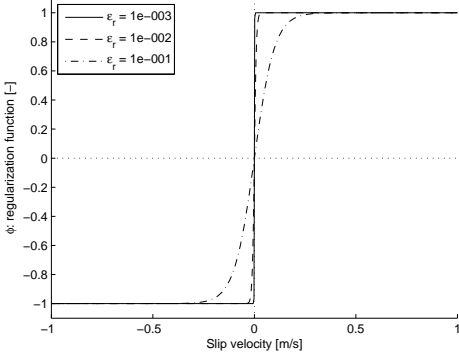


Figure 3. Regularized version of Coulomb's friction law.

Note that this choice results in the desired property $\lim_{h \rightarrow 0} \epsilon = \infty \Rightarrow \lim_{h \rightarrow 0} g = 0$.

Frictional interaction between the surfaces results in a force $t_m \hat{\mathbf{m}}$ being applied at each point $\hat{\mathbf{x}} \in \hat{\Gamma}_c^s$. An opposing force is imposed at $\hat{\mathbf{x}}^m(\hat{\mathbf{x}})$. Here,

$$t_m = -\mu |t_n| \phi(\dot{s}), \quad (14)$$

where μ is the coefficient of friction and

$$\begin{aligned} \dot{s} &= [D_t \hat{\mathbf{x}} - D_t \hat{\mathbf{x}}^m] \cdot \hat{\mathbf{m}} \\ &= [D_t \hat{\varphi}(\hat{\mathbf{X}}^m) - D_t \hat{\varphi}(\hat{\mathbf{X}})] \cdot \hat{\mathbf{m}}(\hat{\mathbf{X}}) \end{aligned} \quad (15)$$

is the slip velocity. For stationary contact, one obtains

$$\dot{s} = [\hat{\mathbf{F}}(\hat{\mathbf{X}}) \cdot \bar{\mathbf{v}}(\hat{\mathbf{X}}) - \hat{\mathbf{F}}(\hat{\mathbf{X}}^m) \cdot \bar{\mathbf{v}}(\hat{\mathbf{X}}^m)] \cdot \hat{\mathbf{m}}(\hat{\mathbf{X}}).$$

Further, $\phi(\dot{s})$ is a function of the same sign as \dot{s} , satisfying $|\phi| \leq 1$. In the current implementation, a regularized version of Coulomb's law is used, so that

$$\phi(\dot{s}) = \tanh(\dot{s}/\epsilon_r), \quad (16)$$

(see Figure 3) where ϵ_r [m/s] is a regularization parameter. Note that in this case, the friction force is unambiguously determined from the slip velocity, and that Coulomb's friction law (which is equivalent to a Lagrange multiplier method) is obtained in the limit $\epsilon_r \rightarrow 0$.

ϵ_r should be chosen in the range $\epsilon_r^{\text{conv}} \leq \epsilon_r \leq \epsilon_r^{\text{num}}$, where ϵ_r^{conv} represents the limit below which the contact iterations do not converge and ϵ_r^{num} the limit above which computed results exhibit a dependency on ϵ_r . These limits depend on (increase with) the overall magnitude of the slip velocity in the contact region, and must be obtained via a convergence study. Note that ϵ_r^{conv} can be decreased by computational strategies aimed at facilitating convergence (see Section 5.3). These are important, since it otherwise might occur that $\epsilon_r^{\text{conv}} > \epsilon_r^{\text{num}}$.

4.2 Thermal contact formulation

The formulation of thermal conduction in the contact region is derived in a manner analogous to the case of normal mechanical contact. A ‘‘penalty’’ heat flux of magnitude $k_c \Delta\theta$ is imposed across the contact interface. Here, k_c is the contact conductivity and

$$\Delta\theta(\hat{\mathbf{X}}) = \theta(\hat{\mathbf{X}}) - \theta(\hat{\mathbf{X}}^m(\hat{\mathbf{X}})) = \bar{\theta}(\hat{\mathbf{X}}) - \bar{\theta}(\hat{\mathbf{X}}^m(\hat{\mathbf{X}})) \quad (17)$$

is the temperature difference. Perfect thermal contact is represented by $\lim_{k_c \rightarrow \infty} \Delta\theta = 0$. That is, the contact conductivity k_c would play a role similar to that of the penalty stiffness ϵ in the mechanical normal contact formulation. However, k_c should here in general be interpreted as a physical conductivity pertaining to the surface properties at the contact. Although here taken as constant in the interests of simplicity, this parameter would in a more realistic model exhibit a complex dependence on e.g. microgeometry, third body characteristics and contact pressure. Further, the phenomenon of interfacial heat conduction is strongly dependent on the relative velocity of the contacting bodies. However, since this dependency is inherent in the convective ALE formulation of the energy balance equation (see Section 6.3.2 and 6.3.3 for a more detailed discussion), there is no need to have k_c depend on the velocity.

Frictional interaction between surfaces generates a frictional power

$$w_f = |t_m \dot{s}| = -t_m \dot{s} = \mu |t_n| \phi(\dot{s}) \dot{s}, \quad (18)$$

where it was used that $t_m \dot{s} < 0$. It is assumed that a portion w_f' of this heat is transferred into the contacting bodies. This amount is governed by the frictional heat transfer ratio γ_f , so that $w_f' = \gamma_f w_f$. The parameters α_f^s and α_f^m ($\alpha_f^s + \alpha_f^m = 1$) govern the heat partitioning, so that the heat fluxes due to the generated heat are

$$\begin{aligned} q_{n,f}^s(\hat{\mathbf{X}}) &= \begin{cases} -\alpha_f^s w_f' & \hat{\mathbf{X}} \in \hat{\Gamma}_c^s \\ 0 & \hat{\mathbf{X}} \notin \hat{\Gamma}_c^s \end{cases}, \\ q_{n,f}^m(\hat{\mathbf{X}}^m(\hat{\mathbf{X}})) &= \begin{cases} -\alpha_f^m w_f' & \hat{\mathbf{X}} \in \hat{\Gamma}_c^s \\ 0 & \hat{\mathbf{X}} \notin \hat{\Gamma}_c^s \end{cases}, \end{aligned} \quad (19)$$

where $w_f' = \gamma_f \mu |t_n| \phi(\dot{s}) \dot{s}$. In the subsequent numerical simulations, the heat partitioning parameters are simply chosen as $\alpha_f^s = \alpha_f^m = 1/2$. Note that there is no need to include heuristic time-dependencies in the parameters α_f^s and α_f^m in order to capture the dependence of heat partitioning on the relative velocity of the contacting bodies. Again, this is due to the fact that this effect is inherent in the employed ALE formulation.

5 Solution method

5.1 Discretization

The finite element formulation of the problem is implemented in MATLAB. The element type used is a triangular element with one/two degrees of freedom per node in the thermal/mechanical problems, respectively. The approximation for both displacements and temperatures is piecewise linear in the plate and piecewise quadratic in the cylinder. Note that the discrepancy in element order between cylinder and plate has implications for the contact formulation, which is further discussed in Section 5.3.

The employed mesh is shown in Figure 4. The mesh of the cylinder is constructed from a coarse basic mesh which is refined according to the following scheme: successive refinement in a series of gradually smaller domains centered at the point of initial contact \rightarrow global refinements (2 are here used) \rightarrow refinement of the largest elements along the periphery. After that, all nodes are remapped radially so that the outer nodes describe a circle. At this point, the centroid of the discretized domain is inevitably slightly displaced compared to that of the ideal annular domain. This causes considerable errors in the contact computation [8]. To compensate, the inner boundary is rigidly moved so that the position of the centroid of the discretized domain is corrected (thus slightly modifying the geometry). The positions of the inner nodes of the mesh are then determined by linear elastic equilibrium.

The plate domain mesh is constructed by starting from a structured mesh and refining it locally in a rectangular area centered at the point of initial contact. This area extends a distance $2d_c$ horizontally and d_c vertically, where d_c is an analytical prediction (using Hertz theory) of the contact patch width. The minimum allowed size for an element in the final mesh of the plate is 1.5 times the size of the largest element in the most refined region of the cylinder mesh.

All mesh refinements are performed according to Rivara's longest-edge refinement technique [15]. The final mesh contains 8017 elements and 12608 nodes.

5.2 Element choice and numerical stabilization

Previous studies [7] indicated that, at least for rolling speeds up to the order of a few hundred km/h, no numerical stability problems arise related to the discretized momentum balance equation for the present implementation. By contrast, various numerical problems have been found to have a prominent influence for the discretized energy balance equation, even for very modest rolling speeds [8]. The numerical problems are manifested as

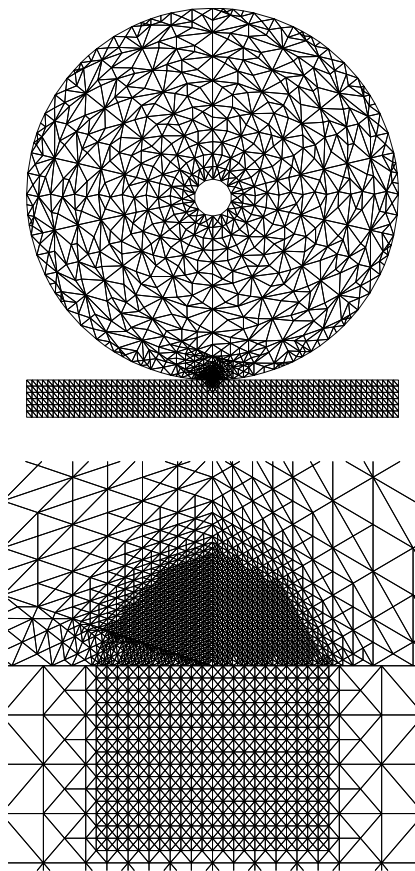


Figure 4. The employed finite element mesh, with a zoomed-in view of the refined contact region.

node-to-node oscillations in the plate domain and oscillations together with energy dissipation in the cylinder domain.

In order to address these problems, two numerical stabilization methods are employed: The Streamline-Upwind Petrov–Galerkin (SUPG) method [10, 16] is used for the plate domain, and a quasi residual-free bubble approach [17, 18], which is a variant of the scheme presented in Brezzi et al. [19], is used for the cylinder domain. The reader is referred to Draganis et al. [8] for a detailed description of the latter method and an investigation of its performance.

5.3 Contact iterations

A linear–linear contact element is used in the cylinder–plate interface, regardless of the element orders used to discretize the two domains. This means that with regard to the employed triangular elements, contact forces are assembled exclusively to corner degrees of freedom.

The addition of the nonlinear contact contributions to the (otherwise linear) FE formulation of the thermomechanical boundary value problem leads to a nonlinear equation system. This system is solved monolithically by the Newton method, employing a contact iteration scheme following Wriggers [14].

Obtaining convergence in the frictional contact iterations is difficult, especially when slip velocities are high. To address this problem, a velocity stepping scheme is implemented in which convective velocities in cylinder and plate are gradually increased, the solution for one step serving as a start guess for the next. The start guess used for the first velocity-stepping iteration is the solution to the corresponding frictionless contact problem (which is far less susceptible to convergence problems). The start guess used here is in turn obtained from a simplified problem employing appropriate Hertzian contact pressure distributions as contact loads.

6 Numerical examples

6.1 Numerical model

The following numerical examples are based on a 2D (plane strain) model of a hollow cylinder rolling on a plate. The model features an isotropic, homogeneous, linear elastic material. A constant translational velocity of the cylinder centre (relative to a fixed coordinate system) is assumed, while a vertical force is applied on the inner boundary (hub) of the cylinder. In order to facilitate comparisons to analytical solutions, gravitational loads on the bodies are not included (inertial effects are modelled, however). The base of the plate is fixed in all degrees of freedom and the cylinder hub is fixed in the horizontal direction (in $\hat{\Omega}$). All other boundaries are free.

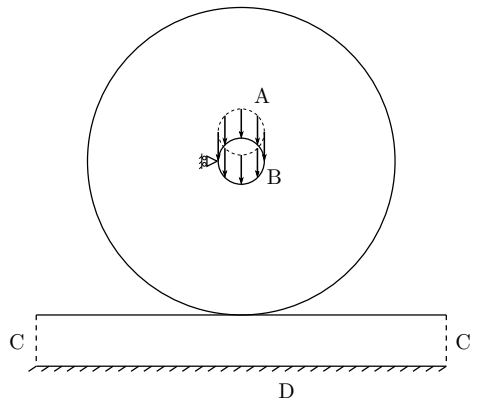


Figure 5. Schematic illustration of the thermomechanical model. A: applied mechanical load, B: cylinder hub (fixed in horizontal direction, fixed temperature), C: artificial plate domain ends (fixed temperature), D: plate base (fixed in all displacement degrees of freedom).

The temperature is prescribed (to the reference temperature) along the cylinder hub and at the plate ends, while all other boundaries (not in contact) are thermally insulated. Figure 5 shows a schematic illustration of the geometry, boundary conditions and loads of the employed model.

A reference parameter setup (used in the following simulations unless otherwise indicated) is now defined. Material parameters in both bodies are: Young’s modulus $E = 200$ GPa, Poisson’s ratio $\nu = 0.3$, specific heat capacity $c = 460$ Jkg⁻¹K⁻¹, thermal conductivity $k = 45$ Wm⁻¹K⁻¹, thermal expansion coefficient $\alpha = 4.8 \cdot 10^{-6}$ K⁻¹ and density $\rho = 8 \cdot 10^3$ kgm⁻³. Outer and inner radii of the cylinder are $r_o = 50$ cm and $r_i = 5$ cm, respectively. The height of the plate is $h = 0.1$ m and the width of the modeled plate domain is chosen as $b = 1$ m. The contact conductivity is $k_c = 10^7$ Wm⁻²K⁻¹, the frictional heat transfer ratio is $\gamma_f = 10\%$ and the penalty stiffness is $\epsilon_n = 5$ TN/m. The reference (environmental) temperature is $\theta^{\text{ref}} = 293$ K and the mechanical load is $P = 10$ kN/m.

The (absolute) translational velocity of the cylinder center is chosen as $V_T = 50$ km/h. The rotational velocity of the cylinder is chosen independently, whereby the creepage [3]

$$\xi := 2(V_T - V_C)/(V_T + V_C), \quad (20)$$

is controlled. Here, V_C is the circumferential convective velocity at the outer boundary. Unless otherwise stated, the creepage is chosen as $\xi = -5 \cdot 10^{-5}$.

The following presentation includes studies of the mean excess temperature $\bar{\theta}_m$, which for an arbitrary do-

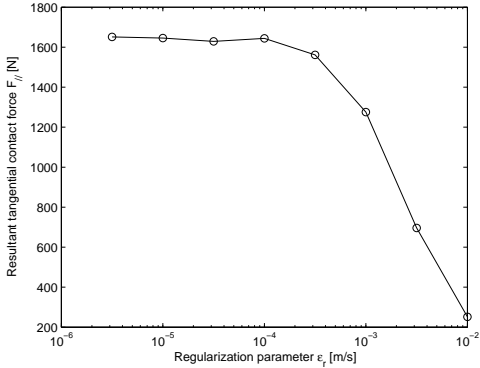


Figure 6. Resultant tangential contact force $F_{//}$ vs. the frictional regularization parameter ϵ_r .

main \mathcal{V}_0 (of volume V_0) is defined as

$$\bar{\theta}_m = \frac{1}{V_0} \int_{\mathcal{V}_0} \bar{\theta} dV. \quad (21)$$

In the following, \mathcal{V}_0 is taken as the cylinder domain and the plate domain, alternatively.

6.2 Convergence study for ϵ_r

Figure 6 shows the dependence on ϵ_r of the resultant tangential contact force $F_{//}$ for given values of V_T and ξ . Based on this data, it can be deduced that $\epsilon_r^{\text{num}} \approx 10^{-4}$. $\epsilon_r = \sqrt{10} \cdot 10^{-5}$ will henceforth be used.

6.3 Rolling/sliding contact simulations

6.3.1 Contact stress distributions

Figure 7 shows the ratio of the resultant tangential contact force $F_{//}$ and the limiting friction force μF_{\perp} (where F_{\perp} is the resultant normal contact force) versus the creepage ξ . An analytical curve obtained from Carter's force-creepage law [20, 3], valid for purely mechanical cylinder-plate rolling contact, is superimposed. Figures 8–10 show the normal and tangential contact stress distributions for the creepages $\xi = -5 \cdot 10^{-5}$, $\xi = -1.25 \cdot 10^{-4}$ and $\xi = -2.5 \cdot 10^{-4}$, respectively. Note that the last creepage value corresponds to full slip (cf. Figure 7). Analytical curves obtained from Carter-Hertz theory [2] are superimposed. Additionally, Figure 11 shows slip velocity profiles across the contact zone for the three cases studied.

Due to local deformations in the contact region, the numerical solution deviates from the idealized Carter-Hertz solution, especially near the point of transition between the stick- and slip regions (see Figures 11–14).

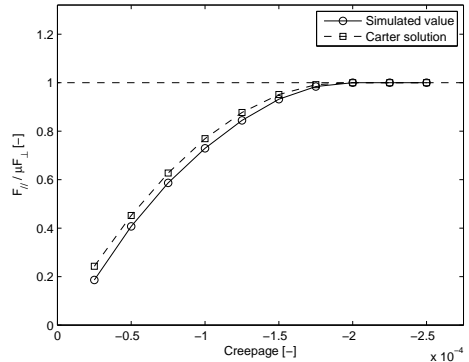


Figure 7. Force-creepage curve.

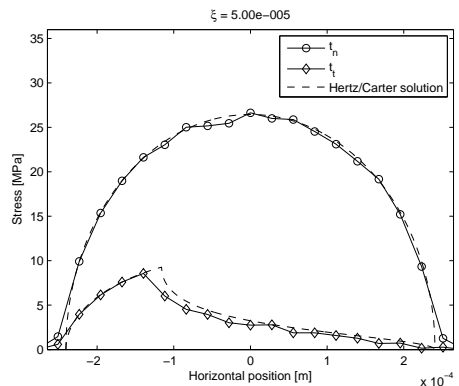


Figure 8. Normal and tangential contact stress distributions. Simulated (solid lines) and Hertz/Carter solutions (dashed lines). $\xi = -5 \cdot 10^{-5}$.

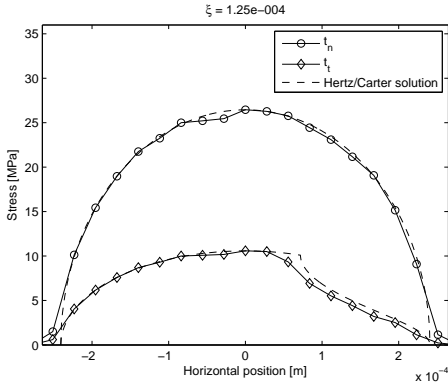


Figure 9. Normal and tangential contact stress distributions. Simulated (solid lines) and Hertz/Carter solutions (dashed lines). $\xi = -1.25 \cdot 10^{-4}$.

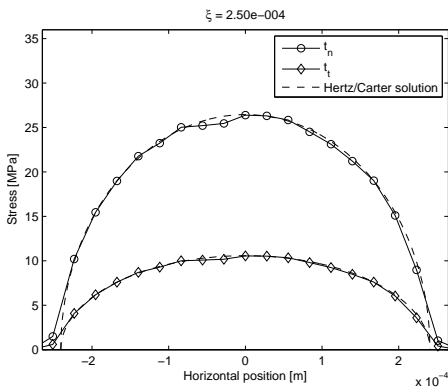


Figure 10. Normal and tangential contact stress distributions. Simulated (solid lines) and Hertz/Carter solutions (dashed lines). $\xi = -2.5 \cdot 10^{-4}$.

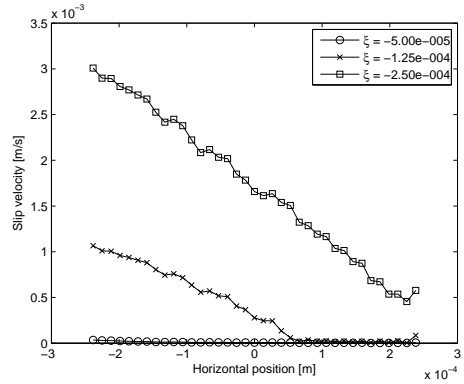


Figure 11. Slip velocity profiles for three rolling contact simulations.

Further, it is noted that since the controlled quantity is the creepage (rather than the driving moment or horizontal force), there is a discrepancy also in the resultant tangential force.

6.3.2 Temperature distributions

Figure 12 shows the temperature distribution for the case $\xi = -5 \cdot 10^{-5}$ in two regions on either side of the contact interface, each having the dimensions $1.5 \text{ mm} \times 0.3 \text{ mm}$. In each case, the edges of the contact zone are highlighted by vertical gray marks. As seen in Figures 7 and 8, the employed value of ξ corresponds to a situation of mixed stick/slip. The frictional interaction between the surfaces gives rise to heat generation in the slip region (see Section 4.2), i.e. the segment near the left (trailing) edge of the contact zone roughly corresponding to the interval $-0.25 \text{ mm} < \tilde{X} < -0.14 \text{ mm}$ (cf. Figure 8).

Another thermal phenomenon affecting the temperature distribution shown in Figure 12 is the convection inherent to the employed ALE formulation, resulting in a temperature distribution skewed in the direction of the convective flow. Note in particular the displacement of the region of the frictionally induced temperature peak from the slip region (whose location in the contact region can be seen in Figure 8). Interfacial heat transfer (see Section 4.2) further contributes to a redistribution of temperature between cylinder and plate. As mentioned in Section 3, the Gough–Joule effect – if modelled – would here have a negligible influence on the temperature field.

The mean temperatures in cylinder and plate for the case studied above are $2.26 \cdot 10^{-6} \text{ K}$ and $4.45 \cdot 10^{-9} \text{ K}$, respectively. To an extent, the large difference in magnitude is due to convective effects: heat is transported out of the considered plate domain while cold material

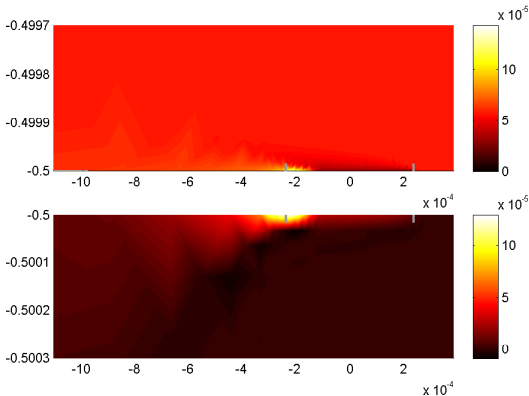


Figure 12. Patch plot of the temperature distribution near the contact interface [K]. Zoomed-in view: each plot window has the dimensions $1.5 \text{ mm} \times 0.3 \text{ mm}$. The gray marks highlight the edges of the contact region. $\xi = -5 \cdot 10^{-5}$.

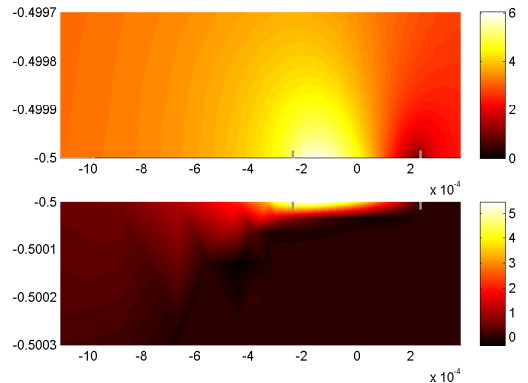


Figure 13. Patch plot of the temperature distribution near the contact interface [K]. Zoomed-in view: each plot window has the dimensions $1.5 \text{ mm} \times 0.3 \text{ mm}$. The gray marks highlight the edges of the contact region. Locked cylinder (pure sliding: $\xi = 2$).

is transported into it. Note however that these quantities are not readily comparable, due to the inherent arbitrariness of the mean temperature measure (21) and the volume over which it is taken.

Figure 13 shows the temperature distribution for the case where the rotational motion of the cylinder is locked ($\xi = 2$) – which means that the convective velocity in the cylinder domain is zero. A comparison between Figures 12 and 13 predictably shows that pure sliding contact results in vastly higher temperatures overall. This is due to higher slip velocities causing an increased frictional heat generation. Another contributing factor is the lack of convection in the cylinder, which means that diffusion and interfacial heat transfer are the only mechanisms transporting heat away from the region in the cylinder closest to the contact. The reason for the asymmetrical temperature distribution in the cylinder (despite the lack of convection in that domain) is the interfacial heat transfer in conjunction with the fact that the temperature distribution in the plate is asymmetric due to convective effects.

6.3.3 Influence of operational parameters

Figure 14 shows mean temperatures in the cylinder versus translational velocity V_T for four different values of the creepage ξ (including the case of pure sliding: $\xi = 2$). In each of these cases, an increased velocity V_T leads to higher slip velocities and thus an increased frictional heat generation. This in turn leads to higher temperatures, both globally (see Figure 14) and locally in the contact region. However, since the convective velocity in the plate also increases (with V_T), so does the interfacial temperature difference and, in turn, the heat conduction

through the contact interface. As a result, the increase of temperature in the cylinder is slowed, as seen in the figure. A similar behaviour was observed in Vernersson and Lundén [21], where a numerical model of wheel-rail heat transfer was used to investigate the influence of rail chill on tread braked railway wheels.

Figure 15 shows the mean temperatures in cylinder and plate plotted against the contact conductivity k_c , for a rolling contact simulation featuring $\xi = -5 \cdot 10^{-5}$. An increased contact conductivity facilitates redistribution of temperature between cylinder and plate, hence the saturation effect apparent in the figure – which is in qualitative agreement with studies performed in Vernersson and Lundén [21].

7 Concluding remarks

A theoretical and computational framework governing thermomechanically coupled, stationary rolling/sliding contact based on an ALE kinematical description is presented. The ALE formulation allows for linearization of the mechanical response, localized mesh refinement and a compact plate domain. It further enables formulation of the stationary rolling contact problem as time-independent and the contact interface law as velocity-independent. Numerical examples featuring frictional rolling/sliding contact show the model to be in agreement with analytical solutions and able to capture stick/slip behaviour. Further, the influence of convective effects on the temperature distribution is illustrated (in the presence of frictional heat generation), including the effect of convective cooling of the cylinder due to the contact with the plate.

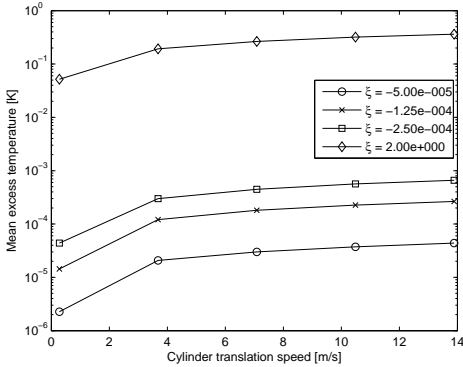


Figure 14. Mean temperatures in cylinder and plate versus cylinder translation speed for varying values of ξ .

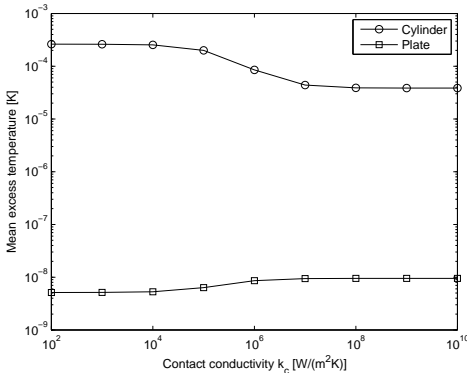


Figure 15. Mean temperatures in cylinder and plate versus contact conductivity for rolling contact featuring $\xi = -5 \cdot 10^{-5}$.

It was shown that normal/tangential contact pressures, temperatures and slip velocities are computable at a local level. Thus, quantities derived from these are readily available in postprocessing. For instance, the local wear rate could be computed (e.g. using Archard’s law [22]) and interpolated across the contact zone, using knowledge of contact pressures, slip velocities, contact interface constitutive data and possibly temperatures.

Upcoming work will be towards implementing support for transient simulations. This would allow for high-resolution investigation of non-stationary, thermomechanical rolling/sliding contact situations, e.g. strongly non-Hertzian contact conditions and transient braking simulations.

Acknowledgement

The project is a part of the ongoing activities in the National Centre of Excellence CHARMEC (www.chalmers.se/charmec).

References

- [1] S. P. Timoshenko and J. N. Goodier. *Theory of elasticity*. Engineering societies monographs. McGraw-Hill, 1951.
- [2] K. L. Johnson. *Contact mechanics*. Cambridge University Press, 1987. ISBN: 9780521347969.
- [3] J. J. Kalker. “Wheel–rail rolling contact theory”. *Wear* **144** (1991), 243–261.
- [4] A. Johansson et al. “Simulation of wheel–rail contact and damage in switches & crossings”. *Wear* **271.1–2** (May 2011), 472–481. ISSN: 00431648. DOI: 10.1016/j.wear.2010.10.014.
- [5] R. Enblom and M. Berg. “Proposed procedure and trial simulation of rail profile evolution due to uniform wear”. *Proceedings of the Institution of Mechanical Engineers, Part F: Journal of Rail and Rapid Transit* **222.1** (Mar. 2008), 15–25. ISSN: 0954-4097. DOI: 10.1243/09544097JRRT173.
- [6] J. Tunna, J. Sinclair, and J. Perez. “A review of wheel wear and rolling contact fatigue”. *Proceedings of the Institution of Mechanical Engineers, Part F: Journal of Rail and Rapid Transit* **221.2** (Jan. 2007), 271–289. ISSN: 0954-4097. DOI: 10.1243/09544097JRRT72.
- [7] A. Draganis, F. Larsson, and A. Ekberg. “Numerical evaluation of the transient response due to non-smooth rolling contact using an arbitrary Lagrangian–Eulerian formulation”. *Proceedings of the Institution of Mechanical Engineers, Part J: Journal of Engineering Tribology* **226.1** (2012), 36–45. DOI: 10.1177/1350650111422015.

- [8] A. Draganis, F. Larsson, and A. Ekberg. “Finite element analysis of transient thermomechanical rolling contact using an efficient arbitrary Lagrangian–Eulerian description”. *Computational Mechanics* **54.2** (2014), 389–405. ISSN: 0178-7675. DOI: 10.1007/s00466-014-0992-6.
- [9] U. Nackenhorst. “The ALE-formulation of bodies in rolling contact: Theoretical foundations and finite element approach”. *Computer Methods in Applied Mechanics and Engineering* **193** (2004), 4299–4322. DOI: 10.1016/j.cma.2004.01.033.
- [10] J. Donéa and A. Huerta. *Finite element methods for flow problems*. Wiley, 2003. ISBN: 9780471496663.
- [11] A. Suwannachit and U. Nackenhorst. “A novel approach for thermomechanical analysis of stationary rolling tires within an ALE-kinematic framework”. *Tire Science and Technology* **41.3** (2013), 174–195.
- [12] B. Schweizer and J. Wauer. “Atomistic explanation of the Gough-Joule-effect”. *The European Physical Journal B - Condensed Matter and Complex Systems* **23.3** (2001), 383–390. ISSN: 1434-6028. DOI: 10.1007/s100510170058.
- [13] N. S. Ottosen and M. Ristinmaa. *The mechanics of constitutive modeling*. Elsevier, 2005. ISBN: 9780080446066.
- [14] P. Wriggers. *Computational contact mechanics*. Springer, 2006. ISBN: 9783540326083.
- [15] M. C. Rivara. “Algorithms for refining triangular grids suitable for adaptive and multigrid techniques”. *International Journal for Numerical Methods in Engineering* **20.4** (1984), 745–756. ISSN: 1097-0207. DOI: 10.1002/nme.1620200412.
- [16] R. Codina, E. Onate, and M. Cervera. “The intrinsic time for the streamline upwind/Petrov-Galerkin formulation using quadratic elements”. *Computer Methods in Applied Mechanics and Engineering* **94.2** (1992), 239–262. ISSN: 0045-7825. DOI: 10.1016/0045-7825(92)90149-E.
- [17] F. Brezzi et al. “A relationship between stabilized finite element methods and the Galerkin method with bubble functions”. *Computer Methods in Applied Mechanics and Engineering* **96.1** (1992), 117–129. ISSN: 0045-7825. DOI: 10.1016/0045-7825(92)90102-P.
- [18] C. Baiocchi, F. Brezzi, and L. P. Franca. “Virtual bubbles and Galerkin-least-squares type methods (Ga.L.S.)” *Computer Methods in Applied Mechanics and Engineering* **105.1** (1993), 125–141. ISSN: 0045-7825. DOI: 10.1016/0045-7825(93)90119-I.
- [19] F. Brezzi, D. Marini, and A. Russo. “Applications of the pseudo residual-free bubbles to the stabilization of convection-diffusion problems”. *Computer Methods in Applied Mechanics and Engineering* **166.1–2** (1998). Advances in Stabilized Methods in Computational Mechanics, 51–63. ISSN: 0045-7825. DOI: [http://dx.doi.org/10.1016/S0045-7825\(98\)00082-6](http://dx.doi.org/10.1016/S0045-7825(98)00082-6).
- [20] F. W. Carter. “On the action of a locomotive driving wheel”. *Proceedings of the Royal Society of London. Series A* **112.760** (1926), 151–157. DOI: 10.1098/rspa.1926.0100.
- [21] T. Vernersson and R. Lundén. “Temperatures at railway tread braking. Part 3: wheel and block temperatures and the influence of rail chill”. *Proceedings of the Institution of Mechanical Engineers, Part F: Journal of Rail and Rapid Transit* **221.4** (Jan. 2007), 443–454. ISSN: 0954-4097. DOI: 10.1243/09544097JRR91.
- [22] J. F. Archard. “Contact and rubbing of flat surfaces”. *Journal of Applied Physics* **24.8** (1953), 981–988. DOI: <http://dx.doi.org/10.1063/1.1721448>.

Paper D

Finite element modelling of transient thermomechanical rolling contact featuring mixed control of the rigid body motion

Finite element modelling of transient thermomechanical rolling contact featuring mixed control of the rigid body motion

Andreas Draganis

Department of Applied Mechanics, Chalmers University of Technology, Gothenburg, Sweden
CHARMEC, Chalmers University of Technology, Gothenburg, Sweden

Abstract

A theoretical and computational framework for the analysis of fully transient, thermomechanically coupled, frictional rolling contact based on an Arbitrary Lagrangian–Eulerian (ALE) kinematical description is presented. In particular, a computationally efficient methodology for mixed control between the ALE referential velocities and their corresponding driving forces is developed and discussed in depth. Numerical examples involving 2D cylinder–plate rolling contact are presented, covering a range of transient, thermomechanically coupled rolling contact phenomena, existing on a broad range of time scales. Here, particular points of emphasis include dynamical effects in the vicinity of the contact region, and the time scales on which mechanical and thermal mechanisms operate.

Keywords: arbitrary Lagrangian–Eulerian, rolling contact, frictional contact, thermomechanical coupling, transient analysis, finite element method

1 Introduction

Computational approaches to rolling contact problems commonly employ semi-analytical models, where analytical expressions (usually from Hertz and Carter theory [1, 2, 3]) are used in conjunction with e.g. Finite Element (FE) analysis of contacting bodies (see e.g. Xu and Jiang [4] and references therein). These approaches entail low computational costs, but are only applicable to situations in which their underlying assumptions hold. For instance, Hertz theory is based on the half-space assumption (which in turn requires the contact patch to be small relative to the radii of curvature of the contacting bodies) and is limited to smooth contact surfaces and quasistatic dynamics. Another approach to computational rolling contact analysis is represented by Kalker’s and Vollebregt’s CONTACT software [5, 6]: a versatile and robust framework which is based on the boundary element method. However, CONTACT is also based on the half-space assumption, does not support a thermo-mechanical analysis, and is limited to quasistatic dynamics.

A third option is to employ a full FE discretization of the contacting bodies. Although there are cases in this context in which a standard Lagrangian kinematical description can be used [7], an Arbitrary Lagrangian–Eulerian (ALE) kinematical description [8, 9] is a more suitable choice when large rolling distances and velocities are involved. When properly configured, such a description separates the rigid body component of the rolling motion from the deformation dependent part, and enables linearization of the mechanical response. Further-

more, the region of contact remains largely stationary throughout the rolling motion in this case, which allows for localized mesh refinement and a compact computational domain.

The use of similar relative kinematics approaches for analysis of rolling contact goes back to the eighties [10, 11, 12]. The relation between these methods and the ALE methods that saw regular use in fluid mechanics and fluid–structure interaction problems at the time was observed in Nackenhorst [13]. In a later paper by the same author, a complete mathematical formulation of mechanical rolling contact in the context of an ALE kinematical description was established [8]. Here, detailed derivations of the kinematical description, balance laws, weak forms and contact kinematics are presented in the ALE framework. The paper furthermore discusses computational advantages gained from the use of the ALE description, including the resulting time-independent description of stationary (steady-state) rolling and localized mesh refinement, but also highlights complications stemming from the associated difficulty of tracking material points. These include handling inelastic material behaviour and keeping track of relative slip distances, both of which were addressed in a subsequent paper [14]. In Suwannachit and Nackenhorst [15], the use of an ALE formulation for thermomechanically coupled stationary rolling contact was introduced. Here, a thermoviscoelastic constitutive model is employed, involving large deformations and temperature-dependent constitutive parameters.

In Draganis et al. [16], the mathematical framework for thermomechanically coupled, frictionless, transient

rolling contact was derived in the context of an ALE description. Support for tangential contact stresses and frictional heat generation was added to the contact formulation in Draganis et al. [17]. Numerical examples in the context of stationary rolling contact were here presented in a study of the thermomechanical response of the computational model.

This paper concerns thermomechanically coupled, transient, frictional rolling contact. It discusses computationally efficient strategies for analysis of problems involving variable velocities, as well as mixed control between the ALE referential convective velocities and corresponding driving forces. Numerical examples are presented, covering a range of transient, thermomechanically coupled rolling contact phenomena. Here, particular points of emphasis include dynamical effects in the vicinity of the contact region and the time scales on which mechanical and thermal mechanisms operate.

The remainder of the paper is outlined as follows: In Section 2, the kinematical description of the rolling motion is described. The thermomechanical problem and the contact formulation are presented in Sections 3 and 4, respectively. Section 5 describes implemented numerical stabilization schemes, strategies for computationally efficient analysis of problems involving variable velocities, as well as a method for mixed control between the ALE referential convective velocities and corresponding driving forces. Numerical examples involving transient, thermomechanical rolling contact phenomena are presented in Section 6. Finally, Section 7 concludes the paper with a summary and an outlook toward future work.

2 Kinematical description

The employed ALE description of cylinder–plate rolling motion [8, 16] can be described as follows: Two intermediate configurations are utilized in addition to the initial (“undeformed”) configuration, $\Omega_X \ni \mathbf{X}$, and the current (“deformed”) configuration, $\omega_X \ni \mathbf{x}$. The first intermediate configuration is denoted $\hat{\Omega} \ni \hat{\mathbf{X}}$. The map from Ω_X to $\hat{\Omega}$ accounts for a rigid body rotation of the cylinder and a pure translation of the plate. The second intermediate configuration is denoted $\hat{\omega} \ni \hat{\mathbf{x}}$. The map from $\hat{\Omega}$ to $\hat{\omega}$ accounts for the deformation of cylinder and plate. Both intermediate configurations feature a moving coordinate system that follows the cylinder center. The map from $\hat{\omega}$ to ω_X accounts for a pure translation of the system in going back to the original fixed coordinate system.

The maps between the configurations are formulated as $\hat{\mathbf{X}} = \hat{\phi}(\mathbf{X}, t)$, $\hat{\mathbf{x}} = \hat{\varphi}(\hat{\mathbf{X}}, t)$, $\mathbf{x} = \check{\phi}(\hat{\mathbf{x}}, t)$ and $\mathbf{x} = \varphi(\mathbf{X}, t)$, so that $\varphi(\mathbf{X}, t) = \hat{\phi}(\hat{\phi}(\hat{\phi}(\mathbf{X}, t), t), t)$, with corresponding deformation gradients $\hat{\mathbf{f}}$, $\hat{\mathbf{F}}$, $\check{\mathbf{f}}$ and \mathbf{F} . Figure 1 contains a schematic illustration of the employed

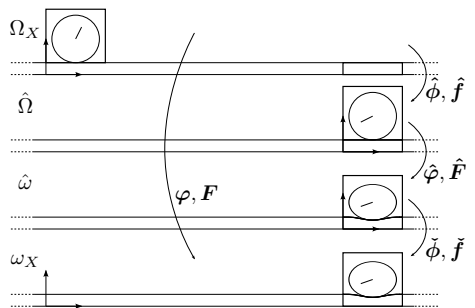


Figure 1: Illustration of configurations and maps relevant to the employed ALE description.

configurations, with their intermediary maps and deformation gradients.

The rigid body maps $\hat{\mathbf{X}} = \hat{\phi}(\mathbf{X}, t)$ and $\mathbf{x} = \check{\phi}(\hat{\mathbf{x}}, t)$ can be expressed a priori from knowledge of the translational and rotational motion of the cylinder along the plate:

$$\hat{\mathbf{X}} = \hat{\phi}(\mathbf{X}, t) = \begin{cases} \mathbf{R}(t) \cdot \mathbf{X} & \text{for } \mathbf{X} \in \Omega_X^c \\ \mathbf{X} - \bar{\mathbf{X}}(t) & \text{for } \mathbf{X} \in \Omega_X^p \end{cases} \quad (1)$$

$$\mathbf{x} = \check{\phi}(\hat{\mathbf{x}}, t) = \hat{\mathbf{x}} + \bar{\mathbf{X}}(t) \quad \text{for } \hat{\mathbf{x}} \in \hat{\omega}, \quad (2)$$

where \mathbf{R} is a rotation tensor, $\bar{\mathbf{X}}$ is the translation of the cylinder center, and the notation $(\cdot)^c$ and $(\cdot)^p$ denotes subsets of the relevant domain corresponding to the cylinder and plate domains, respectively. Above and henceforth, a coordinate system originating from the cylinder center is employed for the domains Ω_X and $\hat{\Omega}$. The Lagrangian problem of finding the map $\mathbf{x} = \varphi(\mathbf{X}, t)$ (or the displacement $\mathbf{u}(\mathbf{X}, t) = \varphi(\mathbf{X}, t) - \mathbf{X}$) is thus narrowed down to the ALE problem of finding the map $\hat{\mathbf{x}} = \hat{\varphi}(\hat{\mathbf{X}}, t)$ (or the displacement $\hat{\mathbf{u}}(\hat{\mathbf{X}}, t) = \hat{\varphi}(\hat{\mathbf{X}}, t) - \hat{\mathbf{X}}$). For small strains, the ALE displacements $\hat{\mathbf{u}}$ will be small, which is generally not the case for the standard Lagrangian displacements \mathbf{u} . Consequently, in the former case (but not the latter) it is possible to linearize the mechanical response.

Another advantage of the presented convective kinematical description is the fact that it allows for a compact computational model: only a relatively short section of the plate domain needs to be modelled, regardless of rolling distance. Further, the position (in the intermediate domains) of the contact region in both cylinder and plate is largely stationary throughout the rolling motion, allowing for localized mesh refinement. Figure 4 illustrates these points.

A potential difficulty in convective formulations is the tracking of boundaries [8]. In the present case, since a

round cylinder and a flat plate are considered, the boundaries are stationary and this is not a problem.

2.1 Material time derivatives

The material time derivative of a tensor quantity $\mathbf{s} = \mathbf{s}_X(\mathbf{X}, t) = \hat{\mathbf{s}}(\hat{\mathbf{X}}, t)$ (of any order) may be transformed as follows:

$$\begin{aligned} D_t \mathbf{s} &= \frac{\partial}{\partial t} \hat{\mathbf{s}}(\hat{\mathbf{X}}, t, t) \\ &= \frac{\partial \hat{\mathbf{s}}(\hat{\mathbf{X}}, t)}{\partial \hat{\mathbf{X}}} \cdot \frac{\partial \hat{\mathbf{X}}(\mathbf{X}, t)}{\partial t} + \frac{\partial \hat{\mathbf{s}}(\hat{\mathbf{X}}, t)}{\partial t} \quad (3) \\ &= (\mathbf{s} \otimes \hat{\mathbf{V}}) \cdot \bar{\mathbf{v}} + d_t \mathbf{s}, \end{aligned}$$

where $D_t(\cdot) := \partial(\cdot)/\partial t|_{\mathbf{X}^{-1}}$, $d_t(\cdot) := \partial(\cdot)/\partial t|_{\hat{\mathbf{X}}}$, $\hat{\mathbf{V}}$ is the vector differential operator with respect to $\hat{\Omega}$, and $\bar{\mathbf{v}}$ is the (undeformed) convective velocity:

$$\bar{\mathbf{v}} := D_t \hat{\phi}(\mathbf{X}, t) = \begin{cases} \omega(t) \mathbf{Q} \cdot \hat{\mathbf{X}} & \text{for } \hat{\mathbf{X}} \in \hat{\Omega}^c \\ -\bar{V}(t) \mathbf{e}_x & \text{for } \hat{\mathbf{X}} \in \hat{\Omega}^p, \end{cases} \quad (4)$$

where \mathbf{Q} is the constant matrix fulfilling $\dot{\mathbf{R}} \cdot \mathbf{R}^T = \omega \mathbf{Q}$. Here, ω is the counter-clockwise angular velocity and \bar{V} is the rightward translational velocity of the cylinder². Note that $\bar{\mathbf{v}}(\hat{\mathbf{X}}, t)$ is the velocity in $\hat{\Omega}$ of the material point $\mathbf{X} \ni \Omega_X$ which at the time t occupies the position $\hat{\mathbf{X}}$ in $\hat{\Omega}$.

In particular, the material velocity and acceleration are expressed as follows in terms of the ALE description:

$$\mathbf{v} = D_t \mathbf{x} = \dot{\hat{\mathbf{X}}} + D_t \hat{\mathbf{x}} = \dot{\hat{\mathbf{X}}} + \hat{\mathbf{F}} \cdot \bar{\mathbf{v}} + d_t \hat{\mathbf{x}} \quad (5)$$

and

$$\begin{aligned} \mathbf{a} &= D_t \mathbf{v} = \ddot{\hat{\mathbf{X}}} + \hat{\mathbf{G}} : (\bar{\mathbf{v}} \otimes \bar{\mathbf{v}}) + 2(d_t \hat{\mathbf{F}}) \cdot \bar{\mathbf{v}} \\ &\quad + \hat{\mathbf{F}} \cdot (D_t \bar{\mathbf{v}}) + d_{tt} \hat{\mathbf{x}}, \end{aligned} \quad (6)$$

respectively. Here, $\hat{\mathbf{G}} := \hat{\mathbf{x}} \otimes \hat{\mathbf{V}} \otimes \hat{\mathbf{V}}$ and

$$D_t \bar{\mathbf{v}} = \begin{cases} \dot{\omega} \mathbf{Q} \cdot \hat{\mathbf{X}} - \omega^2 \hat{\mathbf{X}} & \text{for } \hat{\mathbf{X}} \in \hat{\Omega}^c \\ -\dot{\bar{V}} \mathbf{e}_x & \text{for } \hat{\mathbf{X}} \in \hat{\Omega}^p. \end{cases} \quad (7)$$

A useful kinematical quantity in the context of rolling contact is the creepage [18]:

$$\xi := \frac{(V_T - V_C)}{(V_T + V_C)/2}, \quad (8)$$

where $V_T = \bar{V}$ is the rightward translational velocity of the cylinder and $V_C = -r_o \omega$ (where r_o is the radius of the cylinder) is its clockwise peripheral velocity. The creepage is thus the difference between the translational and peripheral velocity of the cylinder, normalized by their

¹ \mathbf{X} held fixed.

²For brevity, the argument t is henceforth omitted.

mean value. It can be used to characterize the rolling motion in the stationary/quasistatic case: In an idealized (undeformed) situation, $\xi = 0$ ($V_T = V_C \Rightarrow \bar{V} = -r_o \omega$) corresponds to pure rolling, $\xi < 0$ to accelerated rolling and $\xi > 0$ to decelerated rolling (braking). In particular, $\xi = 2$ corresponds to pure sliding ($\omega = 0$, \bar{V} arbitrary).

3 Thermomechanical problem

Assuming isotropic, homogeneous materials, small strains and small temperature fluctuations, the governing thermomechanical equations (momentum balance and energy balance, respectively) take the following form in terms of the ALE description [16]:

$$\begin{aligned} \hat{\rho} \left[\ddot{\hat{\mathbf{X}}} + \hat{\mathbf{G}} : (\bar{\mathbf{v}} \otimes \bar{\mathbf{v}}) + 2(d_t \hat{\mathbf{H}}) \cdot \bar{\mathbf{v}} \right. \\ \left. + \hat{\mathbf{F}} \cdot (D_t \bar{\mathbf{v}}) + d_{tt} \hat{\mathbf{u}} \right] - \hat{\mathbf{P}} \cdot \hat{\mathbf{V}} - \hat{\mathbf{B}} = 0 \text{ in } \hat{\Omega}, \quad (9) \end{aligned}$$

$$\begin{aligned} 3K\alpha\theta^{\text{ref}}(\mathbf{I} : d_t \hat{\mathbf{H}} + (\hat{\mathbf{H}} \cdot \bar{\mathbf{v}}) \cdot \hat{\mathbf{V}}) \\ + \hat{\rho} c \left(\hat{\mathbf{V}} \bar{\theta} \cdot \bar{\mathbf{v}} + d_t \bar{\theta} \right) + \hat{\mathbf{q}} \cdot \hat{\mathbf{V}} - \hat{r} = 0 \text{ in } \hat{\Omega}. \quad (10) \end{aligned}$$

Here, $\hat{\rho}$ is the density in $\hat{\Omega}$, $\hat{\mathbf{H}} = \hat{\mathbf{F}} - \mathbf{I}$ is the displacement gradient, $\hat{\mathbf{B}}$ is the external body force per unit volume in $\hat{\Omega}$, K is the bulk modulus, α is the thermal expansion coefficient, $\bar{\theta} = \theta - \theta^{\text{ref}}$ is the excess temperature with respect to the reference θ^{ref} , c is the mass specific heat capacity, and \hat{r} is the external heat power per unit volume in $\hat{\Omega}$. Further, $\hat{\mathbf{P}} = \mathbf{P} \cdot \hat{\mathbf{f}}^T$ and $\hat{\mathbf{q}} = \hat{\mathbf{f}} \cdot \mathbf{q}$ are push-forwards to $\hat{\Omega}$ of the first Piola–Kirchhoff stress tensor \mathbf{P} and the heat flux \mathbf{q} , respectively. In particular, a linear thermoelastic constitutive law is used for $\hat{\mathbf{P}}$:

$$\hat{\mathbf{P}} = \mathbf{E} : [\hat{\mathbf{H}} - \alpha \bar{\theta} \mathbf{I}] = \mathbf{E} : \hat{\mathbf{H}} - 3K\alpha \bar{\theta} \mathbf{I}, \quad (11)$$

where \mathbf{E} is the elasticity tensor. Further, Fourier's law is used as a constitutive law for $\hat{\mathbf{q}}$:

$$\hat{\mathbf{q}} = -k \hat{\mathbf{V}} \bar{\theta}, \quad (12)$$

where k is the constant heat conductivity. A more detailed derivation is given in Draganis et al. [16], which also states boundary conditions and presents the weak and FE forms of the problem.

Note that the deformation-dependent terms in the energy balance equation represent the Gough–Joule effect: reversible heating/cooling of the material resulting from a nonzero strain rate [19]. This effect is negligible for thermoelastic metals [20], and will therefore not be modelled in the following numerical simulations.

By construction of the employed ALE kinematical description, the intermediate time derivatives $d_t(\cdot)$ and

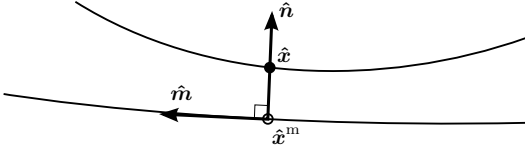


Figure 2: A point on the slave surface and its projection on the master surface, along with relevant unit vectors.

$d_{tt}(\cdot)$ vanish in the stationary case, resulting in a time-independent formulation [16]. In the transient case, a state of rolling where the cylinder's translational and rotational velocities are constant results in a problem in which the time-dependence is confined to the solution fields and external forces/fluxes. This means that in the FE formulation of the problem, the constituent matrices will be time-independent. If the assumption of constant velocities is not valid, these matrices are time-dependent (via the quantities $\ddot{\hat{\mathbf{X}}}$ and $\ddot{\mathbf{v}}$).

4 Contact formulation

The employed thermomechanical contact formulation – described in further detail in Draganis et al. [17] – is based on the computational contact theory presented in Wriggers [21]. In summary, a penalty formulation is used for normal mechanical contact, and a regularized version of Coulomb's friction law is used for tangential contact. A linear model of interfacial heat conduction is employed, and the heat flux due to frictional heat generation is based on an equal local heat partitioning between cylinder and plate. In the following, the basic kinematical and thermal quantities of the contact formulation are presented in the context of transient dynamics. Further, contact contributions to the weak form corresponding to tangential mechanical and thermal contact are expressed, hence complementing the corresponding normal contact contributions, previously expressed in Draganis et al. [16].

As a point $\hat{\mathbf{x}} \ni \hat{\omega}$ on the *slave* surface (here chosen as the cylinder surface) approaches the *master* surface (the plate surface), its projection point $\hat{\mathbf{x}}^m(\hat{\mathbf{x}}, t)$ on the master surface, as well as the associated normal ($\hat{\mathbf{n}}$) and tangential ($\hat{\mathbf{m}}$) vectors can be identified (see Figure 2). The gap function corresponding to the points $\hat{\mathbf{x}}$ and $\hat{\mathbf{x}}^m$ (or their respective undeformed counterparts $\hat{\mathbf{X}}$ and $\hat{\mathbf{X}}^m(\hat{\mathbf{X}}, t)$) can then be expressed as [21]

$$g = (\mathbf{x} - \mathbf{x}^m) \cdot \mathbf{n} = (\hat{\mathbf{x}} - \hat{\mathbf{x}}^m) \cdot \hat{\mathbf{n}}, \quad (13)$$

where \mathbf{n} is the counterpart of $\hat{\mathbf{n}}$ in ω_X . In terms of the

coordinates $\hat{\mathbf{X}}$ and t ,

$$g = g_{\hat{\mathbf{X}}}(\hat{\mathbf{X}}, t) := \left(\hat{\varphi}(\hat{\mathbf{X}}, t) - \hat{\varphi}(\hat{\mathbf{X}}^m(\hat{\mathbf{X}}, t), t) \right) \cdot \hat{\mathbf{n}}(\hat{\mathbf{X}}, t). \quad (14)$$

The slip velocity can be expressed as

$$\dot{s} = (D_t \mathbf{x} - D_t \mathbf{x}^m) \cdot \mathbf{m} = (D_t \hat{\mathbf{x}} - D_t \hat{\mathbf{x}}^m) \cdot \hat{\mathbf{m}}, \quad (15)$$

where \mathbf{m} is the counterpart of $\hat{\mathbf{m}}$ in ω_X . In terms of the coordinates $\hat{\mathbf{X}}$ and t ,

$$\dot{s} = \dot{s}_{\hat{\mathbf{X}}}(\hat{\mathbf{X}}, t) := \left((D_t \hat{\mathbf{x}})(\hat{\mathbf{X}}, t) - (D_t \hat{\mathbf{x}}^m)(\hat{\mathbf{X}}^m(\hat{\mathbf{X}}, t), t) \right) \cdot \hat{\mathbf{m}}(\hat{\mathbf{X}}, t). \quad (16)$$

Using eq. (5), the expression for \dot{s} can be expanded and divided into one stationary and one dynamic part:

$$\dot{s} = \dot{s}_{\text{stat}}(\hat{\mathbf{X}}, t) + \dot{s}_{\text{dyn}}(\hat{\mathbf{X}}, t), \quad (17)$$

where

$$\dot{s}_{\text{stat}} = \left(\hat{\mathbf{F}}(\hat{\mathbf{X}}, t) \cdot \bar{\mathbf{v}}(\hat{\mathbf{X}}, t) - \hat{\mathbf{F}}(\hat{\mathbf{X}}^m, t) \cdot \bar{\mathbf{v}}(\hat{\mathbf{X}}^m, t) \right) \cdot \hat{\mathbf{m}}(\hat{\mathbf{X}}, t)$$

and

$$\dot{s}_{\text{dyn}} = \left((d_t \hat{\mathbf{x}})(\hat{\mathbf{X}}, t) - (d_t \hat{\mathbf{x}}^m)(\hat{\mathbf{X}}^m(\hat{\mathbf{X}}, t), t) \right) \cdot \hat{\mathbf{m}}(\hat{\mathbf{X}}, t).$$

As mentioned in Draganis et al. [17], the employed regularization of Coulomb's law means that the step function that appears in the expression for the tangential force is replaced by the function

$$\phi(\dot{s}) = \tanh(\dot{s}/\epsilon_r). \quad (18)$$

Here, ϵ_r is a regularization parameter: the step function (Coulomb's law) is obtained in the limit $\epsilon_r \rightarrow 0$. ϵ_r has to be carefully chosen: For values that are too high, the computed solution will exhibit a dependence on ϵ_r , whereas values that are too low lead to convergence problems in the iterative solver. Note also that the range of acceptable values of ϵ_r depends on the magnitude of the slip velocity in the contact region [17].

The temperature difference, expressed in terms of $\hat{\mathbf{X}}$ and t , is

$$\Delta\theta(\hat{\mathbf{X}}, t) = \theta(\hat{\mathbf{X}}, t) - \theta(\hat{\mathbf{X}}^m(\hat{\mathbf{X}}, t), t) = \bar{\theta}(\hat{\mathbf{X}}, t) - \bar{\theta}(\hat{\mathbf{X}}^m(\hat{\mathbf{X}}, t), t). \quad (19)$$

The contributions to the weak form residual [16] corresponding to frictional forces and frictional heat generation are, respectively,

$$- \int_{\Gamma^g} \epsilon_r \mu g \phi(\dot{s}) [\underline{\mathbf{N}}_u^T(\hat{\mathbf{X}}) - \underline{\mathbf{N}}_u^T(\hat{\mathbf{X}}^m(\hat{\mathbf{X}}))] \hat{\mathbf{m}} \, d\mathcal{L}$$

and

$$\frac{1}{2} \int_{\hat{\Gamma}_c^s} \gamma_f \epsilon \mu g \phi \delta [\underline{N}_\theta^T(\hat{\mathbf{X}}) + \underline{N}_\theta^T(\hat{\mathbf{X}}^m(\hat{\mathbf{X}}))] d\mathcal{L}.$$

Here, $\hat{\Gamma}_c^s$ is the contact surface, ϵ is the penalty stiffness [21, 16], μ is the coefficient of friction and γ_f is the frictional heat transfer ratio: a parameter governing the ratio of the heat generated in the contact interface that enters the contacting bodies. An equal local heat partitioning between cylinder and plate was assumed.

In the discretized domain, a node-to-segment approach is used to construct contact elements across the contact interface. In the current study, these are chosen as linear-linear, regardless of the element orders used to discretize the two domains. For the triangular mesh used subsequently (see Section 5.4), this means that node forces and fluxes that arise due to the contact interaction are assembled only to corner nodes.

4.1 Irregular surface profiles

As mentioned in Section 2, one of the disadvantages of the ALE description is the associated difficulty of tracking domain boundaries. Specifically, since the ALE description involves convection of material points through the domain, any irregularity along the boundary is similarly transported in the direction of the convective flow as time progresses. This necessitates special measures such as frequent re-meshing to keep the mesh consistent with the geometry, likely outweighing any benefit gained from using the ALE description in the first place. These complications are avoided if all boundaries that are not in- or outflow boundaries follow the streamlines of the convective velocity field, as is the case for the currently considered problem (see Figure 5 and eq. (4)).

One way of modelling non-smooth surface profiles in the context of an ALE description while avoiding the complications discussed above, is by way of modification of the gap functions of the contact formulation [22, 23] (eq. (13)). Here, an offset function, fixed in the material domain Ω_X and representing the desired modification of the nominal surface profile, is imposed on the gap function g . No modifications to the computational domain itself are required.

5 Solution method

5.1 Numerically stabilized finite element formulation

The thermomechanical boundary value problem is discretized using the FE method. The weak and FE forms of the problem are derived in Draganis et al. [16].

Numerical instability problems related to the discretized energy balance equation have been found to arise

for the studied range of convective velocities. In order to address these problems, two different numerical stabilization methods are applied: For the plate domain, the Streamline-Upwind Petrov-Galerkin (SUPG) method [9, 24] is used. In the cylinder domain, a quasi residual-free bubble approach [25, 26], which is a variant of the scheme presented in Brezzi et al. [27], is used for the cylinder domain. The reader is referred to Draganis et al. [16] for a detailed description of the latter method, and an investigation of its performance.

5.2 Matrix decomposition scheme for system matrices

5.2.1 Finite element matrices

As mentioned in Section 3, the use of the ALE description results in an FE formulation wherein the constituent matrices (and vectors) depend on a set of convective velocity parameters. As a result, in simulations where these parameters vary in time, there arises an apparent need to reassemble in each time step the system matrices/vectors that depend on these parameters. This would result in very high computation times. However, in the present case (see Draganis et al. [16]), it may be observed that for each FE matrix/vector which depends on the convective velocity parameters ω , $\dot{\omega}$, \bar{V} and $\dot{\bar{V}}$, functions of these parameters may be factored out:

$$\begin{aligned} \underline{\mathbf{K}}_{uu} &= \underline{\mathbf{K}}_{uu}^0 + \omega^2 \underline{\mathbf{K}}_{uu}^\omega + \dot{\omega} \underline{\mathbf{K}}_{uu}^{\dot{\omega}} + \bar{V}^2 \underline{\mathbf{K}}_{uu}^{\bar{V}^2} + \dot{\bar{V}} \underline{\mathbf{K}}_{uu}^{\dot{\bar{V}}}, \\ \underline{\mathbf{C}}_{uu} &= \omega \underline{\mathbf{C}}_{uu}^\omega + \bar{V} \underline{\mathbf{C}}_{uu}^{\bar{V}}, \\ \underline{\mathbf{K}}_{\theta\theta} &= \underline{\mathbf{K}}_{\theta\theta}^0 + \omega \underline{\mathbf{K}}_{\theta\theta}^\omega + \bar{V} \underline{\mathbf{K}}_{\theta\theta}^{\bar{V}}, \\ \underline{\mathbf{K}}_{\theta u} &= \omega \underline{\mathbf{K}}_{\theta u}^\omega + \bar{V} \underline{\mathbf{K}}_{\theta u}^{\bar{V}}, \\ \underline{\mathbf{f}}_{uv} &= \underline{\mathbf{f}}_{uv}^{\text{ext}} + \omega^2 \underline{\mathbf{f}}_{uv}^\omega + \dot{\omega} \underline{\mathbf{f}}_{uv}^{\dot{\omega}} + \dot{\bar{V}} \underline{\mathbf{f}}_{uv}^{\dot{\bar{V}}}. \end{aligned} \quad (20)$$

See Appendix A for a detailed derivation of these expressions. Note that the matrices $\underline{\mathbf{M}}_{uu}$, $\underline{\mathbf{C}}_{\theta u}$, $\underline{\mathbf{K}}_{u\theta}$ and $\underline{\mathbf{C}}_{\theta\theta}$, and the force vectors $\underline{\mathbf{f}}_{us}$, $\underline{\mathbf{f}}_{\theta v}$ and $\underline{\mathbf{f}}_{\theta s}$ are independent of the convective velocity parameters [16].

Each right-hand side expression above is a linear combination of a series of time-independent matrices, with coefficients that are functions of the convective velocity parameters and their time-derivatives. Note that these time-independent matrices only have to be assembled once. After having done so, the time required for constructing a system matrix as a linear combination of these pre-assembled components is negligible compared to that of a full assembly of the matrix in question. Although complicated to implement, this scheme results in a vast reduction in computation times. Furthermore, in cases where the FE matrices need to be assembled multiple times per time step (such as when the external driving moment or horizontal force is to be controlled:

see Section 5.3), the reduction in computation time is even more significant.

5.2.2 Bubble stabilization matrices

The employed bubble function stabilization scheme involves constructing a local subgrid in each element, the configuration of which depends on the convective velocity field [16, 25]. For this reason, the resulting contributions to the FE matrices/vectors exhibit very complex dependences on the convective velocity parameters, and hence do not lend themselves to factorization in the manner described above. Instead, these contributions will be computed at predetermined instants in time: In case ω and \bar{V} are controlled, the contributions are updated whenever any one of these has changed by more than a specified factor as compared to the value at the previous update. This way, the total number of updates does not increase with the number of time steps. A convergence study with respect to this update frequency should be performed in this case, in order to ascertain the numerical soundness of the results.

In case the external moment M^{ext} and the external horizontal force F_x^{ext} are to be controlled, the angular velocity ω and the horizontal velocity \bar{V} (respectively) are unknown quantities (see Section 5.3). Hence, pre-computation of the stabilization matrices is not possible in this case, necessitating a modification of the strategy stated above. Instead, the stabilization contributions are assembled in the first time step (for which there exists a stationary start guess, containing information about initial velocities), and then reassembled at any time step at which the converged values of ${}^{n+1}\omega$ and ${}^{n+1}\bar{V}$ has changed by more than a specified factor as compared to the value at the previous update. It is noted that this complication emerges in part due to the adoption of a monolithic solution scheme (see Section 5.5). In contrast, in a staggered approach in which the mechanical problem is first solved separately, information about the convective velocities is always available at the stage when the thermal problem is to be solved, enabling computation of the stabilization contributions.

5.2.3 SUPG matrices

As mentioned in Section 5.1, the SUPG method [9] is used to stabilize the response in the plate domain. This method employs the test function

$$\delta\bar{\theta}^{\text{SUPG}} = \tau_e \hat{\rho} c \bar{\mathbf{v}} \cdot \hat{\nabla} \delta\bar{\theta}^{\text{G}},$$

where $\delta\bar{\theta}^{\text{G}}$ is the standard Galerkin test function and

$$\tau_e = \frac{h_e}{2\hat{\rho}c|\bar{\mathbf{v}}|} (\coth(P_e) - 1/P_e).$$

Here, h_e is a measure of the element size and $P_e = \hat{\rho}c|\bar{\mathbf{v}}|/h_e/(2k)$ is the Peclet number. Note that P_e depends

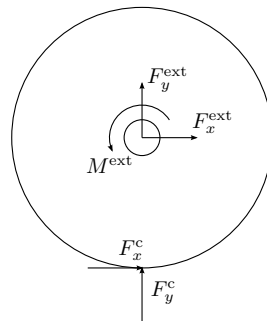


Figure 3: Resultants of external forces and moments acting on the cylinder.

both on the convective velocity parameters and on the element-dependent quantity h_e .

The matrix decomposition scheme described in Section 5.2.1 relies upon a reformulation of each matrix into a sum of matrices, each one being a multiplicative split into one matrix independent of the convective velocity parameters, and a coefficient that may be a function of these parameters. The term $\coth(P_e)$ in the expression for τ_e contains both the element-dependent quantity h_e and the convective velocity $\bar{\mathbf{v}}$. It therefore renders such a decomposition impossible for the SUPG contributions. This problem can be circumvented by approximating $\coth(P_e)$ by a Taylor series for low values of P_e , and by 1 for high values. Which of these approximations to choose can be decided on an element-to-element basis. The approach taken subsequently is to use a first-order version of this scheme where applicable (i.e. where encountered values of P_e do not come close to the intermediate range in which the above approximation is inaccurate) and the approach described in Section 5.2.2 – involving full assembly at select time steps – for all other cases.

5.3 Control of driving forces

Figure 3 illustrates all external forces and moments acting on the cylinder in the considered case. Here, M^{ext} , F_x^{ext} and F_y^{ext} represent the resultant external driving moment and the two components of the resultant external driving force acting on the cylinder inner boundary. F_x^c and F_y^c are the two components of the resultant contact force on the cylinder arising due to interaction with the plate.

It is noted that (M^{ext}, ω) and $(F_x^{\text{ext}}, \bar{V})$ are both work-conjugate pairs, in that $M^{\text{ext}} \cdot \omega$ and $F_x^{\text{ext}} \cdot \bar{V}$ represent rates of work done on the cylinder. As such, one member of the pair must be prescribed in each case, while the

other takes the role of a reaction, computable in post-processing. Prescribing either one of the velocity components ω and \bar{V} is straightforward, since they appear in the expression for $\bar{\mathbf{v}}$ (eq. (4)). Conversely, prescribing either one of M^{ext} and F_x^{ext} requires the introduction of constraint equations and iteration upon the respective unknowns ω and \bar{V} .

5.3.1 Stationary dynamics

The FE formulation of the stationary problem can be written as follows [16]:

$$\begin{aligned} \mathbf{r}_u(\hat{\mathbf{u}}, \bar{\boldsymbol{\theta}}, \omega, \bar{V}) &= \underline{\mathbf{f}}_{\text{int},u}(\hat{\mathbf{u}}, \bar{\boldsymbol{\theta}}, \omega, \bar{V}) - \underline{\mathbf{f}}_{\text{ext},u} = 0, \\ \mathbf{r}_\theta(\hat{\mathbf{u}}, \bar{\boldsymbol{\theta}}, \omega, \bar{V}) &= \underline{\mathbf{f}}_{\text{int},\theta}(\hat{\mathbf{u}}, \bar{\boldsymbol{\theta}}, \omega, \bar{V}) - \underline{\mathbf{f}}_{\text{ext},\theta} = 0. \end{aligned} \quad (21)$$

Here, $\underline{\mathbf{f}}_{\text{ext},u}$ and $\underline{\mathbf{f}}_{\text{ext},\theta}$ contain external forces: both prescribed forces and reactions. Further,

$$\begin{aligned} \underline{\mathbf{f}}_{\text{int},u}(\hat{\mathbf{u}}, \bar{\boldsymbol{\theta}}, \omega, \bar{V}) &= \mathbf{K}_{uu}(\omega, \bar{V}) \hat{\mathbf{u}} + \mathbf{K}_{u\theta}(\omega, \bar{V}) \bar{\boldsymbol{\theta}} \\ &\quad - \underline{\mathbf{f}}_{\text{conv},u}(\omega, \bar{V}) - \underline{\mathbf{f}}_{c,u}(\hat{\mathbf{u}}, \bar{\boldsymbol{\theta}}, \omega, \bar{V}), \\ \underline{\mathbf{f}}_{\text{int},\theta}(\hat{\mathbf{u}}, \bar{\boldsymbol{\theta}}, \omega, \bar{V}) &= \mathbf{K}_{\theta u}(\omega, \bar{V}) \hat{\mathbf{u}} \\ &\quad + (\mathbf{K}_{\theta\theta}(\omega, \bar{V}) + \mathbf{K}_{\theta\theta}^{\text{stab}}(\omega, \bar{V})) \bar{\boldsymbol{\theta}} - \underline{\mathbf{f}}_{\text{conv},\theta}^{\text{stab}}(\omega, \bar{V}) \\ &\quad - \underline{\mathbf{f}}_{c,\theta}(\hat{\mathbf{u}}, \bar{\boldsymbol{\theta}}, \omega, \bar{V}). \end{aligned} \quad (22)$$

are internal forces. Here, $\underline{\mathbf{f}}_{c,u}$ and $\underline{\mathbf{f}}_{c,\theta}$ are the contact contributions and $\underline{\mathbf{f}}_{\text{conv},u}$ represents fictitious (inertial) forces arising due to the employed kinematical description. The superscript ‘‘stab’’ denotes contributions corresponding to stabilization schemes (see Section 5.1).

In order to prescribe the moment M and/or the vertical force F_x acting on the cylinder hub, one or both of the following constraint equations are added to the equation system:

$$\begin{aligned} r_\omega(\hat{\mathbf{u}}, \bar{\boldsymbol{\theta}}, \omega, \bar{V}) &= M(\hat{\mathbf{u}}, \bar{\boldsymbol{\theta}}, \omega, \bar{V}) - M^{\text{ext}} = 0 \\ r_{\bar{V}}(\hat{\mathbf{u}}, \bar{\boldsymbol{\theta}}, \omega, \bar{V}) &= F_x(\hat{\mathbf{u}}, \bar{\boldsymbol{\theta}}, \omega, \bar{V}) - F_x^{\text{ext}} = 0. \end{aligned} \quad (23)$$

Here,

$$\begin{aligned} M(\hat{\mathbf{u}}, \bar{\boldsymbol{\theta}}, \omega, \bar{V}) &= \underline{\mathbf{A}}_M(\hat{\mathbf{u}}) \underline{\mathbf{f}}_{\text{ext},u}(\hat{\mathbf{u}}, \bar{\boldsymbol{\theta}}, \omega, \bar{V}) \\ &= \underline{\mathbf{A}}_M(\hat{\mathbf{u}}) \underline{\mathbf{f}}_{\text{int},u}(\hat{\mathbf{u}}, \bar{\boldsymbol{\theta}}, \omega, \bar{V}) \\ F_x(\hat{\mathbf{u}}, \bar{\boldsymbol{\theta}}, \omega, \bar{V}) &= \underline{\mathbf{A}}_{F_x} \underline{\mathbf{f}}_{\text{ext},u}(\hat{\mathbf{u}}, \bar{\boldsymbol{\theta}}, \omega, \bar{V}) \\ &= \underline{\mathbf{A}}_{F_x} \underline{\mathbf{f}}_{\text{int},u}(\hat{\mathbf{u}}, \bar{\boldsymbol{\theta}}, \omega, \bar{V}) \end{aligned} \quad (24)$$

where $\underline{\mathbf{A}}_M(\hat{\mathbf{u}})$ and $\underline{\mathbf{A}}_{F_x}$ are appropriately constructed matrices (see Appendix B.1). The deformation-dependence of the former matrix, owing to the slight change in shape of the cylinder inner boundary in its deformed state, is neglected in the following.

In case both M and F_x are to be controlled (which will be assumed in the following), the set of unknowns to iterate upon is $\hat{\mathbf{u}}, \bar{\boldsymbol{\theta}}, \omega$ and \bar{V} . The resulting non-linear problem is expressed as

$$\mathbf{r}(\underline{\mathbf{X}}) = \mathbf{0}, \quad (25)$$

where

$$\mathbf{r}(\underline{\mathbf{X}}) = \begin{bmatrix} \mathbf{r}_u(\underline{\mathbf{X}}) \\ \mathbf{r}_\theta(\underline{\mathbf{X}}) \\ r_\omega(\underline{\mathbf{X}}) \\ r_{\bar{V}}(\underline{\mathbf{X}}) \end{bmatrix}, \quad \underline{\mathbf{X}} = \begin{bmatrix} \hat{\mathbf{u}} \\ \bar{\boldsymbol{\theta}} \\ \omega \\ \bar{V} \end{bmatrix}. \quad (26)$$

In order to express the tangent stiffness $\partial \mathbf{r} / \partial \underline{\mathbf{X}}$ for this system, analytical expressions for the derivatives of $\underline{\mathbf{f}}_{\text{int},u}$ and $\underline{\mathbf{f}}_{\text{int},\theta}$ with respect to ω and \bar{V} are additionally required. One may here take advantage of the decomposition of time-dependent FE matrices and vectors described in Section 5.2. Starting from these expressions – being linear combinations of coefficients that are functions of ω and \bar{V} , and matrices that do not depend on these parameters – this differentiation is straightforward (see Appendix B.2).

Similarly, derivatives of SUPG contributions are simple to express in cases where the matrix decomposition scheme is applicable, but complicated otherwise. Derivatives of the bubble stabilization contributions are very complicated to express, due to their complex dependence on the convective velocities (see Section 5.2.2). The course taken in the current paper is to ignore the contribution from the stabilization terms to the rows and columns of the tangent stiffness matrix corresponding to ω and \bar{V} .

5.3.2 Transient dynamics

In the transient case, the residual equation for each time step is

$$\tilde{\mathbf{r}}({}^{n+1}\underline{\mathbf{X}}) = \mathbf{0},$$

where $\tilde{\mathbf{r}}({}^{n+1}\underline{\mathbf{X}})$ is the time-discretized residual associated with the time interval $t_n < t < t_{n+1}$ and ${}^{n+1}\underline{\mathbf{X}} = [{}^{n+1}\hat{\mathbf{u}} \quad {}^{n+1}\bar{\boldsymbol{\theta}} \quad {}^{n+1}\omega \quad {}^{n+1}\bar{V}]^T$ is the set of unknowns. The components of the residual are

$$\begin{aligned} \tilde{r}_u({}^{n+1}\underline{\mathbf{X}}) &= \tilde{\underline{\mathbf{f}}}_{\text{int},u}({}^{n+1}\underline{\mathbf{X}}) - \tilde{\underline{\mathbf{f}}}_{\text{ext},u} = 0, \\ \tilde{r}_\theta({}^{n+1}\underline{\mathbf{X}}) &= \tilde{\underline{\mathbf{f}}}_{\text{int},\theta}({}^{n+1}\underline{\mathbf{X}}) - \tilde{\underline{\mathbf{f}}}_{\text{ext},\theta} = 0 \\ \tilde{r}_\omega({}^{n+1}\underline{\mathbf{X}}) &= \tilde{M}({}^{n+1}\underline{\mathbf{X}}) - \tilde{M}^{\text{ext}} = 0 \\ \tilde{r}_{\bar{V}}({}^{n+1}\underline{\mathbf{X}}) &= \tilde{F}_x({}^{n+1}\underline{\mathbf{X}}) - \tilde{F}_x^{\text{ext}} = 0, \end{aligned} \quad (27)$$

where

$$\begin{aligned}
\tilde{\mathbf{f}}_{\text{int},u}({}^{n+1}\mathbf{X}) &= \tilde{\mathbf{M}}_{uu}\tilde{\mathbf{v}}_d({}^{n+1}\hat{\mathbf{u}}) + \tilde{\mathbf{C}}_{uu}\tilde{\mathbf{v}}({}^{n+1}\hat{\mathbf{u}}) \\
&\quad + \tilde{\mathbf{K}}_{uu}\tilde{\mathbf{u}}({}^{n+1}\hat{\mathbf{u}}) + \mathbf{K}_{u\theta}\tilde{\boldsymbol{\theta}}({}^{n+1}\hat{\boldsymbol{\theta}}) \\
&\quad - \tilde{\mathbf{f}}_{\text{conv},u}({}^{n+1}\boldsymbol{\omega}, {}^{n+1}\bar{\mathbf{V}}) - \mathbf{f}_{c,u}({}^{n+1}\mathbf{X}) \\
\tilde{\mathbf{f}}_{\text{int},\theta}({}^{n+1}\mathbf{X}) &= \tilde{\mathbf{C}}_{\theta u}\tilde{\mathbf{v}}({}^{n+1}\hat{\mathbf{u}}) + \tilde{\mathbf{K}}_{\theta u}\tilde{\mathbf{u}}({}^{n+1}\hat{\mathbf{u}}) \\
&\quad + \tilde{\mathbf{C}}_{\theta\theta}\tilde{\boldsymbol{\theta}}_d({}^{n+1}\hat{\boldsymbol{\theta}}) \\
&\quad + (\tilde{\mathbf{K}}_{\theta\theta} + \tilde{\mathbf{K}}_{\theta\theta}^{\text{stab}})\tilde{\boldsymbol{\theta}}({}^{n+1}\hat{\boldsymbol{\theta}}) \\
&\quad - \tilde{\mathbf{f}}_{\text{conv},\theta}^{\text{stab}}({}^{n+1}\boldsymbol{\omega}, {}^{n+1}\bar{\mathbf{V}}) - \mathbf{f}_{c,\theta}({}^{n+1}\mathbf{X}) \\
\mathbf{v} &= \hat{\mathbf{u}}.
\end{aligned} \tag{28}$$

(the dependence of the $\tilde{\mathbf{M}}$ - $\tilde{\mathbf{C}}$ - and $\tilde{\mathbf{K}}$ -matrices above on ${}^{n+1}\boldsymbol{\omega}$ and ${}^{n+1}\bar{\mathbf{V}}$ has been suppressed for brevity). In the above, the notation $(\tilde{\cdot})$ denotes quantities in which all time-dependent quantities are time-discretized as

$$\mathbf{s} \approx \tilde{\mathbf{s}} = \Theta {}^{n+1}\mathbf{s} + (1 - \Theta) {}^n\mathbf{s},$$

and their time-derivatives as

$$\dot{\mathbf{s}} \approx \tilde{\mathbf{s}}_d = \frac{{}^{n+1}\mathbf{s} - {}^n\mathbf{s}}{\Delta t}$$

Here, $\Theta = 1$ in the present case (corresponding to an Euler Backward scheme) and Δt is the time step size. Note that the contact contributions $\mathbf{f}_{c,u}$, $\mathbf{f}_{c,\theta}$ are always evaluated at the current time step.

The construction of the tangent stiffness matrix in the transient case additionally requires the derivatives of $\tilde{\mathbf{f}}_{\text{int},u}$ and $\tilde{\mathbf{f}}_{\text{int},\theta}$ with respect to ${}^{n+1}\boldsymbol{\omega}$ and ${}^{n+1}\bar{\mathbf{V}}$. Here, as before, the contributions from the stabilization matrices are neglected. Noticing that

$$\frac{\partial \tilde{\mathbf{s}}}{\partial {}^{n+1}\mathbf{s}} = \Theta, \quad \frac{\partial \tilde{\mathbf{s}}_d}{\partial {}^{n+1}\mathbf{s}} = 1/\Delta t,$$

and that the transient parts of the contact forces are independent of ${}^{n+1}\boldsymbol{\omega}$ and ${}^{n+1}\bar{\mathbf{V}}$ (see Section 4), it is seen that the construction of the tangent stiffness matrix in the transient case does not involve any significant complications as compared to the stationary case.

5.4 Discretization

The FE formulation of the problem is implemented in MATLAB. The element type used is a triangular element with one/two degrees of freedom per node for the thermal/mechanical fields, respectively. The approximation for both displacements and temperatures is piecewise linear in the plate and piecewise quadratic in the cylinder.

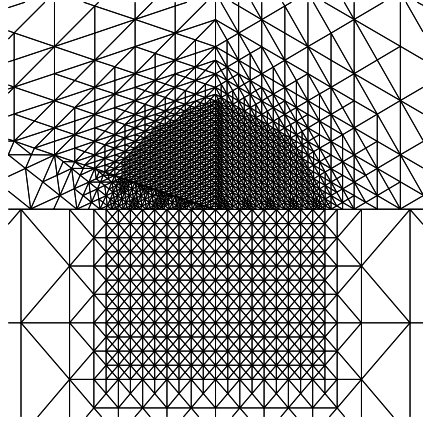
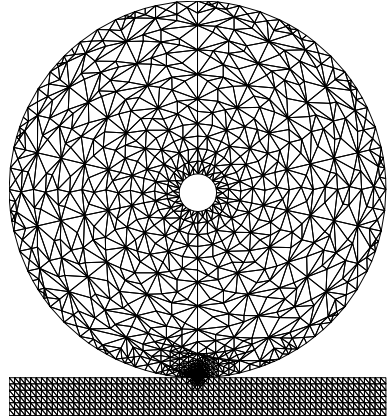


Figure 4: Employed FE mesh, with a zoomed-in view of the refined contact region.

The employed mesh, shown in Figure 4, is constructed according to the scheme described in Draganis et al. [16]. The Euler-backward scheme is chosen for the time-discretization.

5.5 Contact iterations

The addition of the nonlinear contact contributions to the (otherwise linear) FE formulation of the thermo-mechanical boundary value problem leads to a nonlinear equation system. This system is solved monolithically by the Newton method, employing a contact iteration scheme following Wriggers [21]. For the transient problem, the contact contributions are consistently evaluated at the current time step, regardless of the time-discretization scheme used for the solution fields in other

terms.

In the frictional contact iterations, convergence can sometimes be difficult to achieve, especially when slip velocities and/or normal pressures are high. For the stationary problem (e.g. when computing the stationary start configurations used for the transient simulations), a velocity stepping scheme is implemented to address this issue. Here, convective velocities in cylinder and plate are gradually increased, the solution for one step serving as a start guess for the next. The start guess used for the first velocity-stepping iteration is the solution to the corresponding frictionless contact problem. The start guess used here is in turn obtained from a simplified problem employing appropriate Hertzian contact pressure distributions as contact loads.

In the transient case, convergence problems might arise as a result of the chosen time step size being too large to resolve dynamical phenomena local to the contact region. Hence, convergence may in this case be facilitated by a reduction of the time step size.

6 Numerical examples

The following numerical examples are based on a 2D (plane strain) model of a hollow cylinder rolling on a plate. The model features an isotropic, homogeneous, linear elastic material. A vertical force is applied on the inner boundary (hub) of the cylinder. Gravitational loads on the bodies are not included, whereas inertial effects are modelled. The base of the plate is fixed in all degrees of freedom and the cylinder hub is fixed in the horizontal direction (in Ω). All other boundaries are free. The temperature is prescribed (to the reference temperature) along the cylinder hub and at the plate ends, while all other boundaries (not in contact) are thermally insulated. Figure 5 shows a schematic illustration of the geometry, boundary conditions and loads of the employed model. Note that the resultant driving force and moment (shown in Figure 3) are not included in this figure. The reason is that they are not imposed explicitly: They either take the form of reactions or are imposed via additional constraint equations (see Section 5.3).

A reference parameter setup (used in the following unless otherwise indicated) is now defined. Material parameters in both bodies are: Young’s modulus $E = 200$ GPa, Poisson’s ratio $\nu = 0.3$, specific heat capacity $c = 460$ Jkg⁻¹K⁻¹, thermal conductivity $k = 45$ Wm⁻¹K⁻¹, thermal expansion coefficient $\alpha = 4.8 \cdot 10^{-6}$ K⁻¹ and density $\rho = 8 \cdot 10^3$ kgm⁻³. Outer and inner radii of the cylinder are $r_o = 50$ cm and $r_i = 5$ cm, respectively. The height of the plate is $h = 0.1$ m and the width of the modeled plate domain is chosen as $b = 1$ m. The coefficient of friction is $\mu = 0.4$, the (velocity-independent) interfacial heat conductivity is $k_c = 10^7$ Wm⁻²K⁻¹, the frictional heat transfer ratio is $\gamma_f = 10\%$, the penalty

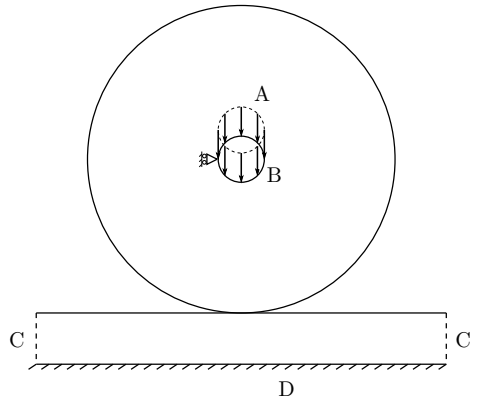


Figure 5: Schematic illustration of the thermomechanical model. A: applied mechanical load, B: cylinder hub (fixed in horizontal direction, fixed temperature), C: artificial plate domain ends (fixed temperature), D: plate base (fixed in all displacement degrees of freedom).

stiffness is $\epsilon_n = 5$ TN/m and the regularization parameter for the friction law is $\epsilon_r = 10^{-4}$ m/s. The reference (environmental) temperature is $\theta^{ref} = 293$ K and the applied mechanical load is $F_y^{ext} = 100$ kN/m.

For some of the subsequent numerical examples (when explicitly stated), Rayleigh damping [28] is implemented. When it is used, the coefficients corresponding to the mass- and stiffness matrices are $r_0 = 0$ and $r_1 = 10^{-4}$ s. Wherever Rayleigh damping is not used in the following, the reason is to keep computed results free from extraneous influencing factors, in order to facilitate and clarify their qualitative study.

6.1 Analytical validation

Carter theory concerns 2D rolling contact between an elastic cylinder and an elastic half-space [2, 18, 3]. By Carter theory, a given normal load and creepage ξ (as defined in eq. (8)) – along with information about geometrical and constitutive parameters – correspond to a certain tangential pressure distribution. Carter’s analytical theory requires the assumptions underlying Hertz theory to hold, i.e. it concerns stationary/quasistatic, purely mechanical rolling, and is based on the half-space assumption. The Carter–Hertz theory will nevertheless be used in the following for comparisons with computed results.

The computational model has been validated against analytical solutions to one-dimensional transient heat conduction problems.

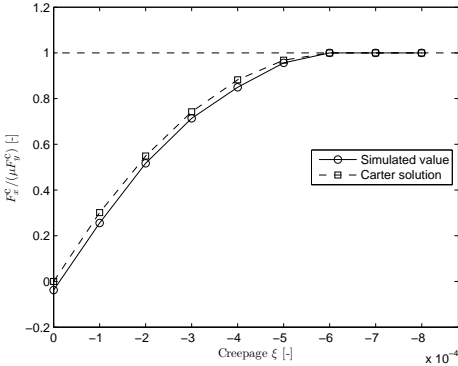


Figure 6: Force–creepage curve from a series of stationary simulations, along with the analytical Carter–Hertz solution.

6.2 Transient simulations

A series of simulations featuring various transient, thermomechanically coupled rolling contact phenomena are presented in the following. Each simulation employs a given stationary solution – prevailing at time $t \leq 0$ – as a start configuration.

6.2.1 Stick/slip transitional states

Figure 6 shows the ratio of the resultant horizontal friction force F_x^c and its limit μF_y^c versus the creepage ξ for a series of stationary simulations³. The analytical Carter–Hertz force–creepage curve is also shown. If $\xi = \xi_{fs}$ is the point of onset of full slip, it is seen from the figure that $\xi_{fs} \approx -6 \cdot 10^{-4}$. Furthermore, it is noted that the simulated resultant tangential contact force is nonzero for $\xi = 0$. This is a consequence of local deformations in the vicinity of the contact region slightly displacing the creepage value corresponding to pure rolling (i.e. rolling with $F_x^c = 0$). This phenomenon also accounts for the discrepancy between the two curves in the interval $0 < \xi < \xi_{fs}$. However, the creepage $\xi = 0$ will still be used in the following whenever free rolling is to be prescribed.

In order to analyze the dynamical transition from pure rolling to full slip, a series of simulations are performed. For each one, the start condition is a state of stationary, pure rolling with $\bar{V} = 50$ km/h. During the time interval $0 < t < 0.7t_e$, the creepage is varied linearly from $\xi = 0$

³Due to local deformations, the x - and y -directions do not exactly coincide with the tangential and normal directions, respectively, across the contact region. $F_x^c / (\mu F_y^c)$ is therefore only approximately equal to unity in the case of full slip, although the difference is negligible.

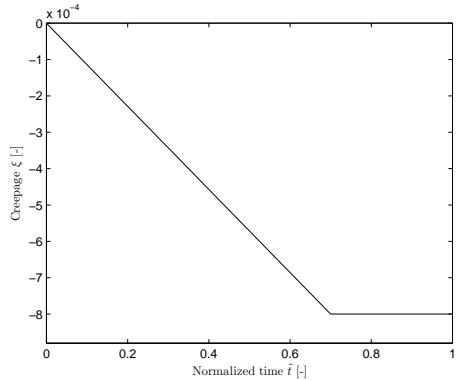


Figure 7: Prescribed time-history of ξ .

to $\xi = -8 \cdot 10^{-4}$, whereafter it is kept constant. Here, t_e is the end time of the simulation. The time interval of each simulation performed in the following can be denoted as $0 < \tilde{t} < 1$, where $\tilde{t} := t/t_e$ is a normalized time parameter. The time-history of the prescribed creepage can then be expressed as

$$\xi(\tilde{t}) = \begin{cases} \xi_0 \tilde{t} / \tilde{t}_0 & 0 \leq \tilde{t} < \tilde{t}_0 \\ \xi_0 & \tilde{t}_0 \leq \tilde{t} \leq 1, \end{cases} \quad (29)$$

where $\xi_0 = -8 \cdot 10^{-4}$ and $\tilde{t}_0 = 0.7$ (see Figure 7). Note that $\xi = \xi_0 > \xi_{fs}$ represents a state of rolling well above the limit of full slip (cf. Figure 6). The creepage is prescribed by holding \bar{V} constant and appropriately controlling ω . The subsequent simulations all feature different values of t_e , which means that the value of the creepage rate $\dot{\xi}$ in the interval $0 < \tilde{t} < \tilde{t}_0$, namely $\dot{\xi} = \xi_0 / (\tilde{t}_0 t_e)$, also takes different values. Table 1 shows the simulation time t_e , the resulting creepage rate $\dot{\xi}$, and the number of time steps used for each simulation. Note that simulations 5 and 6 use a larger number of time steps than the others. This is for convergence reasons.

Figure 8 shows the frictional ratio $F_x^c / (\mu F_y^c)$ versus the normalized time \tilde{t} for each simulation. The vertical dashed line indicates the instant in time $\tilde{t} = \tilde{t}_0$, i.e. the time in which ξ reaches its final value ξ_0 . Also included in the figure is the analytical Carter–Hertz curve, and the data from the stationary/quasistatic simulations, previously shown in Figure 6. Here, the well-defined relation between the creepage ξ and the normalized time \tilde{t} in each simulation (eq. (29)), is used to adapt this data to Figure 8, in which the quantity used for the x -axis is the latter. The curves representing the simulations 1–6 are arranged from bottom to top in the figure.

It is seen from Figure 8 that for approximately $|\dot{\xi}| < 4 \cdot 10^{-3} \text{ s}^{-1}$, the creepage rate is sufficiently low for the

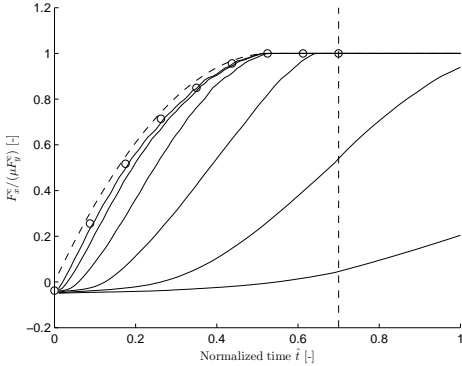


Figure 8: Frictional ratio $F_x^c/(\mu F_y^c)$ vs. normalized time \tilde{t} for the considered transient simulations, along with stationary/quasistatic (circles) and analytical (dashed curve) solutions. The vertical dashed line corresponds to \tilde{t}_0 : the time at which ξ reaches its final value. The curves representing the simulations 1–6 are arranged from bottom to top.

Table 1: Number of time steps, simulation times t_e and creepage rates $\dot{\xi}$ used in the transient simulations.

Sim. no.	Time steps	t_e [s]	$\dot{\xi}$ [s^{-1}]
1	100	$1.0 \cdot 10^{-3}$	-1.1
2	100	$3.2 \cdot 10^{-3}$	$-3.6 \cdot 10^{-1}$
3	100	$1.0 \cdot 10^{-2}$	$-1.1 \cdot 10^{-1}$
4	100	$3.2 \cdot 10^{-2}$	$-3.6 \cdot 10^{-2}$
5	200	$1.0 \cdot 10^{-1}$	$-1.1 \cdot 10^{-2}$
6	200	$3.2 \cdot 10^{-1}$	$-3.6 \cdot 10^{-3}$

mechanical response to behave essentially quasistatically, whereas in the approximate range $|\dot{\xi}| > 4 \cdot 10^{-3} s^{-1}$, the response exhibits transient behaviour: the mechanical response lags behind the variation in creepage.

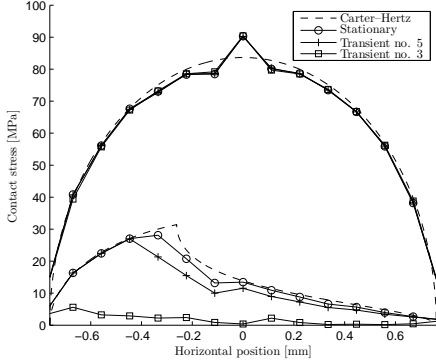
Figure 9 shows snapshots of the normal and tangential stress distributions (acting on the plate surface) at specified values of \tilde{t} (and thus specified values of ξ). Each figure shows data from two of the transient simulations: no. 3 & 5, along with data from the corresponding stationary/quasistatic solution. The analytical Carter–Hertz contact stress curves are also included. As mentioned earlier, the discrepancies between the analytical curves and the stationary solutions are due to deformation-dependent effects that are not modelled in Carter–Hertz theory. In each time instant, the momentaneous discrepancy between the transient solutions and the stationary/quasistatic solution – which is larger for higher values of $\dot{\xi}$ – is due to dynamical effects. Note from Figure 8 that the points at which the transient curves connect with the quasistatic curve vary between the simulations. In particular, this occurs around $\tilde{t} = 0.65$ for simulation no. 3 and around $\tilde{t} = 0.5$ for simulation no. 5. Before this point of connection, the stress distribution – and the extents of the regions of stick/slip – differ from those of the quasistatic solution. This is reflected in the plots in Figure 9.

Figure 10 shows the temperature at the point $\hat{X} \in \hat{\Omega}$ pertaining to initial contact on the cylinder surface, versus the normalized time \tilde{t} , for the considered set of simulations. Here, as in Figure 8, the curves representing the simulations 1–6 are once again positioned from bottom to top. No tendency toward a convergence to quasistatic behaviour can be observed from the figure: much smaller creepage rates $\dot{\xi}$ than those presently considered would be required for that to occur. Note also how the temperature barely changes at all for the highest creepage rate featured (curve no. 1). Clearly, the mechanical response operates on much smaller time scales than the thermal response.

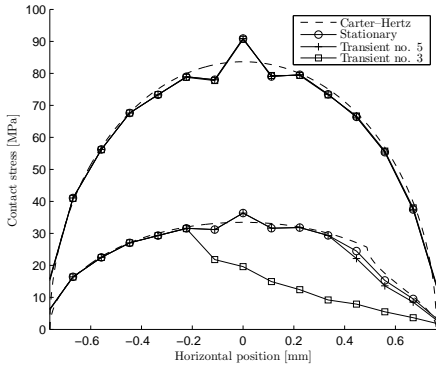
6.2.2 Tractive rolling

In the following, a series of simulations featuring tractive rolling are presented. In the first set of simulations, the rolling velocities ω and \bar{V} are controlled. In a following simulation, the driving force F_x and the driving moment M will instead be chosen as the controlled quantities.

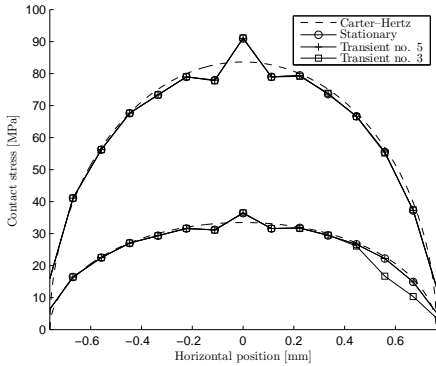
Controlled velocities Sudden, heavy braking from a state of pure rolling ($\xi = 0$) with $\bar{V} = 50$ km/h, to a state of pure rolling with $\bar{V} = 10$ km/h, is considered. The simulation time is $t_e = 10$ s and the number of time steps is 100. Two simulations (*a* and *b*) are performed, which differ only in the prescribed time-history of \bar{V} . In both simulations, ω is prescribed in the same way.



(a) $\tilde{t} = 0.17$ ($\xi = -2 \cdot 10^{-4}$).



(b) $\tilde{t} = 0.44$ ($\xi = -5 \cdot 10^{-4}$).



(c) $\tilde{t} = 0.61$ ($\xi = -7 \cdot 10^{-4}$).

Figure 9: Contact stress distributions on the plate surface for three different values of \tilde{t} and ξ . In each plot, the upper/lower set of curves represents normal/tangential contact stress distributions, respectively. The Carter-Hertz analytical solution, the stationary/quasistatic solution, and two transient solutions are included.

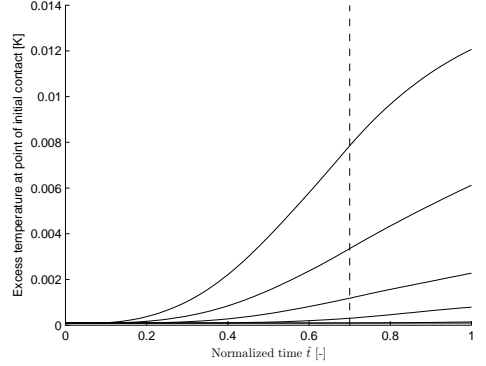


Figure 10: Excess temperature at the point of initial contact on the cylinder surface versus the normalized time \tilde{t} , for the considered set of simulations. The curves representing the simulations 1–6 are arranged from bottom to top.

In particular, ω reaches its final value before \bar{V} does. The chosen piecewise linear–quadratic time-histories of $V_T = \bar{V}$ and $V_C = -r_o\omega$ are shown in Figure 11.

Figure 12 shows the resulting time-history of the creepage ξ . For reference, recall that $\xi = 2$ corresponds to pure sliding (see eq. (8)). For both simulations, the smallest nonzero value of the creepage for any discrete time step is still above the full slip limit ξ_{fs} , i.e. the transition between stick/slip and full slip is not resolved in this simulation (as opposed to the case in Section 6.2.1). For this reason, it is also the case that $F_x^c = \mu F_y^c$ whenever $\xi \neq 0$.

Figure 13 shows the resultant horizontal reaction force F_x^{ext} (see Figure 3), the resultant horizontal contact force F_x^c , and their sum $F_x^{\text{tot}} := F_x^{\text{ext}} + F_x^c$. Note that $F_x^{\text{tot}} = m_{\text{cyl}}\dot{\bar{V}}$, where m_{cyl} is the mass of the cylinder, i.e. F_x^{tot} derives directly from controlled quantities (cf. Figure 11, where $\bar{V}(t)$ is shown). Further, note that the value of F_x^c is not quite zero for $\xi = 0$. The reason, as mentioned in Section 6.2.1, is that local deformations in the contact region slightly displace the creepage value corresponding to pure rolling.

As mentioned, $F_x^{\text{ext}} = m_{\text{cyl}}\dot{\bar{V}} - F_x^c$ is a reaction. For simulation a, F_x^{ext} is almost zero in the initial interval in which \bar{V} varies linearly (see Figure 13a). It can therefore be concluded that it is the frictional force alone that accounts for the acceleration in this region, i.e. $F_x^c \approx F_x^{\text{tot}} = m_{\text{cyl}}\dot{\bar{V}}$ here. Further, since $F_x^c = \mu F_y^c$ in the region where F_x^{tot} varies linearly, the reaction F_x^{ext} must as a result include a spike here (i.e. to fulfill $F_x^{\text{ext}} = F_x^{\text{tot}} - F_x^c$), which may be observed in both

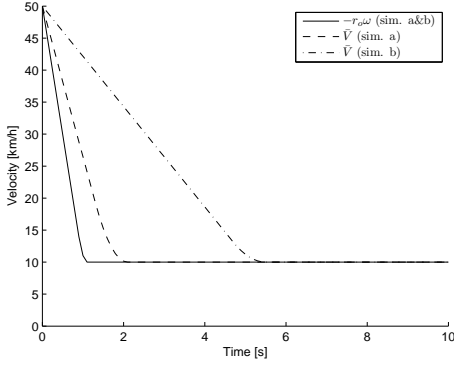
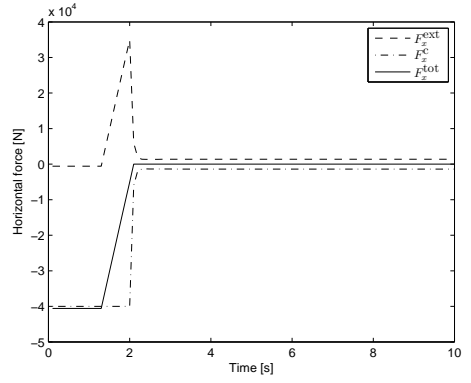
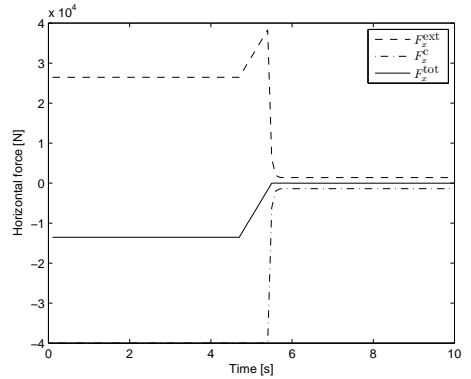


Figure 11: Prescribed time-histories of the translational rolling velocity \bar{V} and the peripheral velocity $-r_o\omega$.



(a) Simulation a.



(b) Simulation b.

Figure 13: Computed time-evolutions of horizontal forces.

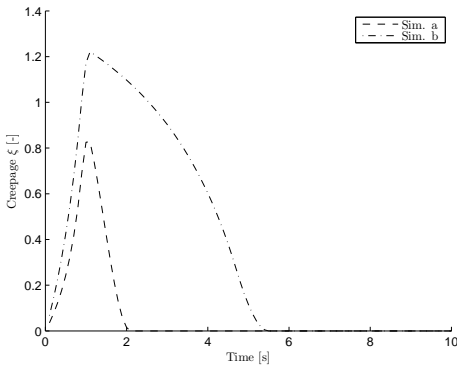
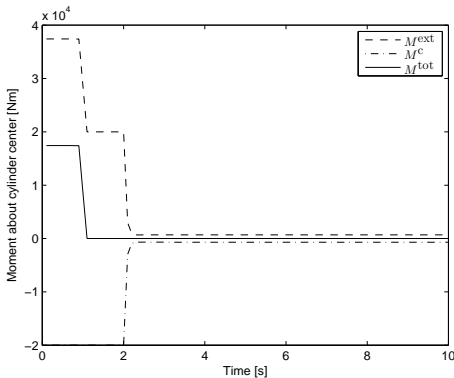
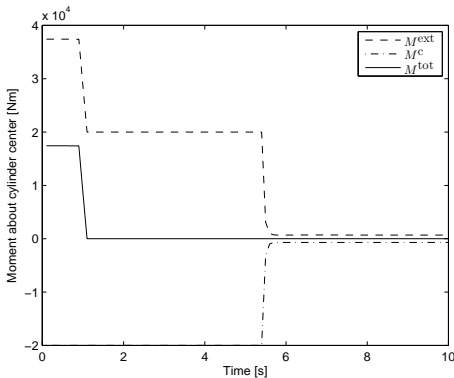


Figure 12: Time-history of the creepage ξ as a result of the prescribed time-histories of \bar{V} and ω .



(a) Simulation a.



(b) Simulation b.

Figure 14: Computed time-evolutions of moments about the cylinder center.

plots in Figure 13. Seen from another perspective, the spike in F_x^{ext} is a consequence of the particular choice of $\bar{V}(t)$ and $\omega(t)$ deviating from the natural time-evolutions of these quantities that would result from controlling the external moment M and the external force F_x .

Figure 14 shows the resultant reaction moment about the cylinder center, M^{ext} (see Figure 3), the resultant moment of the contact forces, $M^c \approx r_o F_x^{\text{ext}}$, and their sum $M^{\text{tot}} := M^{\text{ext}} + M^c$ (all moments are positive in the counter-clockwise direction). Note that $M^{\text{tot}} = I_{\text{cyl}} \dot{\omega}$, where I_{cyl} is the moment of inertia of the cylinder about its central axis. Thus, M^{tot} derives directly from controlled quantities (cf. Figure 11, where $\omega(t)$ is shown). The time-evolution of M^c can be understood by noting that $M^c \approx r_o F_x^{\text{ext}}$ (see Figure 3) and comparing with Figure 13.

At the second plateau and onward in the time-

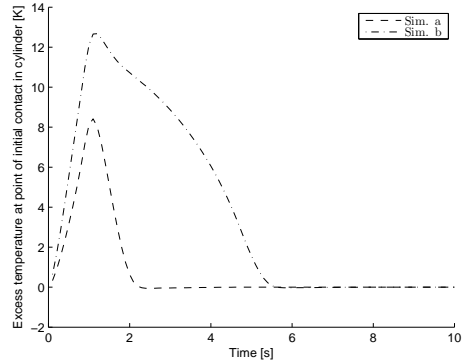


Figure 15: Temperature at the point of initial contact on the cylinder surface for simulations a and b.

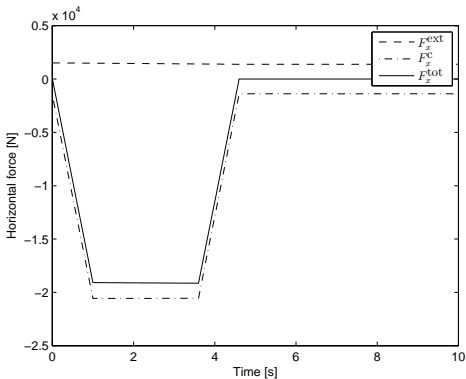
evolution of M^{ext} (i.e. for $t > 1.1$ s in both simulations), this moment is exactly equal and opposite to M^c : The latter, directed clockwise, tends to bring the system back to a state of pure rolling, and must thus be opposed by a counter-clockwise moment in order to satisfy the requirement $\dot{\omega} = 0$ (cf. Figure 11). At the first plateau, M^{ext} is larger still, so as to give rise to a counter-clockwise (braking) angular acceleration ($\dot{\omega} > 0$).

Figure 15 shows the time-evolution of the temperature at the point of initial contact on the cylinder surface for both simulations. The shape of the curve is close to that of the creepage curve, seen in Figure 12. The reason is that the latter corresponds closely to the time-history of local slip velocities in the contact region, and hence to the frictional heat generation.

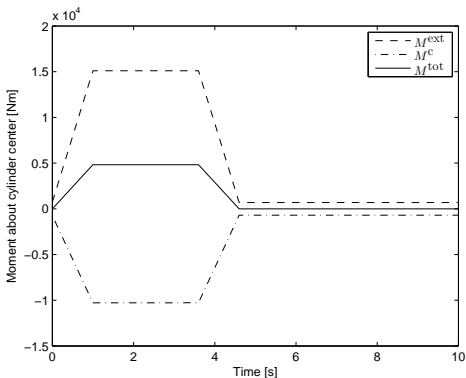
Controlled driving forces In the next example, the driving force and moment are controlled (using the methodology described in Section 5.3) with the aim to bring about a motion similar to that achieved in the previous example: Starting from a stationary state of pure rolling ($\xi = 0$) with $\bar{V} = 0$, the external driving moment M^{ext} is varied in a piecewise linear fashion (as shown in Figure 16b), so as to reduce the horizontal rolling velocity \bar{V} to around 10 km/h in a time that is in the order of 5 s. The external horizontal driving force F_x^{ext} is kept largely constant, except that it is varied linearly from its start value to its end value (see Figure 16a).

The initial and final values of M^{ext} and F_x^{ext} are chosen to the values they obtain in the case of stationary, pure rolling featuring $\bar{V} = 50$ km/h and $\bar{V} = 10$ km/h, respectively (separately determined in a set of stationary analyses).

Temperatures will not be included in the presented



(a) Prescribed time-history of the external horizontal force F_x^{ext} , and computed time-evolutions of the contact force F_x^c and the total force F_x^{tot} .



(b) Prescribed time-history of the external moment M^{ext} , and computed time-evolutions of the contact moment M^c and the total moment M^{tot} .

Figure 16: Time-histories of forces and moments.

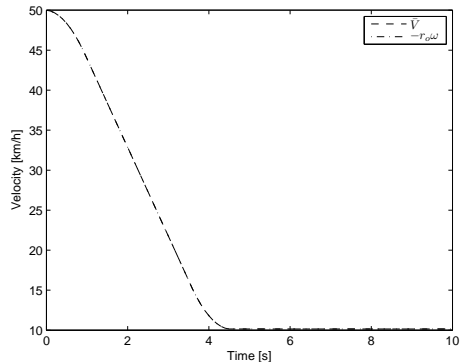


Figure 17: Computed time-evolutions of the translational rolling velocity \bar{V} and the peripheral velocity $-r_o\omega$. Note: the two curves coincide in the figure.

results, which will instead be focused on the computed velocities. Hence, there is no need for numerical stabilization in this case, and it will therefore not be implemented.

The resulting time-evolutions of the velocities and the creepage are shown in Figure 17 and Figure 18, respectively. It is noted that the maximum value of the creepage is only about $1.9 \cdot 10^{-4}$, which means that the braking tangential contact force F_x^c only reaches about 48% of its maximum value (cf. Figure 6). In contrast, simulation *a* of the previous example (which is comparable to the current simulation in that in both cases, $F_x^{\text{tot}} \approx F_x^c$ throughout most of the braking phase) involved a fully developed frictional force F_x^c . Hence the shorter braking time in the latter case (compare Figures 11 and 17).

6.2.3 Negotiation of non-smooth surface profile

Pure sliding ($\xi = 2$) with $\bar{V} = 50$ km/h over a sharp hole in the plate is considered. The hole has a width of 0.5 mm, perpendicular edges, and is modelled as described in Section 4.1. It is deep enough so that contact between its bottom and the cylinder does not occur during traversal, but may be considered shallow enough so as not to affect the structural properties of the plate domain. It is noted that the width of the hole is about 1/3 of the contact patch width (cf. Figure 9). The hole is positioned so that the contact patch reaches it at approximately $t_1 = 90 \mu\text{s}$ and leaves it at approximately $t_2 = 230 \mu\text{s}$. Due to the violent interaction between cylinder and plate as the hole is traversed, Rayleigh damping is implemented, using the coefficients stated previously. The total simulation time is $t_e = 10$ ms and the number of time steps is 1000.

Figures 19 and 20 show the time-evolution of the tem-

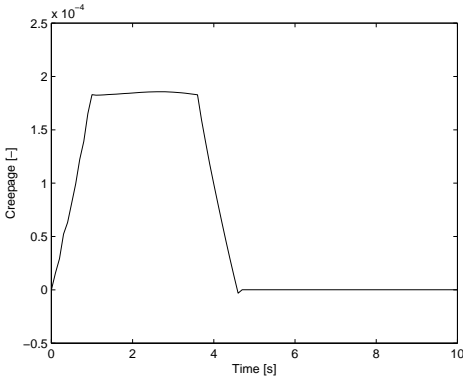
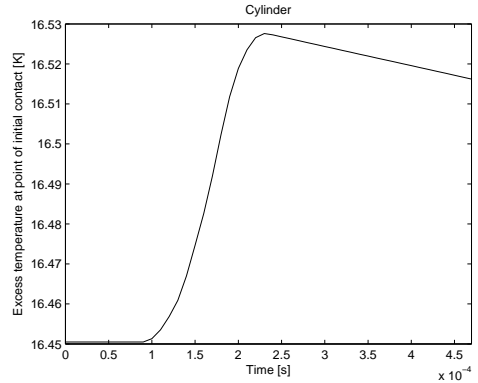


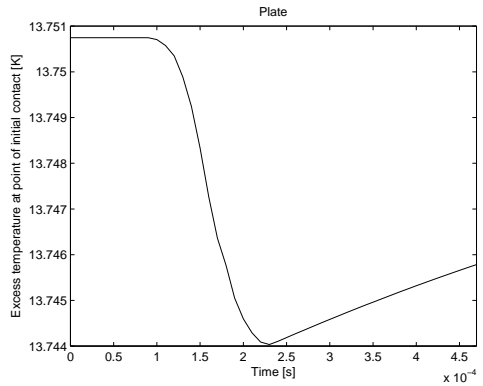
Figure 18: Computed time-evolution of the creepage.

peratures measured at the nominal contact points on the cylinder and plate surfaces. The former figure shows the time interval $0 < t < 2t_2$ and the latter the interval $0 < t < t_e$. The momentaneous, local loss of contact, which occurs as the cylinder traverses the hole in the plate (during the time interval $t_1 < t < t_2$), results in a slight, temporary decrease in the rate of frictional heat generation, as well as in the interfacial heat flux. Figure 19 shows that the latter effect is dominant, as there is an increase in temperature in the cylinder domain, owing to a temporary decrease in the convective cooling effect that arises due to thermal interaction with the colder plate. Conversely, there is a decrease in temperature in the plate domain, owing to a temporary decrease in the supply of heat from the hotter cylinder domain. The effect of the temporary decrease in the rate of frictional heat generation – which should tend to lower the temperatures in both cylinder and plate – is visible in that the magnitude of the temperature change during the traversal of the hole is larger in the plate than in the cylinder. Had this effect been absent, these temperature changes would have been roughly equal. Had it been dominant, the temperature would decrease in both domains.

After the contact patch has passed over the hole (i.e. for $t > t_2$), the temperatures oscillate somewhat while converging to their stationary values (Figure 20). The reason is the oscillations in the normal contact pressures shown in Figure 21, which in turn influence the frictional heat generation. The resulting temperature fluctuations are not instantaneous, which is the reason for the phase shift observed between Figures 20a/b and 21.



(a) Cylinder.



(b) Plate.

Figure 19: Time-evolution of the excess temperature at the point of initial contact.

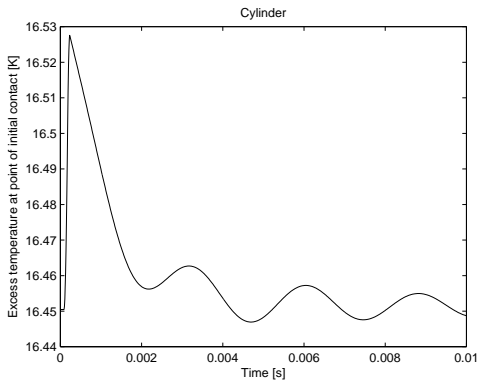
7 Concluding remarks

A theoretical and computational framework based on an ALE kinematical description and aimed toward analysis of fully transient, thermomechanically coupled, frictional rolling contact has been established. Furthermore, a matrix decomposition scheme for computationally efficient assembly of the time-dependent FE matrices, as well as a methodology for controlling external driving forces (rather than nominal rolling velocities), have been developed. Here, the aforementioned matrix decomposition scheme was again employed, this time to derive the tangent stiffness matrix for the associated nonlinear equation system.

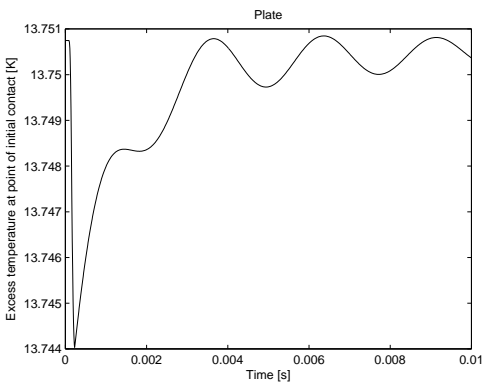
Numerical examples were presented, covering a number of distinct dynamical, thermomechanical rolling contact phenomena, operating on a broad range of time scales. These examples illustrate the modelling capabilities of the computational framework, which include capturing inertial effects and accommodating thermo-mechanical phenomena and highly discontinuous surface geometries.

Highlighted aspects in the thermomechanical analysis includes convective cooling of the rolling body due to contact with the running surface, frictional heat generation, and their dependence on local, transient variations in the slip velocity field. Furthermore, the time scales on which mechanical and thermal mechanisms operate were assessed, and found to be very different in magnitude. This meant that a choice always had to be made between a time step size small enough to resolve small time scale phenomena (such as the redistribution of slip velocities as a result of a change in the creepage: see Section 6.2.1), and one large enough to allow for simulation times suitable for analyzing large time scale phenomena (such as acceleration/braking simulations: see Section 6.2.2). Thus, the implementation of support for variable time step sizes should be considered for the continued development of the computational model. This would allow for local refinement of the time discretization in the vicinity of regions where small time scale phenomena are especially prevalent. An obvious example of a situation where such functionality would be useful is one including traversal of a sharp discontinuity in the plate (see Section 6.2.3).

Another priority for upcoming work should be to replace the regularized friction law by an approach independent of numerical modelling parameters. Viable options include a Lagrange multiplier method [21] or the approach presented in Zieffe and Nackenhorst [14], which is based on integration of slip velocities along material path lines. An approach that is devoid of parameters whose appropriate values depend on slip velocity magnitudes does not require special considerations (such as parametric convergence studies) when rolling velocities



(a) Cylinder.



(b) Plate.

Figure 20: Time-evolution of the excess temperature at the point of initial contact.

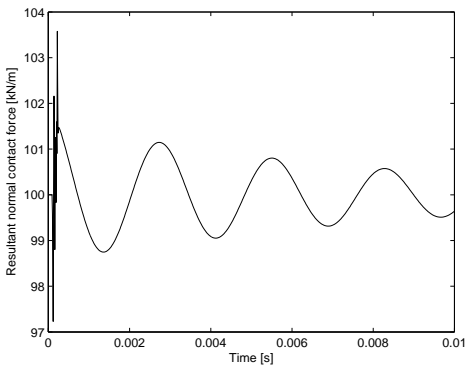


Figure 21: Time-evolution of the resultant normal force.

are varied across orders of magnitude, and is furthermore likely to be more robust.

Apart from the presented numerical simulations, another example of a possible mode of analysis using the presented computational model is an investigation of the slip behaviour of systems in rolling contact: Using the aforementioned methodology for controlling external driving forces, one may in each instant in time evaluate the distribution of slip velocities to an arbitrarily high resolution in time and space, in order to assess the proximity to sliding. Further, one might consider cases of varying tribological properties across the contact interface (for instance, the coefficient of friction could be given a spatial dependence), e.g. in order to investigate the performance of automatic slip prevention systems.

One of the main motivations for the development of the computational model has been for it to reach a state where it can be coupled to a multi-body vehicle dynamical framework – interfacing with the cylinder–plate model via the nominal rolling velocities, or the driving forces acting on the cylinder hub. Although many applications would additionally require a generalization to 3D geometries for an accurate representation of pertinent physical phenomena, this point can now be considered to have been reached. The construction of such a coupled model would result in a framework for vehicle dynamics analysis equipped with a versatile and sophisticated model for the contact interface. This would potentially enable high-resolution analysis of e.g. thermomechanical rolling contact fatigue, thermal damage phenomena, rolling noise generation and corrugation mechanisms.

A Decomposition of system matrices

The following is the subset of all FE matrices that depend on the convective velocity parameters ω , \dot{V} and

their derivatives [16]:

$$\begin{aligned}\underline{\mathbf{K}}_{uu} &= \int_{\hat{\Omega}} \underline{\mathbf{B}}_u^T \underline{\mathbf{E}} \underline{\mathbf{B}}_u dV - \hat{\rho} \int_{\hat{\Omega}} \underline{\mathbf{B}}_u^T \underline{\bar{\mathbf{v}}}_E \underline{\mathbf{B}}_u dV + \\ &\quad \hat{\rho} \int_{\hat{\Omega}} \underline{\mathbf{N}}_u^T \underline{\bar{\mathbf{v}}}_r \underline{\mathbf{B}}_u dV + \hat{\rho} \int_{\hat{\Gamma}_{R_u}} (\bar{\mathbf{v}} \cdot \hat{\mathbf{N}}) \underline{\mathbf{N}}_u^T \underline{\bar{\mathbf{v}}}_1 \underline{\mathbf{B}}_u dA, \\ \underline{\mathbf{C}}_{uu} &= 2\hat{\rho} \int_{\hat{\Omega}} \underline{\mathbf{N}}_u^T \underline{\bar{\mathbf{v}}}_1 \underline{\mathbf{B}}_u dV, \\ \underline{\mathbf{K}}_{\theta\theta} &= k \int_{\hat{\Omega}} \underline{\mathbf{B}}_{\theta}^T \underline{\mathbf{B}}_{\theta} dV - \hat{\rho} c \int_{\hat{\Omega}} \underline{\mathbf{B}}_{\theta}^T \underline{\bar{\mathbf{v}}}_1 \underline{\mathbf{N}}_{\theta} dV \\ &\quad + \hat{\rho} c \int_{\hat{\Gamma}_{R_{\theta}}} (\bar{\mathbf{v}} \cdot \hat{\mathbf{N}}) \underline{\mathbf{N}}_{\theta}^T \underline{\mathbf{N}}_{\theta} dA, \\ \underline{\mathbf{K}}_{\theta u} &= \alpha E \theta^{\text{ref}} \int_{\hat{\Gamma}_{R_{\theta}}} \underline{\mathbf{N}}_{\theta}^T (\hat{\mathbf{N}} \otimes \bar{\mathbf{v}})^T \underline{\mathbf{B}}_u dA \\ &\quad - \alpha E \theta^{\text{ref}} \int_{\hat{\Omega}} \underline{\mathbf{B}}_{\theta}^T \underline{\bar{\mathbf{v}}}_1 \underline{\mathbf{B}}_u dV, \\ \underline{\mathbf{f}}_{uv} &= \int_{\hat{\Omega}} \underline{\mathbf{N}}_u^T \underline{\hat{\mathbf{B}}} dV - \hat{\rho} \int_{\hat{\Omega}} \underline{\mathbf{N}}_u^T \underline{\bar{\mathbf{v}}}_B dV.\end{aligned}$$

Here, $(\bar{\mathbf{v}}_E)_{ijkl} = \delta_{ik}\bar{v}_j\bar{v}_l$, $(\bar{\mathbf{v}}_1)_{ijk} = \delta_{ij}\bar{v}_k$, $(\bar{\mathbf{v}}_r)_{ijk} = \delta_{ij}(D_t\bar{v}_k - (\bar{v}_k\bar{v}_l)_{,l})$, $(\bar{\mathbf{v}}_B)_i = D_t\bar{v}_i - \dot{\bar{X}}_i$ and $\bar{\mathbf{v}}$ are tensors dependent on the convective velocity parameters. $\hat{\mathbf{N}}$ is the outward normal to $\hat{\Omega}$ and $\hat{\Gamma}_R$ is the subset of the boundary $\hat{\Gamma}$ of $\hat{\Omega}$ where Robin-type boundary conditions are imposed [16]. $\underline{\mathbf{N}}_u$, $\underline{\mathbf{N}}_{\theta}$ are shape function matrices and $\underline{\mathbf{B}}_u$, $\underline{\mathbf{B}}_{\theta}$ their respective gradients. The underline notation denotes the use of a Voigt matrix representation of tensors.

As stated in Section 5.2.1, the above matrices may be rewritten as linear combinations of time-independent matrices, with coefficients that are functions of the convective velocity parameters and their time-derivatives (see eq. (20)). In order to achieve this, the convective velocity parameters are first factored out from the tensors in which they are contained, and finally from each integral expression as a whole. For instance, $\bar{\mathbf{v}}$ and $D_t\bar{\mathbf{v}}$ (see eqs. (4) and (7), respectively) are rewritten as

$$\bar{\mathbf{v}} = \begin{cases} \omega \bar{\mathbf{w}}_{\bar{\mathbf{v}}}^{c,\omega} & \text{for } \hat{\mathbf{X}} \in \hat{\Omega}^c \\ \dot{V} \bar{\mathbf{w}}_{\bar{\mathbf{v}}}^{p,\dot{V}} & \text{for } \hat{\mathbf{X}} \in \hat{\Omega}^p \end{cases}, \quad (30)$$

$$D_t\bar{\mathbf{v}} = \begin{cases} \dot{\omega} \bar{\mathbf{w}}_{D_t\bar{\mathbf{v}}}^{c,\dot{\omega}} + \omega^2 \bar{\mathbf{w}}_{D_t\bar{\mathbf{v}}}^{c,\omega^2} & \text{for } \hat{\mathbf{X}} \in \hat{\Omega}^c \\ \dot{V} \bar{\mathbf{w}}_{D_t\bar{\mathbf{v}}}^{p,\dot{V}} & \text{for } \hat{\mathbf{X}} \in \hat{\Omega}^p \end{cases}, \quad (31)$$

where $\bar{\mathbf{w}}_{\bar{\mathbf{v}}}^{c,\omega} = \bar{\mathbf{w}}_{D_t\bar{\mathbf{v}}}^{c,\dot{\omega}} = \mathbf{Q} \cdot \hat{\mathbf{X}}$, $\bar{\mathbf{w}}_{\bar{\mathbf{v}}}^{p,\dot{V}} = \bar{\mathbf{w}}_{D_t\bar{\mathbf{v}}}^{p,\dot{V}} = -\mathbf{e}_x$ and $\bar{\mathbf{w}}_{D_t\bar{\mathbf{v}}}^{c,\omega^2} = -\hat{\mathbf{X}}$. Setting out from these expressions, the following can be stated:

$$\underline{\bar{\mathbf{v}}}_E = \begin{cases} \omega^2 \underline{\bar{\mathbf{w}}}_E^{c,\omega^2} \\ \dot{V}^2 \underline{\bar{\mathbf{w}}}_E^{p,\dot{V}^2} \end{cases} \quad \underline{\bar{\mathbf{v}}}_r = \begin{cases} \omega^2 \underline{\bar{\mathbf{w}}}_r^{c,\omega^2} + \dot{\omega} \underline{\bar{\mathbf{w}}}_r^{c,\dot{\omega}} \\ \dot{V} \underline{\bar{\mathbf{w}}}_r^{p,\dot{V}} \end{cases} \quad (32)$$

$$\underline{\bar{\mathbf{v}}}_1 = \begin{cases} \omega \underline{\bar{\mathbf{w}}}_1^{c,\omega} \\ \dot{V} \underline{\bar{\mathbf{w}}}_1^{p,\dot{V}} \end{cases} \quad \bar{\mathbf{v}} \cdot \hat{\mathbf{N}} = \begin{cases} 0 \\ \dot{V} \bar{\mathbf{w}}_{\bar{\mathbf{v}} \cdot \hat{\mathbf{N}}}^{p,\dot{V}} \end{cases} \quad (33)$$

$$\hat{\mathbf{N}} \otimes \bar{\mathbf{v}} = \begin{Bmatrix} \omega \bar{\mathbf{w}}_{\hat{\mathbf{N}} \otimes \bar{\mathbf{v}}}^{c, \omega} \\ \bar{\mathbf{V}} \bar{\mathbf{w}}_{\hat{\mathbf{N}} \otimes \bar{\mathbf{v}}}^{p, \bar{\mathbf{V}}} \end{Bmatrix} \quad \bar{\mathbf{v}}_B = \begin{Bmatrix} \bar{\mathbf{V}} \bar{\mathbf{w}}_B^{c, \bar{\mathbf{V}}} + \omega^2 \bar{\mathbf{w}}_B^{c, \omega^2} + \dot{\omega} \bar{\mathbf{w}}_B^{c, \dot{\omega}} \\ \mathbf{0} \end{Bmatrix} \quad (34)$$

where the top/bottom rows in each expression correspond to the cylinder/plate domain, respectively. The explicit expressions for the $\bar{\mathbf{w}}$ -terms are omitted. At this stage, the velocity-independent matrices shown in eq. (20) may be expressed as follows:

$$\begin{aligned} \underline{\mathbf{K}}_{uu}^0 &= \int_{\hat{\Omega}} \underline{\mathbf{B}}_u^T \underline{\mathbf{E}} \underline{\mathbf{B}}_u dV, \\ \underline{\mathbf{K}}_{uu}^{\omega^2} &= -\hat{\rho} \int_{\hat{\Omega}^c} \underline{\mathbf{B}}_u^T \bar{\mathbf{w}}_E^{c, \omega^2} \underline{\mathbf{B}}_u dV \\ &\quad + \hat{\rho} \int_{\hat{\Omega}^c} \underline{\mathbf{N}}_u^T \bar{\mathbf{w}}_r^{c, \omega^2} \underline{\mathbf{B}}_u dV, \\ \underline{\mathbf{K}}_{uu}^{\dot{\omega}} &= \hat{\rho} \int_{\hat{\Omega}^c} \underline{\mathbf{N}}_u^T \bar{\mathbf{w}}_r^{c, \dot{\omega}} \underline{\mathbf{B}}_u dV, \\ \underline{\mathbf{K}}_{uu}^{\bar{\mathbf{V}}^2} &= -\hat{\rho} \int_{\hat{\Omega}^p} \underline{\mathbf{B}}_u^T \bar{\mathbf{w}}_E^{p, \bar{\mathbf{V}}^2} \underline{\mathbf{B}}_u dV \\ &\quad + \hat{\rho} \int_{\hat{\Gamma}_{\text{Rp}}} \bar{\mathbf{w}}_{\bar{\mathbf{v}} \cdot \hat{\mathbf{N}}}^{p, \bar{\mathbf{V}}} \underline{\mathbf{N}}_u^T \bar{\mathbf{w}}_l^{p, \bar{\mathbf{V}}} \underline{\mathbf{B}}_u dA, \\ \underline{\mathbf{K}}_{uu}^{\dot{\mathbf{V}}} &= \hat{\rho} \int_{\hat{\Omega}^p} \underline{\mathbf{N}}_u^T \bar{\mathbf{w}}_r^{p, \dot{\mathbf{V}}} \underline{\mathbf{B}}_u dV, \end{aligned} \quad (35)$$

$$\begin{aligned} \underline{\mathbf{C}}_{uu}^{\omega} &= 2\hat{\rho} \int_{\hat{\Omega}^c} \underline{\mathbf{N}}_u^T \bar{\mathbf{w}}_l^{c, \omega} \underline{\mathbf{B}}_u dV, \\ \underline{\mathbf{C}}_{uu}^{\bar{\mathbf{V}}} &= 2\hat{\rho} \int_{\hat{\Omega}^p} \underline{\mathbf{N}}_u^T \bar{\mathbf{w}}_l^{p, \bar{\mathbf{V}}} \underline{\mathbf{B}}_u dV, \end{aligned} \quad (36)$$

$$\begin{aligned} \underline{\mathbf{K}}_{\theta\theta}^0 &= k \int_{\hat{\Omega}} \underline{\mathbf{B}}_{\theta}^T \underline{\mathbf{B}}_{\theta} dV, \\ \underline{\mathbf{K}}_{\theta\theta}^{\omega} &= -\hat{\rho} c \int_{\hat{\Omega}^c} \underline{\mathbf{B}}_{\theta}^T \bar{\mathbf{w}}_{\bar{\mathbf{v}}}^{c, \omega} \underline{\mathbf{N}}_{\theta} dV, \\ \underline{\mathbf{K}}_{\theta\theta}^{\bar{\mathbf{V}}} &= -\hat{\rho} c \int_{\hat{\Omega}^p} \underline{\mathbf{B}}_{\theta}^T \bar{\mathbf{w}}_{\bar{\mathbf{v}}}^{p, \bar{\mathbf{V}}} \underline{\mathbf{N}}_{\theta} dV \\ &\quad + \hat{\rho} c \int_{\hat{\Gamma}_{\text{Rp}}} \bar{\mathbf{w}}_{\bar{\mathbf{v}} \cdot \hat{\mathbf{N}}}^{p, \bar{\mathbf{V}}} \underline{\mathbf{N}}_{\theta}^T \underline{\mathbf{N}}_{\theta} dA, \end{aligned} \quad (37)$$

$$\begin{aligned} \underline{\mathbf{K}}_{\theta u}^{\omega} &= \alpha E \theta^{\text{ref}} \int_{\hat{\Gamma}_{\text{R}\theta}} \underline{\mathbf{N}}_{\theta}^T \bar{\mathbf{w}}_{\hat{\mathbf{N}} \otimes \bar{\mathbf{v}}}^{c, \omega} \underline{\mathbf{B}}_u dA \\ &\quad - \alpha E \theta^{\text{ref}} \int_{\hat{\Omega}^c} \underline{\mathbf{B}}_{\theta}^T \bar{\mathbf{w}}_l^{c, \omega} \underline{\mathbf{B}}_u dV, \\ \underline{\mathbf{K}}_{\theta u}^{\bar{\mathbf{V}}} &= \alpha E \theta^{\text{ref}} \int_{\hat{\Gamma}_{\text{Rp}}} \underline{\mathbf{N}}_{\theta}^T \bar{\mathbf{w}}_{\hat{\mathbf{N}} \otimes \bar{\mathbf{v}}}^{p, \bar{\mathbf{V}}} \underline{\mathbf{B}}_u dA \\ &\quad - \alpha E \theta^{\text{ref}} \int_{\hat{\Omega}^p} \underline{\mathbf{B}}_{\theta}^T \bar{\mathbf{w}}_l^{p, \bar{\mathbf{V}}} \underline{\mathbf{B}}_u dV, \end{aligned} \quad (38)$$

$$\begin{aligned} \underline{\mathbf{f}}_{uv}^{\text{ext}} &= \int_{\hat{\Omega}} \underline{\mathbf{N}}_u^T \hat{\underline{\mathbf{E}}} dV, \\ \underline{\mathbf{f}}_{uv}^{\omega^2} &= -\hat{\rho} \int_{\hat{\Omega}^c} \underline{\mathbf{N}}_u^T \bar{\mathbf{w}}_B^{c, \omega^2} dV, \\ \underline{\mathbf{f}}_{uv}^{\dot{\omega}} &= -\hat{\rho} \int_{\hat{\Omega}^c} \underline{\mathbf{N}}_u^T \bar{\mathbf{w}}_B^{c, \dot{\omega}} dV, \\ \underline{\mathbf{f}}_{uv}^{\bar{\mathbf{V}}} &= -\hat{\rho} \int_{\hat{\Omega}^c} \underline{\mathbf{N}}_u^T \bar{\mathbf{w}}_B^{c, \bar{\mathbf{V}}} dV. \end{aligned} \quad (39)$$

B Control of driving forces

B.1 Expressions for the driving force and moment

As shown in eq. (24), the driving force F_x and the (counter-clockwise) driving moment M are expressed as

$$\begin{aligned} M(\hat{\mathbf{u}}, \bar{\boldsymbol{\theta}}, \omega, \bar{\mathbf{V}}) &= \underline{\mathbf{A}}_M(\hat{\mathbf{u}}) \underline{\mathbf{f}}_{\text{int}, u}(\hat{\mathbf{u}}, \bar{\boldsymbol{\theta}}, \omega, \bar{\mathbf{V}}) \\ F_x(\hat{\mathbf{u}}, \bar{\boldsymbol{\theta}}, \omega, \bar{\mathbf{V}}) &= \underline{\mathbf{A}}_{F_x} \underline{\mathbf{f}}_{\text{int}, u}(\hat{\mathbf{u}}, \bar{\boldsymbol{\theta}}, \omega, \bar{\mathbf{V}}) \end{aligned} \quad (40)$$

Here,

$$\begin{aligned} \underline{\mathbf{A}}_M(\hat{\mathbf{u}}) &= [|\hat{y}_{n_1}| \hat{x}_{n_1} | \dots | -\hat{y}_{n_N}| \hat{x}_{n_N}] \\ \underline{\mathbf{A}}_{F_x} &= [|\hat{1}| | \dots | | \hat{1}|]. \end{aligned} \quad (41)$$

In these expressions, the notation ‘|’ represents a sequence of zeros, zero or more in number. The nonzero elements are distributed so as to correspond to the following set of degrees of freedom on the cylinder inner boundary: $d_{n_1, x}$, $d_{n_1, y}$, \dots , $d_{n_N, x}$, $d_{n_N, y}$. For instance, $d_{n_i, x}$ is the horizontal degree of freedom corresponding to node number n_i on the cylinder inner boundary (of which the total number is N). Note that $\underline{\mathbf{A}}_M$ may be approximated as deformation-independent by evaluating it in the undeformed domain.

B.2 Tangent stiffness matrix

The tangent stiffness matrix for the case where both the external moment M and the external horizontal force F_x are controlled is expressed as follows in the stationary case:

$$\frac{\partial \underline{\mathbf{r}}}{\partial \underline{\mathbf{X}}} = \begin{bmatrix} \partial \underline{\mathbf{r}}_u / \partial \hat{\mathbf{u}} & \partial \underline{\mathbf{r}}_u / \partial \bar{\boldsymbol{\theta}} & \partial \underline{\mathbf{r}}_u / \partial \omega & \partial \underline{\mathbf{r}}_u / \partial \bar{\mathbf{V}} \\ \partial \underline{\mathbf{r}}_{\theta} / \partial \hat{\mathbf{u}} & \partial \underline{\mathbf{r}}_{\theta} / \partial \bar{\boldsymbol{\theta}} & \partial \underline{\mathbf{r}}_{\theta} / \partial \omega & \partial \underline{\mathbf{r}}_{\theta} / \partial \bar{\mathbf{V}} \\ \partial \underline{\mathbf{r}}_{\omega} / \partial \hat{\mathbf{u}} & \partial \underline{\mathbf{r}}_{\omega} / \partial \bar{\boldsymbol{\theta}} & \partial \underline{\mathbf{r}}_{\omega} / \partial \omega & \partial \underline{\mathbf{r}}_{\omega} / \partial \bar{\mathbf{V}} \\ \partial \underline{\mathbf{r}}_{\bar{\mathbf{V}}} / \partial \hat{\mathbf{u}} & \partial \underline{\mathbf{r}}_{\bar{\mathbf{V}}} / \partial \bar{\boldsymbol{\theta}} & \partial \underline{\mathbf{r}}_{\bar{\mathbf{V}}} / \partial \omega & \partial \underline{\mathbf{r}}_{\bar{\mathbf{V}}} / \partial \bar{\mathbf{V}} \end{bmatrix}, \quad (42)$$

where the residual $\underline{\mathbf{r}}$ and the array of unknowns $\underline{\mathbf{X}}$ were given in Section 5.3.1. Omitting contributions from the

stabilization matrices, the tangent stiffness matrix is expressed as

$$\frac{\partial \mathbf{r}}{\partial \underline{\mathbf{X}}} = \begin{bmatrix} \underline{\mathbf{K}}_{uu} & \underline{\mathbf{K}}_{u\theta} & 2\omega(\underline{\mathbf{K}}_{uu}^{\omega^2} \hat{\underline{\mathbf{u}}} - \underline{\mathbf{f}}_{uu}^{\omega^2}) \\ \underline{\mathbf{K}}_{\theta u} & \underline{\mathbf{K}}_{\theta\theta} & \underline{\mathbf{K}}_{\theta u}^{\omega} \hat{\underline{\mathbf{u}}} + \underline{\mathbf{K}}_{\theta\theta}^{\omega} \hat{\underline{\theta}} \\ \underline{\mathbf{A}}_M \underline{\mathbf{K}}_{uu} & \underline{\mathbf{A}}_M \underline{\mathbf{K}}_{u\theta} & 2\omega \underline{\mathbf{A}}_M (\underline{\mathbf{K}}_{uu}^{\omega^2} \hat{\underline{\mathbf{u}}} - \underline{\mathbf{f}}_{uu}^{\omega^2}) \\ \underline{\mathbf{A}}_{F_x} \underline{\mathbf{K}}_{uu} & \underline{\mathbf{A}}_{F_x} \underline{\mathbf{K}}_{u\theta} & 2\omega \underline{\mathbf{A}}_{F_x} (\underline{\mathbf{K}}_{uu}^{\omega^2} \hat{\underline{\mathbf{u}}} - \underline{\mathbf{f}}_{uu}^{\omega^2}) \end{bmatrix} - \partial \begin{bmatrix} \underline{\mathbf{f}}_{c,u}(\hat{\underline{\mathbf{u}}}, \hat{\underline{\theta}}, \omega, \bar{V}) \\ \underline{\mathbf{f}}_{c,\theta}(\hat{\underline{\mathbf{u}}}, \hat{\underline{\theta}}, \omega, \bar{V}) \\ \underline{\mathbf{A}}_M \underline{\mathbf{f}}_{c,u}(\hat{\underline{\mathbf{u}}}, \hat{\underline{\theta}}, \omega, \bar{V}) \\ \underline{\mathbf{A}}_{F_x} \underline{\mathbf{f}}_{c,u}(\hat{\underline{\mathbf{u}}}, \hat{\underline{\theta}}, \omega, \bar{V}) \end{bmatrix} / \partial \underline{\mathbf{X}}. \quad (43)$$

The expressions for the derivatives of the contact terms are not shown. However, these are fairly straightforward, since the only constituent quantity of these terms that depends on the convective velocity parameters is the stationary part of the slip velocity \hat{s} . The derivatives of the slip velocity \hat{s} with respect to ω and \bar{V} are (cf. eq. (17) and eq. (4))

$$\begin{aligned} \frac{\partial \hat{s}}{\partial \omega} &= \frac{\partial \hat{s}_{\text{stat}}}{\partial \omega} = (\hat{\mathbf{F}} \cdot \mathbf{Q} \cdot \hat{\mathbf{X}}) \cdot \hat{\mathbf{m}} \\ \frac{\partial \hat{s}}{\partial \bar{V}} &= \frac{\partial \hat{s}_{\text{stat}}}{\partial \bar{V}} = (\hat{\mathbf{F}}^m \cdot \mathbf{e}_x) \cdot \hat{\mathbf{m}}. \end{aligned} \quad (44)$$

The expression for the tangent stiffness matrix in the transient case is omitted. However, as argued in Section 5.3.2, it is not much more complicated as compared to the stationary case.

References

- [1] H. Hertz. “Über die berührung fester elastischer körper (On the contact of elastic solids)”. *J. reine und angewandte Mathematik* **92** (1882), 156–171.
- [2] F. W. Carter. “On the action of a locomotive driving wheel”. *Proceedings of the Royal Society of London. Series A* **112.760** (1926), 151–157. DOI: 10.1098/rspa.1926.0100.
- [3] K. L. Johnson. *Contact mechanics*. Cambridge University Press, 1987. ISBN: 9780521347969.
- [4] B. Xu and Y. Jiang. “Elastic–plastic finite element analysis of partial slip rolling contact”. *Journal of Tribology* **124.1** (Mar. 2001), 20–26. DOI: 10.1115/1.1395630.
- [5] J. J. Kalker. *Three-dimensional elastic bodies in rolling contact*. Solid mechanics and its applications. Kluwer Academic Publishers, 1990. ISBN: 9780792307129.
- [6] E. A. H. Vollebregt. *User guide for CONTACT, Vollebregt & Kalker’s rolling and sliding contact model*. Tech. rep. TR09-03, version 13.1. VORTech, Sept. 2012.
- [7] L. M. Galantucci and L. Tricarico. “Thermomechanical simulation of a rolling process with an FEM approach”. *Journal of Materials Processing Technology* **92–93** (1999), 494–501. ISSN: 0924-0136. DOI: 10.1016/S0924-0136(99)00242-3.
- [8] U. Nackenhorst. “The ALE-formulation of bodies in rolling contact: Theoretical foundations and finite element approach”. *Computer Methods in Applied Mechanics and Engineering* **193** (2004), 4299–4322. DOI: 10.1016/j.cma.2004.01.033.
- [9] J. Donéa and A. Huerta. *Finite element methods for flow problems*. Wiley, 2003. ISBN: 9780471496663.
- [10] I. Zeid and J. Padovan. “Finite element modeling of rolling contact”. *Computers & Structures* **14.1–2** (1981), 163–170. ISSN: 0045-7949. DOI: [http://dx.doi.org/10.1016/0045-7949\(81\)90098-5](http://dx.doi.org/10.1016/0045-7949(81)90098-5).
- [11] J. T. Oden and T. L. Lin. “On the general rolling contact problem for finite deformations of a viscoelastic cylinder”. *Computer Methods in Applied Mechanics and Engineering* **57.3** (1986), 297–367. ISSN: 0045-7825. DOI: [http://dx.doi.org/10.1016/0045-7825\(86\)90143-X](http://dx.doi.org/10.1016/0045-7825(86)90143-X).
- [12] J. Padovan. “Finite element analysis of steady and transiently moving/rolling nonlinear viscoelastic structure—I. Theory”. *Computers & Structures* **27.2** (1987), 249–257. ISSN: 0045-7949. DOI: [http://dx.doi.org/10.1016/0045-7949\(87\)90093-9](http://dx.doi.org/10.1016/0045-7949(87)90093-9).
- [13] U. Nackenhorst. “On the finite element analysis of steady state rolling contact”. *Contact Mechanics — Computational Techniques* (1993), 53–60. DOI: 10.2495/CON930071.
- [14] M. Zieffle and U. Nackenhorst. “Numerical techniques for rolling rubber wheels: treatment of inelastic material properties and frictional contact”. *Computational Mechanics* **42.3** (2008), 337–356. ISSN: 0178-7675. DOI: 10.1007/s00466-008-0243-9.
- [15] A. Suwannachit and U. Nackenhorst. “A novel approach for thermomechanical analysis of stationary rolling tires within an ALE-kinematic framework”. *Tire Science and Technology* **41.3** (2013), 174–195.
- [16] A. Draganis, F. Larsson, and A. Ekberg. “Finite element analysis of transient thermomechanical rolling contact using an efficient arbitrary Lagrangian–Eulerian description”. *Computational Mechanics* **54.2** (2014), 389–405. ISSN: 0178-7675. DOI: 10.1007/s00466-014-0992-6.

- [17] A. Draganis, F. Larsson, and A. Ekberg. “Finite element modelling of frictional thermomechanical rolling/sliding contact using an arbitrary Lagrangian–Eulerian formulation”. *Proceedings of the Institution of Mechanical Engineers, Part J: Journal of Engineering Tribology (in review)* (2014).
- [18] J. J. Kalker. “Wheel–rail rolling contact theory”. *Wear* **144** (1991), 243–261.
- [19] B. Schweizer and J. Wauer. “Atomistic explanation of the Gough-Joule-effect”. *The European Physical Journal B - Condensed Matter and Complex Systems* **23.3** (2001), 383–390. ISSN: 1434-6028. DOI: 10.1007/s100510170058.
- [20] N. S. Ottosen and M. Ristinmaa. *The mechanics of constitutive modeling*. Elsevier, 2005. ISBN: 9780080446066.
- [21] P. Wriggers. *Computational contact mechanics*. Springer, 2006. ISBN: 9783540326083.
- [22] D. J. Thompson. “Theoretical modelling of wheel–rail noise generation”. *Proceedings of the Institution of Mechanical Engineers, Part F: Journal of Rail and Rapid Transit* **205.2** (1991), 137–149. DOI: 10.1243/PIME_PROC_1991_205_227_02.
- [23] A. Draganis, F. Larsson, and A. Ekberg. “Numerical evaluation of the transient response due to non-smooth rolling contact using an arbitrary Lagrangian–Eulerian formulation”. *Proceedings of the Institution of Mechanical Engineers, Part J: Journal of Engineering Tribology* **226.1** (2012), 36–45. DOI: 10.1177/1350650111422015.
- [24] R. Codina, E. Onate, and M. Cervera. “The intrinsic time for the streamline upwind/Petrov-Galerkin formulation using quadratic elements”. *Computer Methods in Applied Mechanics and Engineering* **94.2** (1992), 239–262. ISSN: 0045-7825. DOI: 10.1016/0045-7825(92)90149-E.
- [25] F. Brezzi et al. “A relationship between stabilized finite element methods and the Galerkin method with bubble functions”. *Computer Methods in Applied Mechanics and Engineering* **96.1** (1992), 117–129. ISSN: 0045-7825. DOI: 10.1016/0045-7825(92)90102-P.
- [26] C. Baiocchi, F. Brezzi, and L. P. Franca. “Virtual bubbles and Galerkin-least-squares type methods (Ga.L.S.)” *Computer Methods in Applied Mechanics and Engineering* **105.1** (1993), 125–141. ISSN: 0045-7825. DOI: 10.1016/0045-7825(93)90119-I.
- [27] F. Brezzi, D. Marini, and A. Russo. “Applications of the pseudo residual-free bubbles to the stabilization of convection-diffusion problems”. *Computer Methods in Applied Mechanics and Engineering* **166.1–2** (1998). Advances in Stabilized Methods in Computational Mechanics, 51–63. ISSN: 0045-7825. DOI: [http://dx.doi.org/10.1016/S0045-7825\(98\)00082-6](http://dx.doi.org/10.1016/S0045-7825(98)00082-6).
- [28] R. R. Craig and A. J. Kurdila. *Fundamentals of structural dynamics*. Wiley, 2006. ISBN: 9780471430445.

